

MODELING OXIDATION AND PLASTICITY INDUCED DAMAGE IN
THERMAL BARRIER COATINGS (TBCS)

A THESIS SUBMITTED TO
THE GRADUATE SCHOOL OF NATURAL AND APPLIED SCIENCES
OF
MIDDLE EAST TECHNICAL UNIVERSITY

BY

FERIT SAIT

IN PARTIAL FULFILLMENT OF THE REQUIREMENTS
FOR
THE DEGREE OF DOCTOR OF PHILOSOPHY
IN
AEROSPACE ENGINEERING

JUNE 2020

Approval of the thesis:

**MODELING OXIDATION AND PLASTICITY INDUCED DAMAGE IN
THERMAL BARRIER COATINGS (TBCS)**

submitted by **FERIT SAIT** in partial fulfillment of the requirements for the degree
of **Doctor of Philosophy in Aerospace Engineering Department, Middle East
Technical University** by,

Prof. Dr. Halil Kalıpçılar
Dean, Graduate School of **Natural and Applied Sciences**

Prof. Dr. İsmail H. Tuncer
Head of Department, **Aerospace Engineering**

Assoc. Prof. Dr. Ercan Gürses
Supervisor, **Aerospace Engineering, METU**

Assoc. Prof. Dr. Özgür Aslan
Co-supervisor, **Mechanical Engineering, Atılım University**

Examining Committee Members:

Prof. Dr. Demirkan Çöker
Aerospace Engineering, METU

Assoc. Prof. Dr. Ercan Gürses
Aerospace Engineering, METU

Prof. Dr. Hasan U. Akay
Automotive Engineering, Atılım University

Assoc. Prof. Dr. Ahmet H. Argeşo
Manufacturing Engineering, Atılım University

Assoc. Prof. Dr. Hüsnü Dal
Mechanical Engineering, METU

Date:

I hereby declare that all information in this document has been obtained and presented in accordance with academic rules and ethical conduct. I also declare that, as required by these rules and conduct, I have fully cited and referenced all material and results that are not original to this work.

Name, Surname: Ferit Sait

Signature :

ABSTRACT

MODELING OXIDATION AND PLASTICITY INDUCED DAMAGE IN THERMAL BARRIER COATINGS (TBCS)

Sait, Ferit
Ph.D., Department of Aerospace Engineering
Supervisor: Assoc. Prof. Dr. Ercan Gürses
Co-Supervisor : Assoc. Prof. Dr. Özgür Aslan

June 2020, 150 pages

Computational analysis and simulation of multi-physics phenomena taking place in coating systems is still a challenging task. Specifically, for ceramic coatings used as protective systems for base materials against elevated temperatures, known as thermal barrier coating (TBC) systems, construction of continuum level models which can express coupled nonlinear phenomena has attracted great attention. Thermal stresses, oxidation, creep and numerous other mechanisms and phenomena make it even harder to model and simulate the behavior of TBCs and bring a need for the development of premier models. In this effort, a new numerical model that allows simulation of oxidation and thermally grown oxide (TGO) in bond-coat is presented. Phase field theory is used with finite strain formulation and implemented using user element subroutine (UEL) in ABAQUS software for the finite element method. Results are compared with experimental data available for TGO in the literature. Initiation and development of damage were also modeled considering plasticity induced failure. Results were also compared with experimental data available for damage and stress development in isothermal conditions.

Keywords: Thermal barrier coating, Anisotropic Phase field, Oxidation, EB-PVD Ceramic, FEM, Ceramic failure, Thermally grown oxide, Plasticity induced damage

ÖZ

ISIL BARIYER KAPLAMALARDA OKSİDASYON VE PLASTİSİTE ETKİLİ HASARIN MODELLEMESİ

Sait, Ferit
Doktora, Havacılık ve Uzay Mühendisliği Bölümü
Tez Yöneticisi: Doç. Dr. Ercan Gürses
Ortak Tez Yöneticisi : Doç. Dr. Özgür Aslan

Haziran 2020 , 150 sayfa

Kaplama sistemlerinde yer alan çoklu fizik olaylarının hesaplamalı analizi ve simülasyonu hala zor bir işdir. Özellikle, ısı bariyer kaplama (TBC) sistemleri olarak bilinen yüksek sıcaklıklara karşı temel malzemeler için bir koruma sistemi olarak kullanılan seramik kaplamalar için, birleştirilmiş doğrusal olmayan fenomenleri ifade edebilen sürekli seviye modellerin yapım büyük ilgi çekmiştir. Termal stresler, oksidasyon, sünme ve diğer birçok mekanizma ve olaylar, TBC'lerin davranışlarını modelleme ve simüle etmeyi daha da zorlaştırır ve önde gelen modellerin geliştirilmesi ihtiyacını ortaya koyar. Bu çalışmada, oksidasyonun ve bağ kaplamalarının içinde termal olarak büyümüş oksit (TGO) simülasyonuna olanak veren yeni bir sayısal model sunulmuştur. Faz alan teorisi büyük gerinim formülasyonu için sonlu elemanlar yöntemi ile ABAQUS yazılımında kullanıcı eleman altprogramı (UEL) kullanılarak uygulanmıştır. Sonuçlar literatürdeki TGO için mevcut deneysel veriler ile karşılaştırılmıştır. Plastisite kaynaklı kırılma göz önüne alınarak hasarın başlatılması ve gelişmesi de modellenmiştir. Sonuçlar ayrıca, izotermal koşullarda hasar ve gerilim gelişimi için mevcut deneysel veriler ile karşılaştırıldı.

Anahtar Kelimeler: Termal bariyer kaplama, İsootropik olmayan faz alanı, Oksidasyon, EB-PVD Seramik, FEM, Seramik kırılması, Termal olarak büyüyen oksit, Plastisite kaynaklı hasar

To my lovely family

ACKNOWLEDGMENTS

First and foremost I would like to thank Assoc. Prof. Özgür Aslan who has mentored me throughout this thesis and provided all the essentials required for this research. I deeply thank him for opening new doors for me in the academy and computational science. He has been the one who taught me how to use my theoretical knowledge in practice at the highest standard. I would like to thank my advisor Assoc. Prof. Ercan Gürses, who has supported me even before my Ph.D. studies, for his patience and for everything he has taught me in the field of computational mechanics. I would also like to thank my thesis committee members Prof. Demirkan Çöker and Assoc. Prof. Hüsnü Dal, for their invaluable guidance throughout my research. I am sincerely thankful to Prof. Hasan U. Akay and Assoc. Prof. Ahmet H. Argeşo for their acceptance to become a referee of my dissertation.

I would like to express my endless gratitude to my parents Farideh and Abdolreza and my dear sister Nazanin, who have never given up supporting me the whole of my life and during my studies at METU. Thanks to my parents-in-law Hossein and Manizheh and my dear sister-in-law Asal for motivation and support at hard times.

To my lab-mates Gamze Kabakçı, Gizem Nur Bulanık, Senem Aktaş, and Elif Pelit, thanks for the fun and support, specially to Vahid Rezazadeh and Caner Çamalan with whom we learned a lot and spent great moments.

This thesis is dedicated to my sweetheart wife Gazel, who is the greatest motivator for every struggle I have for a better life for us and others. I thank her for helping me work numberless weekends at the laboratory during this study.

Financial support from The Scientific and Technological research council of Turkey (TÜBİTAK), under project number 315M138, is also gratefully acknowledged.

TABLE OF CONTENTS

ABSTRACT	v
ÖZ	vii
ACKNOWLEDGMENTS	x
TABLE OF CONTENTS	xi
LIST OF TABLES	xiv
LIST OF FIGURES	xv
LIST OF ABBREVIATIONS	xix
LIST OF SYMBOLS	xx
CHAPTERS	
1 THERMAL BARRIER COATING	1
1.1 Introduction	1
1.1.1 Thermal barrier coatings	3
1.1.2 Numerical analysis and simulation of TBC systems	7
2 OXIDATION OF BOND-COAT ALLOY AT HIGH TEMPERATURES	13
2.1 Oxidation in TBC systems	13
2.1.1 Growth kinematics	13
3 TIME-DEPENDENT GINZBURG-LANDAU PHASE FIELD MODEL	21

3.1	Specialization of the free energy function	23
3.2	Finite Element Implementation	25
3.2.1	Diffusion Equation	26
3.2.2	G-L Equation	28
3.3	Results	30
4	PHASE TRANSFORMATION AND DEFORMATION COUPLED ANALYSIS	39
4.1	Kinematics	39
4.2	Balance Equations	43
4.3	Constitutive Equations	49
4.4	Specialization of the Constitutive equations	51
4.4.1	Bond-coat	51
4.4.2	Topcoat	53
4.5	Surface Undulation	55
4.6	Numerical Implementation	57
5	FAILURE MODELING IN THERMAL BARRIER COATINGS	77
5.1	Kinematics	78
5.1.1	Time integration	81
5.2	Analysis	84
6	CONCLUDING REMARKS	97
6.1	Future works	98
	REFERENCES	101
	APPENDICES	

A	TIME INTEGRATION FOR VISCOPLASTIC RESPONSE	115
A.1	Time integration for bond-coat material model	115
A.2	Summary of the time integration	120
A.3	Time integration for top-coat material model	121
A.4	Calculation of $\frac{\partial \mathbf{T}}{\partial \mathbf{F}}$	123
B	NUMERICAL IMPLEMENTATION OF CAHN-HILLIARD MODEL FOR PHASE SEPARATION	127
B.1	Constitutive equations	129
B.2	Numerical Implementation	130
C	MATERIAL AND ANALYSIS PARAMETER CALIBRATION	139
C.1	Top-coat elasticity	139
C.2	Bond-coat elasto-viscoplasticity	140
C.3	Alumina layer	141
D	FINITE ELEMENT IMPLEMENTATION	145
D.1	F-bar method	148
	CURRICULUM VITAE	149

LIST OF TABLES

TABLES

Table 2.1	Structural and material properties of the alloys and alumina [1, 2]. . .	17
Table 3.1	Material and analysis parameters at 1200°C	32
Table 4.1	Definition of variables	66
Table 4.2	Material and analysis parameters	67
Table 5.1	Material and analysis parameters	85
Table 5.2	Material and analysis parameters	85
Table 5.3	Damage parameters	87
Table B.1	Material and analysis parameters	133
Table C.1	Material parameters for $FeCrAlY$ at 400°C [3, 4]	141
Table C.2	Material parameters for alumina at room temperature	142
Table C.3	Material parameters for alumina at 400°C	143

LIST OF FIGURES

FIGURES

Figure 1.1	Thermal barrier coating in gas turbines	1
Figure 1.2	Porous structure of coating on the bondcoat [5]	2
Figure 1.3	spallation of topcoat [6]	3
Figure 1.4	External pores (right) and internal pores (left) in the ceramic structure [7]	5
Figure 1.5	Top view of coating a) as deposited b) after 12 hrs of sintering at 1500°C [8]	6
Figure 1.6	Change in the orientation of columnar structure (adapted from [9])	6
Figure 2.1	Oxidation schematic for a typical A_uB_v alloy (adapted from [10])	16
Figure 2.2	Schematic diagram for diffusion of paths of components for formation of Alumina.	18
Figure 2.3	Schematic of lateral and in-plane stretching due to oxide growth.	19
Figure 2.4	Evolution of the in-plane growth strain in alumina at 1200°C [11].	20
Figure 3.1	Double-well free energy at temperature below critical temperature [12].	23
Figure 3.2	The metal/oxide interface in bulk metal oxidation captured by SEM [13]	24

Figure 3.3	Comparison of analytical and numerical solutions for the phase field and the concentration	33
Figure 3.4	Schematic of hyperbolic initial conditions and no-flux boundary condition imposed on the model	34
Figure 3.5	Normalized concentration profile after 10 hrs for different mesh sizes.	35
Figure 3.6	Normalized concentration contour evolution in time $t_0 < t_1 < t_2$	36
Figure 3.7	Time evolution of the interfacial concentration in 50 hrs.	37
Figure 3.8	Diffuse interface thickness for different values of α	38
Figure 4.1	Phase propagation with an initially undulated surface.	44
Figure 4.2	Phase propagation in undulated surface after modification.	46
Figure 4.3	Image captured by SEM	56
Figure 4.4	Initial conditions specified for the concentration and phase field variable.	64
Figure 4.5	Mechanical boundary condition and TGO evolution in time after 10, 100 and 200 hrs.	68
Figure 4.6	Calibration of parameter π of mechanical stresses on TGO growth. Experimental data is taken from [14].	69
Figure 4.7	Validation of creep strain in $1050^\circ C$	70
Figure 4.8	TGO thickness versus time for the increasing values of mobility parameter \mathcal{M}	70
Figure 4.9	TGO thickness versus time for the increasing values of phase field parameter β	71
Figure 4.10	The normal Cauchy stress components (MPa) and equivalent plastic strain in the top-coat after 100 hrs of isothermal service.	72

Figure 4.11	The normal Cauchy stress components (MPa) and equivalent plastic strain in the bond-coat after 100 hrs of isothermal service.	73
Figure 4.12	Evolution of stress component in TGO, in transverse σ_{11} (left) and lateral σ_{22} (right) directions.	74
Figure 4.13	Evolution of lateral and transverse stresses in top-coat in downhill (left) and uphill of the interface (right).	74
Figure 4.14	Evolution of stresses along the TGO/bond-coat interface, in transverse (left) and lateral (right) directions.	75
Figure 4.15	The normal Cauchy stress component (MPa) in the lateral direction in the bond-coat and the TGO without top-coat creep (elastic top-coat) (left) and with creep (right) after 100 hrs.	75
Figure 5.1	Stress-strain curve for one element simple tension test.	84
Figure 5.2	Uniaxial tensile loading of a strip with a defected element.	86
Figure 5.3	Damage evolution and crack propagation in a mode I fracture test.	89
Figure 5.4	lateral and transverse cracks in the system and spallation of the top-coat due to coalescence of the cracks.	90
Figure 5.5	Cracks in the top-coat (yellow) and in the TGO (red) in an isothermally tested specimen after 96 hrs [15].	90
Figure 5.6	Cracks in an isothermally tested specimen after 200 hrs [15].	91
Figure 5.7	Damage contour for isothermal analysis after (a) 10 hrs, (b) 100 hrs and (c) 200 hrs.	92
Figure 5.8	The TGO vs. the projected stress in the TGO after 100 hrs (left) and 200 hrs (right).	93
Figure 5.9	The normal Cauchy stress components (MPa), equivalent plastic strain, and damage resistance (MPa) in the top-coat after 200 hrs of isothermal service.	94

Figure 5.10	The normal Cauchy stress components (MPa), equivalent plastic strain, and damage resistance (MPa) in the bond-coat after 200 hrs of isothermal service.	95
Figure 5.11	Damage contour for $S^d = 800\text{MPa}$ (left) and $S^d = 820\text{MPa}$ (right) after 200 hrs in the bond-coat.	96
Figure 5.12	Damage contour for $S^d = 155\text{MPa}$ (left) and $S^d = 205\text{MPa}$ (right) after 200 hrs in the top-coat.	96
Figure A.1	Flowchart of the user element subroutine.	125
Figure B.1	No-flux condition at boundaries and initial concentrations in upper and lower regions.	134
Figure B.2	Phase field illustration after approximately 12 hrs. The left contour corresponds to the C-H solution while the right one corresponds to Fick's law.	135
Figure B.3	Time evolution of normalized concentration on the path presented in the previous figure for diffusion with the Fick's law	136
Figure B.4	Time evolution of normalized concentration on the path presented in the previous figure (b) for diffusion with the C-H law	137
Figure C.1	Young's modulus for TBC deposited on different bondcoats [16].	139
Figure C.2	Change of column orientation in the EB-PVD deposited ceramic layer [17].	140
Figure C.3	Stress-strain curve for $FeCrAlY$ experimental (black) and numerical (red) result comparison [4].	141
Figure D.1	Isoparametric mapping.	146

LIST OF ABBREVIATIONS

ABBREVIATIONS

TBC	Thermal Barrier Coating
EB-PVD	Electron Beam Physical Vapor Deposition
TGO	Thermally Grown Oxide
PBR	Pilling-Bedworth Ratio
PS	Plasma Spray
UEL	User Element
UMAT	User Material
YSZ	Yttria Stabilized Zirconia
EB-PVD	Electron Beam Physical Vapor Deposition
APPS	Atmospheric Porous Pressure Spray
APS	Air Plasma Spray
FEM	Finite Element Method
BC	Bond Coat
TC	Top Coat
G-L	Ginzburg-Landau
PDE	Partial Differential Equation
SEM	Scanning Electron Microscope
DOF	Degree of Freedom

LIST OF SYMBOLS

SYMBOLS

\mathbf{u}	Displacement vector
c	Normalized concentration of species
ϕ	Phase field variable
P	Auxiliary field variable
ν	Pilling-Bedworth Ratio
\mathbf{q}	Heat flux per unit reference area
q	Heat flux with external source per unit reference volume
\mathbf{j}	Species flux per unit reference area
$\dot{\varepsilon}^p$	Equivalent plastic strain rate
$\dot{\varepsilon}_m^p$	Matrix equivalent plastic strain rate
μ	Chemical potential
ψ	Helmholtz free energy per unit reference volume
\mathbf{n}	Unit normal vector of the surface
η	Entropy per unit reference volume
φ	Viscoplastic potential
ε	Internal energy per unit reference volume
\mathbf{T}	Cauchy stress
\mathbf{T}_R	1 st Piola-Krichhoff stress
\mathbf{T}^e	2 nd Piola-Krichhoff stress
\mathbf{M}^e	Mandel stress
\mathbf{M}_0^e	Deviatoric Mandel stress
M_d^e	Projected Mandel stress

J	Jacobian
\mathbf{N}^p	Plastic flow direction
$\boldsymbol{\mathcal{E}}$	Energy conjugate to $\nabla\phi$ (vector)
\mathcal{P}	Energy conjugate to ϕ (Scalar)
$\bar{\sigma}$	Equivalent stress
\mathbf{F}	Deformation gradient
$\bar{\sigma}_m$	Matrix equivalent stress
\mathbf{E}^e	Elastic strain tensor
F	Amplifying function
\mathbf{v}	Velocity
X	Triaxiality
\mathbf{D}	Stretching tensor
\mathbf{W}	Spin tensor
\mathbf{L}	Velocity gradient
\mathbf{C}^e	Right Cauchy-Green tensor
\mathbf{R}^e	Rotation tensor
\mathbf{S}	Swelling tensor
\mathbf{b}	Body force
N	Avogadro's number
V	Volume
n	Number of molecules per unit cell
ρ	Density
W	Molar mass
ε_t	Transversal strain component
ε_l	Lateral strain component
α	Phase field parameter
β	Phase field parameter

χ	Phase field parameter
k	Phase field parameter
\mathcal{M}	Onsager's coefficient
δ	Interface thickness
σ	Inter-facial energy
D	Diffusion constant
β	Phase field parameter
S	Deformation resistance
S^d	Damage resistance
h_0	Hardening parameter
h_1	Softening parameter
m	Rate sensitivity
m^d	Damage rate sensitivity

CHAPTER 1

THERMAL BARRIER COATING

1.1 Introduction

Thermal barrier coating systems (TBC) are prime examples of modern surface engineering technologies to enhance the performance and durability of turbine blades. We outline below a research that addresses major aspects of mathematical modeling and the development of computational procedures for the thermo-mechanical structural design of high-temperature coating systems for advanced turbine technologies. The research is aimed at modeling and predicting the performance and durability of TBCs.

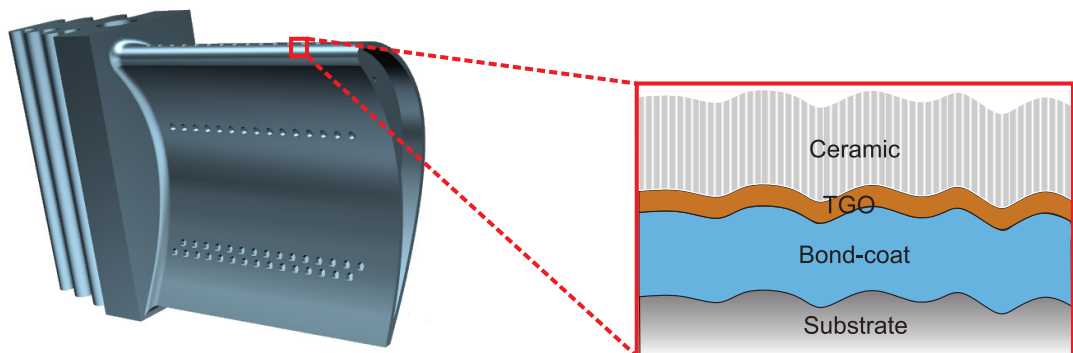


Figure 1.1: Thermal barrier coating in gas turbines

The properties and long-term stability of the individual TBC constituents are strongly dependent on their chemical composition, as well as their morphology. The latter can vary greatly with the deposition method. A typical thermal barrier coating (TBC) system shown in Figure 1.1 and Figure 1.2, consists of three layers of dissimilar materials:

1. A substrate or a base material.
2. An oxidation-resistant metallic layer or a bond-coat (BC) deposited on a superalloy.
3. A thermal insulator top-coat, which is chosen from ceramics.

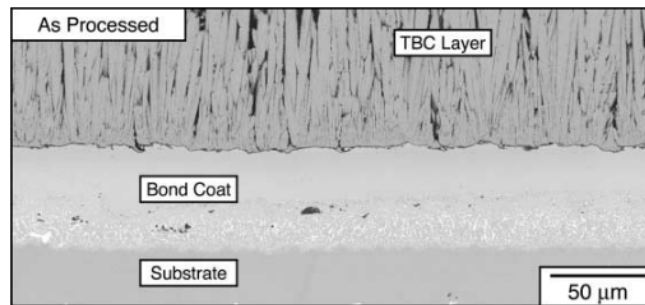


Figure 1.2: Porous structure of coating on the bondcoat [5]

Currently, the most advanced thermal barrier coating (TBC) systems consist of a platinum-modified aluminide bond-coat, and electron beam physical vapor deposition (EB-PVD) applied yttria-stabilized zirconia (YSZ) top-coat. In the case of deposition with EB-PVD the ceramic top-coat exhibits a columnar structure. The ceramic columns themselves exhibit a feathery structure and contain internal porosity. Such a microstructure of the YSZ layer offers not only strain-tolerance but also reduces thermal conductivity due to the presence of the columnar gaps and porosities (Figure 1.3).

Different mechanisms are reported to control the durability and stability of thermal barrier coatings. Oxidation induced swelling in the bond-coat, top-coat sintering, consolidation and failure processes in the multi-layer system are among the most important mechanisms in the list. Due to the material mismatch in the multi-layer TBC system, when working in high-temperature environments, extremely high stresses are induced to the system. Especially, when thermal expansion is associated with stresses induced by oxidation of the bond-coat, stresses increase to higher levels due to the constrained structure of the TBC. These high stresses are the reason for the failure of TBC systems at regions close to growing oxide specifically at material interfaces (Figure 1.3). Crack initiation and propagation are very dependent on the morphology

of the constituents of the system and loading conditions. There are several experimental efforts in the literature characterizing the nature of failure mechanisms in isothermal and cyclic thermal loading cases. One can clearly observe the initiation of the cracks in and close to a themally grown oxide layer (TGO), which generally leads to the debonding of the top-coat.

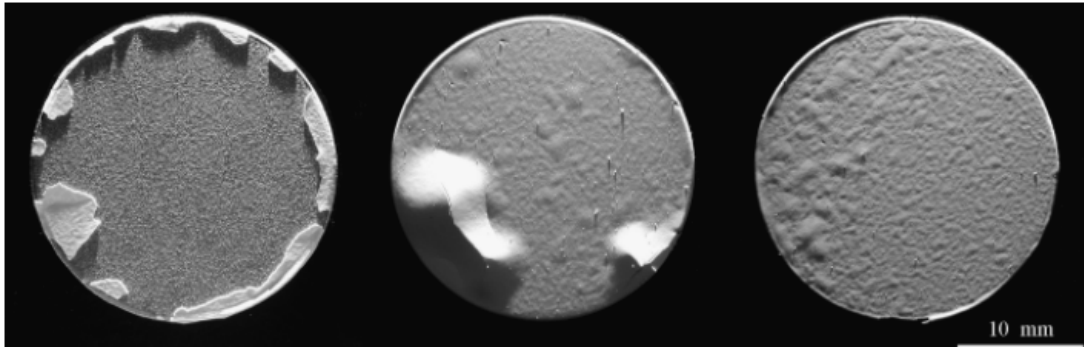


Figure 1.3: spallation of topcoat [6]

Lifetime estimation and failure of TBC systems require sophisticated continuum level models that can express a variety of physical phenomena altogether. The development and implementation of these models is a serious challenge that has attracted the attention of researchers for a while. Oxidation, thermo-elastoplastic deformation, creep, damage, phase transformation are among physical and chemical phenomena, which are working in a coupled way through the service period of TBC systems at high temperatures. It is very clear that the further development of these models will be researchers' focus point for quite a long time until they reach to a satisfactory level of precision.

1.1.1 Thermal barrier coatings

Today's thermal barrier coatings (TBCs) are mainly manufactured with two different techniques. The first coatings brought into service were plasma sprayed coatings which are still used as thermal barriers. These coatings were first tested in commercial aircraft and owe their acceptance to success in this field. However, this the success brought up the demand for research to achieve pioneer coatings that can serve in higher temperatures and more severe conditions. In cases where many thermal

cycles may happen, the use of zirconia-based coatings with a high amount of monoclinic phase was proven to be inappropriate for structures (due to high volumetric changes when transforming to the martensitic phase). Porous atmospheric-pressure plasma-sprayed (APPS) zirconia-yttria (ZrO_2 - Y_2O_3) on a plasma sprayed *NiCrAlY* bond-coat was introduced by NASA Lewis Research Center as an alternative way to overcome this handicap. This new technology is considered to be the onset of the thermal barrier coating research era [18, 19].

Using yttria as a stabilizer for the zirconia top-coat, using an oxidation-resistant material (*MCrAlY*) as a bond-coat for base metallic material and lastly using the bond-coat system to eliminate the layer mismatches between the ceramic top-coat and the base metal have been the most critical developments for the success of new coatings. Using a metallic bond-coat as a replacement for the intermediate layer reduces stresses induced by material mismatch in thermal loading. However, mitigation of stresses due to material mismatch was not significant when exposed to higher temperatures since oxidation of the metallic bond-coat would be highly accelerated causing also additional stresses [20].

A new type of coating which was deposited using the electron beam technique was developed in the late 1980s and became commercial in the 1990s. Electron beam-physical vapor deposited (EB-PVD) zirconia-yttria coating was first used and tested in the burner rig lives and performance was reported to be much better than the performance of plasma-sprayed entirely zirconia-yttria coatings [21]. Furthermore, modifications in the top-coat material made it possible to use these systems at higher temperatures [22, 23].

Coatings deposited by electron beam technique owe their long life and durability to the flexible columnar and porous structure, which makes them more strain tolerant. There are two types of porosities reported for these coatings, intracolumnar and intercolumnar vacancies (Figure 1.4). These porosities may disappear by sintering mechanism during services at high temperatures, but it is efficient enough to extend coating life by a considerable time. The micro-structure and changes in the material properties, especially the thermal diffusion and thermal conductivity of YSZ are affected as a result of sintering. Aging treatments cause the disappearance of feather-

like coating structure and generation of a structure with dispersed pores. This will lead to an increase in thermal conductivity [9].

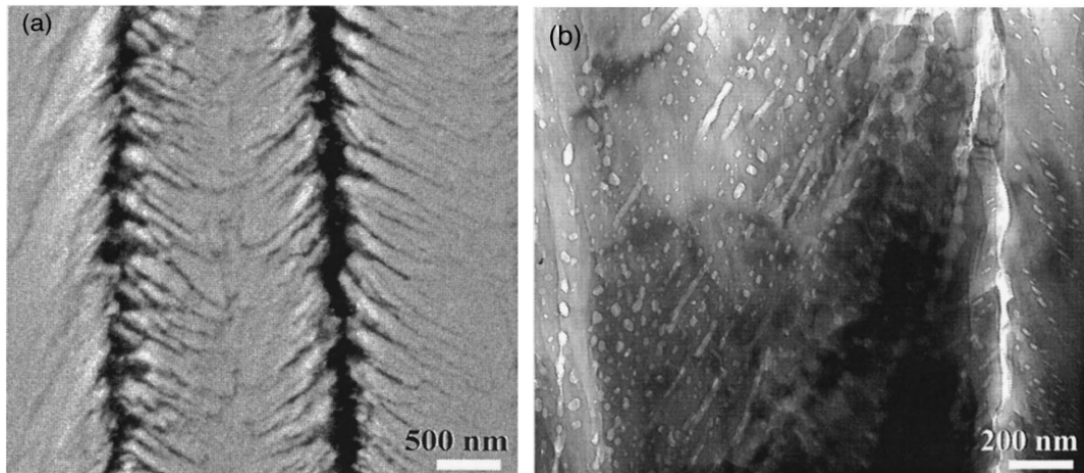


Figure 1.4: External pores (right) and internal pores (left) in the ceramic structure [7]

EB-PVD is a complex technology and requires expensive equipment, but it provides much better coating properties than other processes available for the deposition of coatings. The most basic feature of this kind of coating is the strain tolerant property provided by the columnar microstructure in the ceramic top-coat. The mechanical properties and the thermal conductivity of the TBC are dependent on the properties and microstructure of the upper layer. The bond-coat layer is a metallic layer providing adherence between the top-coat and substrate. The substrate layer is generally a single crystal superalloy used as the base material for the fabrication of the blades.

The yttrium stabilized zirconium (YSZ) coating produced by EB-PVD contains columns laid in the direction perpendicular to the substrate material. The structure of the columns can be observed in the Figure 1.2. The pores extending between the columns increase as the thickness of the plane increases. This porosity (outer porosity) extending between the columns extends the life of the TBC by increasing the flexibility of the coating. The porosity of the top-coat is known to be affected by high temperatures during the service time by a sintering process (Figure 1.5). As a result of sintering, top-coat will become thermally more conductive and structurally brittle.

The top-coat may behave as a transversely isotropic material due to the columnar structure. This structure can be observed in the Figure 1.6. The orientation of those

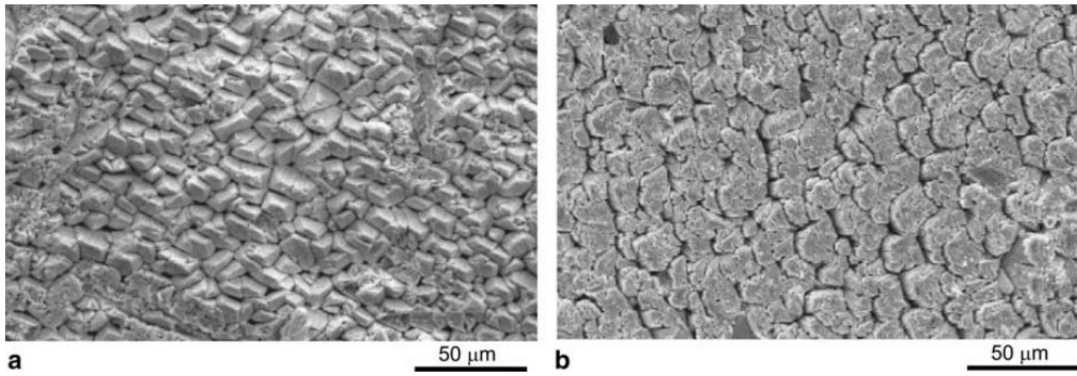


Figure 1.5: Top view of coating a) as deposited b) after 12 hrs of sintering at 1500°C [8]

columns is reported to be changing in the vicinity of the TC/BC interface.

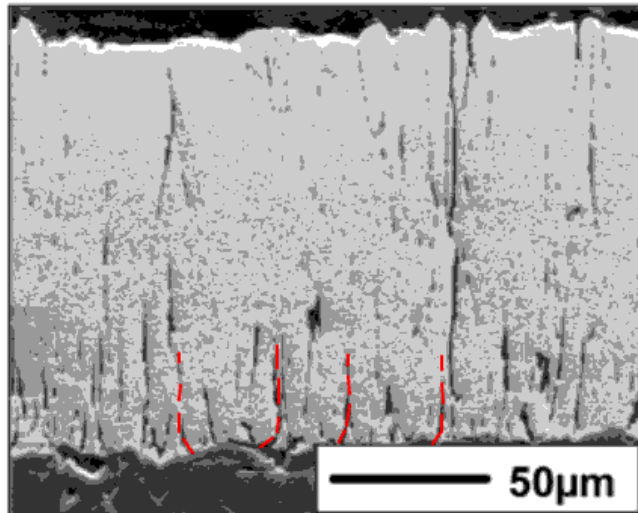


Figure 1.6: Change in the orientation of columnar structure (adapted from [9])

Oxidation of the bond coat is often considered as one of the prime mechanisms that can lead to failure of TBC systems. Evans et al. [24, 25] claimed that due to anisotropic swelling of the thermally grown oxide layer and uneven development of the TGO layer, residual stresses can rise and lead to the nucleation of micro-cracks. Therefore, they become the dominant failure mechanism which can affect the long-term durability of TBC systems. However, the mechanism through which the oxidation occurs, different species travel through materials and meet to form TGO is pretty complicated, and a significant amount of research has been conducted to clarify this

problem. For bond-coat alloys containing yttrium, diffusion of aluminum is affected by this reactive component, which decelerates diffusion of aluminum cations, thus oxide components meet in the regions closer to bond-coat material [26]. Consequently, the presence of yttrium leads to the formation of oxide mainly on the oxide-bond coat interface.

1.1.2 Numerical analysis and simulation of TBC systems

It seems that the very first computational analysis of thermal barrier coating systems was carried out by Chang et al. [27]. In this study, they have developed a finite element model using MARC to calculate isothermal stress mismatches between different layers of a TBC in a cylindrical model coated with APS (Air Plasma Spray). The sinusoidal pattern was also defined for the bond-coat/ceramic interface as an outcome of experimental researches conducted previously. For the simulation of oxidation, an artificial large thermal expansion coefficient was defined causing residual stresses in the medium. The results of this analysis emphasize the importance of oxidation in coating failures. It was also proposed that cracking may happen as a result of residual stresses at the peak of the sinusoidal interface.

In 1998 a finite element model for oxidation induced failure in a plasma-sprayed TBC was developed by Freborg et al. [28]. They focused on the creep behavior and oxidation of the bond coat. Oxidation was modeled by changing the bond-coat elements with oxide elements in time and assigning a higher thermal expansion coefficient and a small amount of dummy temperature change. Thermal cyclic loads were used and a steady-state conduction was assumed for the thermal analysis.

Cheng et al. [29] used a more realistic model in the analysis. The material property change by temperature was also considered. Thermal expansion mismatches between the TGO and the ceramic layer was also taken into account. Instead of elastic material models used in previous efforts, an elastic-perfectly plastic model was used.

Hsuiee et al. [30] investigated the relationship between the surface roughness and localized residual stresses generated due to the material thermal expansion mismatch. The material expansion mismatch is reported to have a significant role in coating

spallation and failure. The finite element method was used for the analysis of various interface profiles. It was observed that cracks predominantly were located in convex parts of asperities in thicker oxide layers.

A coupled thermo-mechanical code was developed by He et al. [31, 32, 33] to analyze the durability of TBC systems by investigating the fracture process and crack initiation due to thermal cyclic loading. The oxidation growth was also taken into account also by applying a definite growth strain at every step of the analysis.

In an experiment conducted in 2003 [34], it was discovered that the mechanical properties of the bond-coat change significantly not only with temperature change but also with cyclic loading. In this work, changes in the properties of the bond-coat due to dynamic micro-structure evolution are investigated.

Caliez et al. [35], used Zebulon (developed by Ecole des Mines de Paris and ONERA) to develop a weakly coupled FEM code. The staggered scheme used in the implementation, coupled the mechanical response and the Fick's law of diffusion. The strain growth is bonded to a parabolic strain growth with time for calculation of induced stresses .

Rosler et al. [36], used the finite element method to determine the effect of creep on the TBC life and the effect of crystal size of TGO on the relaxation to see if it is possible to tailor the micro-structure of TGO to extend the TBC life. The analysis was thermo-mechanical with isothermal and cyclic thermal loading. The TGO layer was simulated by a time-dependent property change of bond coat elements. Later they also conducted a parametric study of the effect of the creep strength and the surface undulation on the stress state in TBC systems [37].

The sintering process of EB-PVD coatings was also studied in 2005. According to this experimental effort, there may be several mechanisms for the transportation of pores in the structure of ceramic while sintering. The sintering initiates at 900°C and the diffusion and the migration of pores occur from convex to concave sites [38].

Taking the oxidation of the bond-coat into account Busso et al. [17], presented a model which includes also the solidification process of the topcoat. In this study, it is mentioned, that the aging causes external porosities of the columnar structure of the

ceramic to impinge together and form thicker columns which would mean a decrease in overall external porosity. But since there are cracks found all over the the surface this change in the structure can be neglected [8]. Then, the main mechanism which changes the material property after sintering would be, the change in internal porosity of the columnar structures. They also used a definite model to include creep in their analysis. A staggered scheme for coupling the oxide generation with the analysis was considered, in which oxygen concentration was calculated prior to thermo-mechanical analysis.

Himanshu et al. [39], conducted a parametric FEM study to investigate delamination and spallation of the top-coat due to buckling in EB-PVD coatings, where isotropic material response was assumed. The thermally grown oxide layer was modeled as a layer with constant thickness and definite material properties existing between the TC and the BC layers. They also introduced a method for the simulation of the oxidation in the bond-coat. A coupled temperature-displacement model was used and a finite difference analysis was conducted to establish a table of phase proportions in the bond-coat material as a function of time. Then, this table was linked to UMAT in ABAQUS to simulate the TGO growth in time.

In 2011, Anand [40] proposed a model for the diffusion of hydrogen in metals. A thermodynamically consistent model for large deformation elastoplasticity accounting for the species transport was developed. Later in 2011, Loeffel and Anand [41] carried out a chemo-thermo-mechanical analysis accounting for the oxygen diffusion in the model and the chemical reaction, which is a version of the previous model taking chemical reaction into account . They also implemented this model for the analysis of thermal barrier coatings later in 2013 and also included the cohesive-zone methodology to model the decohesion of ceramic top-coat [42].

In contrast to the classical models, where the interphase region of a multi-phase system was investigated using discrete solutions with possessing severe computational challenges, Cahn-Hilliard [12] and Ginzburg-Landau models (Allen-Cahn model) treat those systems as continuous domains which bring certain ease to the implementation of the model. In these approaches, the free energy is defined to be a function of either the species concentration or the order parameter (phase field variable) and

gradients of the corresponding parameters along with any other thermodynamic variable that may also be included in the model. According to these theories, a previously predetermined interfacial energy for a restricted thickness is taken into account. It is also noted that the existence of free energy due to the non-equilibrium of phases in the diffuse interface of two-phase systems was not considered at the time. The treatments proposed by Cahn-Hilliard, Allen-Cahn, and Ginzburg-Landau are general equations that can be used in the fields with a spatial variation of a parameter (composition, density, etc.). The modeling and the simulation of the oxide formation process in TBC systems have been a hot topic in the past decade and an extensive variety of models are available in the literature, but only a few of them tackle with coupled multi-physics oxidation and failure problem in the same numerical framework. Ammar et al. [43] have used the Allen-Cahn phase field model to simulate oxidation and oxide propagation in the bulk metal. This model has the nature of flattening initial phase interface undulations. In the case of the oxidation of bulk metal, the initial surface undulation smoothing is observed in time. In contrast, when the coating is present on the metal, interface undulations maintain their shape during the oxide growth due to the material mismatches [31]. The most recent and inclusive model available is proposed and implemented by Loeffle et al. [41, 42], where a modified version of the classical Fick's law for the diffusion of oxygen through ceramic is used. Thus, the model generates a sharp interface of diffusing oxide in the bond coat. The numerous simplifications and formulation difficulties raised due to modification in the Fick's law is the motive for formulating a new model in this study.

As already pointed out major contributions have been made in the past decade in chemo-thermo-mechanical modeling of oxidation of metals and phase precipitation induced swelling in two essential ways:

1. Numerical tools have been used to simulate the new phase growth and temporal evolution of the mechanical properties of the oxidized domain in the bulk material (eg. [25], [44], [45]).
2. Standard (eg. [46], [47], [48]) or non-standard phase field ([49], [50]) approaches have been coupled with mechanics to simulate isotropic and anisotropic swelling/shrinking in the material undergoing phase change process.

However to the best knowledge of authors a model and the corresponding simulation utilizing standard phase field theories coupled with mechanics in large deformation framework for formulating anisotropic swelling/shrinking is lacking. In this thesis, a comprehensive model based on the Allen-Cahn's theory, which can retain undulations during the growth of oxide by modifying a gradient term in the diffusion and phase field equation is proposed. The model is implemented in the finite strain framework using ABAQUS user element subroutine (UEL) for the finite element analysis.

CHAPTER 2

OXIDATION OF BOND-COAT ALLOY AT HIGH TEMPERATURES

2.1 Oxidation in TBC systems

The top-coat is almost transparent to the oxygen diffusion and provides nearly no oxygen insulation. The bond-coat constitutes a reservoir of aluminum reacting with the oxygen allowing the formation of a protective alumina layer at the bond-coat/ceramic interface. This layer is called the thermally grown oxide (TGO). In the following chapter the kinematics of the growing alumina is presented. The growth strain is calculated in a typical manner using the modified Pilling-Bedworth ratio, which is used for volume change calculations in chemical reactions.

2.1.1 Growth kinematics

Probably the very first research in this field was carried out by Pilling and Bedworth in 1927 [51, 52]. They have related stresses generated by the thermally grown oxide to the molar volume of traveling species. In the literature, the Pilling-Bedworth ratio (PBR) [10] for growth stresses is known to be accurate for many years but it is too simplistic since it is incapable of explaining mechanism of the oxidation and stress generation. However, this theory can be used for calculation of total volume change of a unit volume of a metal and can be related to the swelling eigenstrains. The PBR theory states that in the oxidation process of metals, when oxygen diffuses through the oxide already present on the metal face, a new oxide forms in the oxide-metal interface. Then, the PBR ratio can be calculated as

$$PBR = \frac{\text{Oxide Volume}}{\text{Metal Volume}} \quad (2.1)$$

Thus, when $PBR > 1$ or $PBR < 1$ the stress generated in the oxide constrained by the old oxide and the metal is compressive or tensile, respectively. According to Chunhua and Gao [10], this theory should be extended for alloys, since in most of the cases alloys are used instead of pure metals. They proposed an improved version of the formula by calculating the PBR based on the difference of molar volume of the metal in the pure metal and the alloy. This method, however, does not provide any information about the scale of the stress generated.

In the oxidation of metals, the formation of one mole of B_xO_y consumes x mole of B . But the volume of consumed B is different when B comes from the alloy. According to the modified PBR calculation proposed by Chunhua et al. [10] the PBR can be calculated using the following formula.

$$PBR = \frac{\text{Volume of a mole of } B_xO_y}{\text{Volume of } x \text{ moles of } B \text{ in alloy}} \quad (2.2)$$

The volume (V) of one mole of oxide is calculated via its molar mass (W) and density (ρ),

$$V = W/\rho \quad (2.3)$$

On the other hand, molar volume of the metal is calculated as

$$V = N \cdot a^3/n \quad (2.4)$$

where N is the Avogadro's number (6.02×10^{23}), a^3 is the volume of a unit cell and n is the number of molecules or atoms per unit cell.

Consider the chemical reaction given in (2.5) for the generation of one mole of B_xO_y .



The reaction (2.5) consumes x mole of B which is going to be afforded by the representative alloy A_uB_v (x , y , u and v are mole fractions). Then, one can compute the amount of the alloy A_uB_v needed to provide x mole of B ($x_{[B]}$) for oxidation as follows. The components of x mole of A_uB_v is

$$x_{[A_uB_v]} = x(u_{[A]} + v_{[B]}) \quad (2.6)$$

Then, the equation can be rearranged in the following form

$$x_{[B]} = (x/v)_{[A_uB_v]} - (ux/v)_{[A]} \quad (2.7)$$

Equation (2.7) shows that in order to provide x mole of B for oxidation, (x/v) moles of A_uB_v have to lose (ux/v) moles of A metal. The molar equation (2.7) can be written volume-wise using equation (2.4),

$$\text{Volume of } x_{[B]} = \text{Volume of } ((x/v)_{[A_uB_v]}) - \text{Volume of } (ux/v)_{[A]} \quad (2.8)$$

Equation (2.8) is valid for the case when diffusion of B is slow in the alloy, which results an A -rich region in the alloy as presented in Figure 2.1. However, in the case of oxidation at high temperatures, as pointed out in the previous chapter, the migration of ions will be faster. Thus, the region will not be rich in A and will contain A_uB_v [10]. As a result in equation (2.7), A can be replaced by A_uB_v . For this purpose one should find the number of moles of A_uB_v (D) that should be replaced by a mole of A in equation (2.7).

$$u_{[A]} = D_{[A_uB_v]} \quad (2.9)$$

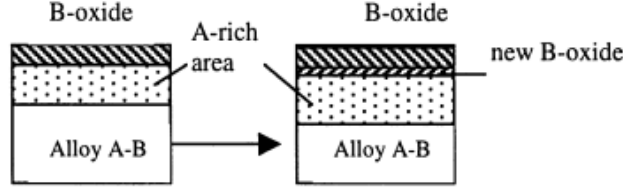


Figure 2.1: Oxidation schematic for a typical $A_u B_v$ alloy (adapted from [10])

Then, equation (2.9) can be written as

$$u_{[A]} = D(u_{[A]} + v_{[B]}) \quad (2.10)$$

Then, D is computed as

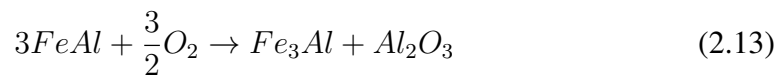
$$D = u/(u + v) \quad (2.11)$$

Rewriting equation (2.8) would result the following.

$$\text{Volume of } x_{[B]} = \text{Volume of } (x/(u + v))_{[A_u B_v]} \quad (2.12)$$

Equation (2.12) gives the volume of a metal in the alloy in extreme conditions where the diffusion of the B ions is very fast.

Specifically speaking, for TBC systems with $FeAl$ bond-coat, the oxidation reaction of the $FeAl$ alloy (2.13) occurring at the bond-coat/ceramic interface can be analyzed for the volume change of a mole of the alloy. For this purpose, first the volume of the Al in the $FeAl$ and in the Fe_3Al will be calculated. Then since the volume of a mole of Al_2O_3 can also be calculated through equation (2.3), the total volume change can be computed according to the chemical balance below.



The density of a crystal solid can be calculated using its atomic mass and lattice parameters. According to Rossi et al. [53] the molar weight and the density of Al_2O_3

Table 2.1: Structural and material properties of the alloys and alumina [1, 2].

Alloy	n	$a(\text{nm})$	$W(\text{g/mol})$	$\rho(\text{g/cm}^3)$
$FeAl$	1	0.291	-	-
Fe_3Al	16	0.579	-	-
Al_2O_3	-	-	102	3.987

are measured to be 102 g/mol and 3.987 g/cm³ respectively. Thus, using equation (2.3) the molar volume of Al_2O_3 can be calculated as below:

$$V_{Al_2O_3} = 102/3.987 = 25.58 \text{ cm}^3 \quad (2.14)$$

Using (2.4) and (2.12) volume of one mole of Al in the alloys is calculated using intermetallic alloy properties given in Table 2.1 as below.

$$\begin{aligned} \text{Volume of 1 mole of Al in } FeAl &= \left(\frac{1}{2}\right) \left(\frac{0.602 \times 10^{24} \times (0.291 \times 10^{-7})^3}{1}\right) \\ &= 7.415 \text{ cm}^3 \end{aligned} \quad (2.15)$$

$$\begin{aligned} \text{Volume of 1 mole of Al in } Fe_3Al &= \left(\frac{1}{4}\right) \left(\frac{0.602 \times 10^{24} \times (0.579 \times 10^{-7})^3}{16}\right) \\ &= 1.825 \text{ cm}^3 \end{aligned} \quad (2.16)$$

According to the reaction equilibrium (2.13) the change of the volume in the overall chemical process may be calculated as [45],

$$\frac{V_{Al_2O_3} + V_{Fe_3Al}}{V_{FeAl}} = \frac{25.58 + 1.825}{3 \times 7.415} = 1.23 \quad (2.17)$$

The calculated ratio can only show whether the generated growth stresses are tensile or compressive. However, construction of the kinematic equations of the problem involves calculation of the eigenstrains induced by the oxidation process. The determination of the growth mechanism has been one of the most challenging researches

in TBCs. In 1970 Rhines et al. [54], experimented oxidation of nickel at high temperatures in order to understand microstructural changes in the specimens and stresses induced by oxidation growth. It was observed that the rod specimens used show an increase in length and a decrease in the diameter, moreover the length increase in the specimens with smaller thicknesses was larger. The author’s interpretation of this phenomenon is the generation of an in-plane compression in the oxide in the sense that the extent of lengthening is associated with the thickness. It is proposed that the generation of the new TGO grains in the internal boundaries of the grains can be the source of in-plane (in the direction parallel to the interface plane) stresses since scale thickening (thickening in the direction normal to the interface) in no way can generate an in-plane pressure in planar bodies (Figure 2.2). It should be mentioned that the study was conducted for pure *Ni* oxidation.

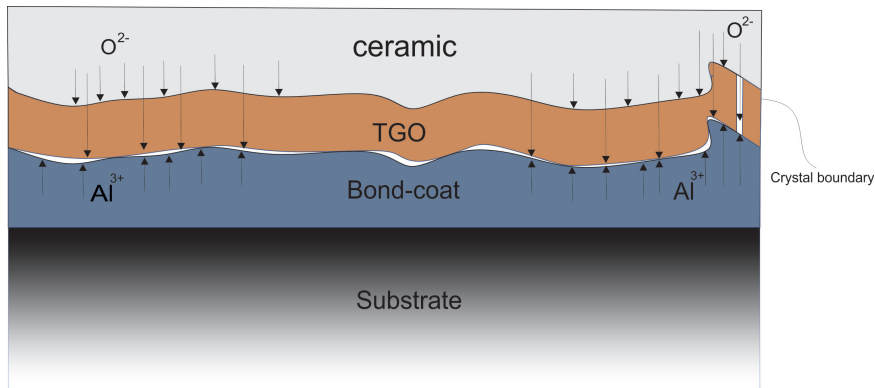


Figure 2.2: Schematic diagram for diffusion of paths of components for formation of Alumina.

For the *MCrAlY* alloy with generic *M* component, the diffusion of aluminum is effected by the reactive component yttrium, which decelerates the diffusion of aluminum cations, thus oxide components meet at regions closer to the BC [26]. As a result, the presence of yttrium in the composition of the alloy leads to formation of the oxide mainly on the oxide/bond-coat interface. The yttrium doped *FeCrAl* alloy shows quite small amount of in-plane strain while getting oxidated at high temperatures [55]. This property makes the alloy a proper candidate for usage as a bond-coat material in TBC systems. Thus *FeCrAlY* is chosen for the bond-coat through this study.

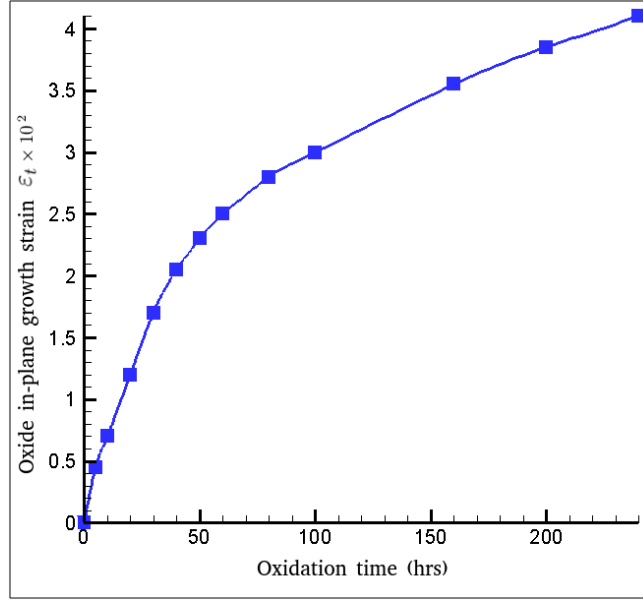


Figure 2.4: Evolution of the in-plane growth strain in alumina at 1200°C [11].

strain tensor, respectively. By neglecting higher order terms the change of the volume in a unit volume can be approximated as:

$$V = V_0 + \Delta V = 1 + \epsilon_t + \epsilon_l + \epsilon_t \quad (2.19)$$

Using the PBR value obtained in equation (2.17) one can write

$$\frac{V}{V_0} = PBR = (1 + \epsilon_l + 2\epsilon_t) = 1.23 \quad (2.20)$$

Thus, the sum of normal strain components is

$$\epsilon_l + 2\epsilon_t = 0.23 \quad (2.21)$$

Then assuming maximum transverse growth strain $\epsilon_t = 0.04$ [4], the lateral growth strain is computed as

$$\epsilon_l = 0.15 \quad (2.22)$$

CHAPTER 3

TIME-DEPENDENT GINZBURG-LANDAU PHASE FIELD MODEL

The Ginzburg-Landau (G-L) theory was originally used in the calculation of the second-order phase transitions in electromagnetic fields [56]. Later this model was used in a variety of phenomena and a variety of materials such as metals, polymers, and ceramics. Precipitation of new phases, phase growth, grain growth, dendrite formation, solidification, competitive particle ripening, spinodal decomposition, etc. are among physical and metallurgical phenomena that have been simulated using G-L model [12, 57, 58, 59, 60, 61, 62, 63, 64, 65, 66, 67, 68].

In the Ginzburg-Landau theory, it is assumed that the local energy depends on the regional composition and the inter-facial composition of the environment as well as the phase field. The Cahn-Hilliard theory [12] (the fundamental theory behind G-L) assumed that the gradient of the concentration of the species c (if the non-uniform field is chosen to be the molar fraction of a definite phase) is small enough with respect to the reciprocal of the inter-molecular distance, then ∇c can be accounted to be an independent variable. A similar assumption can be made for the gradient of the field variable (phase field), which leads to the definition of a form of free energy dependent on the phase field, the phase field gradient and the concentration of species $\psi(c, \phi, \nabla\phi, \nabla^2\phi, \dots)$. The Taylor series expansion of the function around a single phase point, ignoring higher-order terms, using divergence theorem and neglecting species inlet from boundary surface, one can write a specific form Helmholtz free energy density as below [69],

$$\psi(c, \phi, \nabla\phi) = \psi_0(c, \phi) + \frac{1}{2}\alpha\nabla\phi \cdot \nabla\phi \quad (3.1)$$

where $\psi_0(c, \phi)$ is the local free energy density and the second part of the equation is the non-local contribution of the phase field to the total energy. $\alpha > 0$ is a coefficient with energy per unit volume times length square unit.

According to the time-dependent Ginzburg-Landau equation the evolution of the non-equilibrium field variable ϕ can be expressed as follows [70],

$$\beta\dot{\phi} = \alpha\Delta\phi - \frac{\partial\psi_0}{\partial\phi} \quad (3.2)$$

where Δ is the Laplace operator. The classical derivation of the chemical potential in the form of a variational derivative is,

$$\mu = \frac{\partial\psi}{\partial c} \quad (3.3)$$

Then the flux of species can be written as,

$$\mathbf{j} = -\mathcal{M}(\phi)\nabla\mu \quad (3.4)$$

with $\mathcal{M}(\phi)$ known as the Onsager coefficient, which is a parameter generally defined dependent on the phase field. The species balance is then defined to be [71],

$$\dot{c} = \text{Div}\left(\mathcal{M}(\phi)\nabla\left(\frac{\partial\psi(c, \phi, \nabla\phi)}{\partial c}\right)\right) \quad (3.5)$$

ψ for solution composition of symbolic A and B phases is a non-convex double-well function as depicted in Figure 3.1. Then using equations (3.2) and (3.5) the interphase interface diffusion can be described.

$$\begin{cases} \dot{c} = \text{Div}\left(\mathcal{M}(\phi)\nabla\left(\frac{\partial\psi(c, \phi, \nabla\phi)}{\partial c}\right)\right) \\ \beta\dot{\phi} = \alpha\Delta\phi - \frac{\partial\psi_0(c, \phi)}{\partial\phi} \end{cases} \quad (3.6)$$

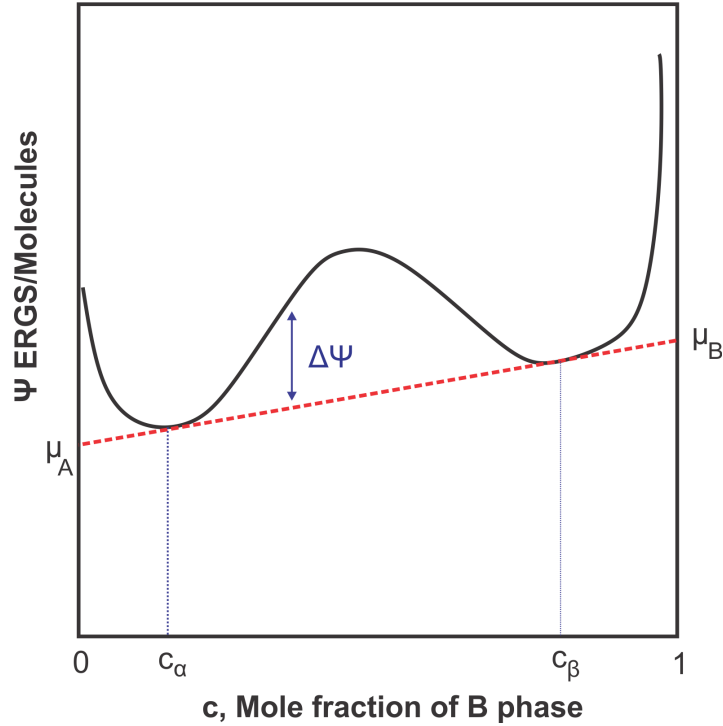


Figure 3.1: Double-well free energy at temperature below critical temperature [12].

As can be observed from equation (3.6) in order to describe the behavior, a system of second-order equations has to be solved. The substitution of the G-L equation in the diffusion equation will result in a fourth-order PDE. Therefore, for finite element solution of the problem C^1 -continuous basis functions should be used [72] but to get rid of this kind of basis functions phase field can also be defined as a new degree of freedom together with concentration to solve the system of two second-order equations instead of a fourth-order one [43].

3.1 Specialization of the free energy function

It is known, that any kind of phase diffusion without taking the free energy of the interphase region into account is mathematically ill-posed and physically wrong [73, 74]. Taking the interfacial free energy into account, phase segregation phenomena can be modeled as described and implemented in Appendix B. Separation into binodal points (labeled as c_α and c_β in Figure 3.1) will be a consequence of using non-convex double-well free energy.

The diffusion of oxygen in a solid material is considered as diffusion of a gas in a porous media. Therefore, phase separation models of diffusion which additionally include the free energy of the interphase region in the calculation seem to be improper for simulation of oxygen diffusion dependent oxide phase precipitation in the sense that oxygen in the porous media may not have a sharp boundary. Furthermore, the phase segregation is not needed if merely diffusion of oxygen is to be modeled. However, use of phase-field models proper for the interface propagation of aluminum oxide in the bond-coat can be quite reasonable [75].

A special type of alumina that is stable at 1200⁰C is $\alpha - Al_2O_3$, which is the dominant alumina phase in the oxide in our isothermal analyses. Around 1000⁰C two different phases $\theta - Al_2O_3$ and $\alpha - Al_2O_3$ are the stable phases. A phase spinal decomposition may be used in this case, but it will be quite far from the scope of this research [76, 77]. Thus, we have focused on a single alumina phase precipitation in the metal as the first step. Earlier models used for the oxidation process do lack the oxide/metal interface [78] or assume a smooth transition from the metal to the oxide phase [45]. However, a sharp change of phase is observed in SEM micrographs (Figure 3.2) [79, 80].

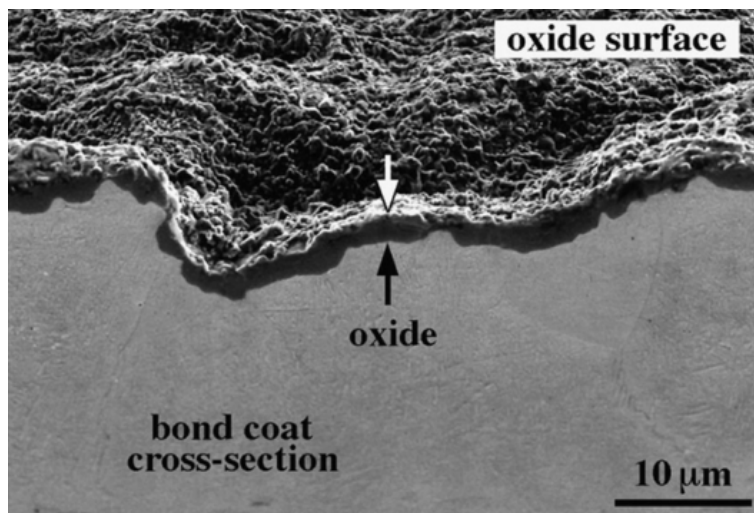


Figure 3.2: The metal/oxide interface in bulk metal oxidation captured by SEM [13]

These experimental results are the main motives for the utilization of a definite and special diffusion model to catch a sharp phase interface between alumina and substrate material. In this case, the oxide (TGO) and the metal (bond-coat) will be con-

sidered as two phases that are in equilibrium. The Cahn-Hilliard model implemented and presented in Appendix B can clearly show that a modified version of this model is needed for the simulation of moving interface. Thus, a time-dependent G-L (the equivalent model used in material science is called as the Allen-Cahn model) is found to be suitable. For this purpose, the total free energy of diffusion can be written to be as [71],

$$\psi_0(c, \phi) = \phi^2(3 - 2\phi)\psi_1(c) + (1 - \phi^2)(3 - 2\phi)\psi_2(c) + \chi\phi^2(1 - \phi)^2 \quad (3.7)$$

where χ is a parameter related to the interface energy and $\psi_i(c)$ is defined as below [81],

$$\psi_i(c) = \frac{1}{2}k_i(c - c_i)^2, \quad i = 1, 2 \quad (3.8)$$

In the equation above k_i are the curvatures of the free energy with respect to concentration and are chosen to be positive to ensure convexity at equilibrium concentrations c_i [81].

3.2 Finite Element Implementation

For the implementation purpose, now an additional degree of freedom should be considered as explained before. Two scalar fields, the concentration c and the phase field variable (order parameter) ϕ , are approximated. The approximations of the fields and the gradients can be written as below

$$c = \sum_{i=1}^n N_i c_i, \quad \nabla c = \sum_{i=1}^n \mathbf{B}_i c_i \quad (3.9)$$

$$\phi = \sum_{i=1}^n N_i \phi_i, \quad \nabla \phi = \sum_{i=1}^n \mathbf{B}_i \phi_i, \quad (3.10)$$

where n is the number of nodes and $\mathbf{B}_i = \nabla N_i$ is a matrix consisting of the derivatives of the shape function of node i . Details can be found in Appendix D).

3.2.1 Diffusion Equation

For simplicity, the diffusion constant D of the metal and the oxide phases are assumed to be equal. Since the propagation of the oxide phase in the metal is controlled by calibrated phase field parameters after setting diffusion constant to a definite value, the exact value of the mobility in different phases is not required. \mathcal{M} is known as the Onsager coefficient and for a two phase system defined as [82, 83]

$$\mathcal{M} = \phi^2(3 - 2\phi)\frac{D_1}{k_1} + (1 - \phi^2(3 - 2\phi))\frac{D_2}{k_2} \quad (3.11)$$

where D_1 and D_2 are diffusion constants for two different phases. In this study for simplicity diffusion constants and curvatures of free energy for both phases are taken to be equal so that the Onsager coefficient will be simplified to mobility coefficient. Substituting (3.7) in (3.5), after some algebraic manipulations the balance equation can be written as,

$$\dot{c} - \text{Div} \left[\mathcal{M} \nabla (\phi^2(3 - 2\phi)k_1(c - c_1) + (1 - \phi^2(3 - 2\phi))k_2(c - c_2)) \right] = 0 \quad (3.12)$$

In order to derive the weak form of this equation, (3.12) is multiplied by a weighting function w and integrating over the reference volume domain.

$$\int_{\Omega} w \left[\dot{c} - \text{Div} \left[\mathcal{M} \left[\nabla c (k_1 \phi^2(3 - 2\phi) + k_2(1 - \phi^2(3 - 2\phi))) + 6\phi \nabla \phi (1 - \phi) (k_1(c - c_1) - k_2(c - c_2)) \right] \right] \right] dV = 0 \quad (3.13)$$

where Ω denotes deformed body in the material configuration and approximated using finite elements $\Omega = \sum \Omega^e$. The boundary is decomposed into two parts such that $\partial\Omega = \partial\Omega_c \cup \partial\Omega_j$, where Ω_c and Ω_j denote the boundaries where the essential and the

natural boundary conditions are prescribed, respectively.

$$\begin{cases} c = c_0 \text{ on } \partial\Omega_c \\ -D \frac{\partial c}{\partial \mathbf{X}} = \mathbf{j}_0 \text{ on } \partial\Omega_j \end{cases} \quad (3.14)$$

Next we define,

$$a = k_1 \phi^2 (3 - 2\phi) + k_2 (1 - \phi^2 (3 - 2\phi)) \quad (3.15)$$

$$b = k_1 (c - c_1) - k_2 (c - c_2) \quad (3.16)$$

The shape function for a definite node of an element is denoted by N_A . Then the weight function is approximated as $w = N_A w_A$. With the help of the integration by parts and the divergence rule, the weak form is calculated as

$$\begin{aligned} \int_{\Omega^e} [N_A w_A \dot{c} + \mathcal{M} a w_A \nabla N_A \nabla c + (6\mathcal{M} b \phi (1 - \phi)) w_A N_A \nabla \phi] dV \\ - \int_{\partial\Omega_j} w_A N_A \mathbf{j} \cdot \mathbf{n} dS = 0 \end{aligned} \quad (3.17)$$

Then the residual vector reads

$$R_c^A = \int_{\Omega^e} [N_A \dot{c} + \mathcal{M} a \nabla N_A \nabla c + (6\mathcal{M} b \phi (1 - \phi)) N_A \nabla \phi] dV - \int_{\partial\Omega_j} N_A \mathbf{j} \cdot \mathbf{n} dS \quad (3.18)$$

with $\frac{\partial c}{\partial X_i} = \frac{\partial N_B}{\partial X_i} c_B$ and $\frac{\partial \phi}{\partial X_i} = \frac{\partial N_B}{\partial X_i} \phi_B$, where X is an arbitrary material point of Ω . The evolution of the concentration is calculated in the following manner using backward-Euler method.

$$\dot{c} = \frac{c_{t+1} - c_t}{\Delta t} \quad (3.19)$$

where c_{t+1} and c_t are the values of c at time $t + 1$ and t respectively. Stiffness matrix is also calculated to be,

$$K_{cc}^{AB} = -\frac{\partial R_c^A}{\partial c^B} = -\int_{\Omega^e} \left[\frac{N_A N_B}{\Delta t} + \mathcal{M}a \nabla N_A \nabla N_B + 6\mathcal{M}\phi(1-\phi) \frac{\partial b}{\partial c} N_B \nabla N_A \nabla \phi \right] dV - \int_{\partial\Omega_j} N_A N_B \frac{\partial \mathbf{j}}{\partial c} \cdot \mathbf{n} dS, \quad (3.20)$$

where

$$\frac{\partial b}{\partial c} = k_1 - k_2. \quad (3.21)$$

The non-zero off-diagonal term of the stiffness matrix is as following,

$$K_{c\phi}^{AB} = -\frac{\partial R_c^A}{\partial \phi^B} = -\int_{\Omega^e} \left[N_B \left(M \frac{\partial a}{\partial \phi} \right) \nabla N_A \nabla c + 6 \left(\mathcal{M} \frac{\partial b}{\partial \phi} \right) \phi (1-\phi) N_B \nabla N_A \nabla \phi + 6Mb(1-2\phi) N_B \nabla N_A \nabla \phi + 6\mathcal{M}b\phi(1-\phi) \nabla N_A \nabla N_B \right] dV \quad (3.22)$$

It should be noted that all the calculations are carried out in the reference configuration and a special care must be taken in definition of the species flux boundary condition, because the change in the configuration must be taken into account [84]. However, since the subroutine does not support surface fluxes, the calculated residuals and tangent tensors are presented in a general form.

3.2.2 G-L Equation

The boundary for phase field domain is also decomposed into two parts such that $\partial\Omega = \partial\Omega_\phi \cup \partial\Omega_\varepsilon$, where Ω_ϕ and Ω_ε denote the boundaries where the essential and the natural boundary conditions are prescribed, respectively.

$$\begin{cases} \phi = \phi_0 \text{ on } \partial\Omega_\phi \\ \alpha \frac{\partial \phi}{\partial \mathbf{X}} = \mathcal{E} \text{ on } \partial\Omega_\varepsilon \end{cases} \quad (3.23)$$

Considering the balance equation (3.2) and using the divergence theorem, the Ginzburg-Landau equation related part of the weak form is found to be as below

$$\mathcal{C} = k_1(c - c_1)^2 - k_2(c - c_2)^2 \quad (3.24)$$

$$\mathcal{D} = 4\phi^3 - 6\phi^2 + 2\phi \quad (3.25)$$

$$\int_{\Omega^e} N_A w_A [\beta \dot{\phi} + 3\phi(1 - \phi)\mathcal{C} + N_A \chi \mathcal{D}] + \alpha \nabla N_A \nabla \phi \, dV + \int_{\partial\Omega_\varepsilon} N_A w_A \boldsymbol{\mathcal{E}} \cdot \mathbf{n} \, dS = 0 \quad (3.26)$$

Then the residual vector reads

$$R_\phi^A = \int_{\Omega^e} N_A [\beta \dot{\phi} + 3\phi(1 - \phi)\mathcal{C} + \chi \mathcal{D}] + \alpha \nabla N_A \nabla \phi \, dV + \int_{\partial\Omega_\varepsilon} N_A \boldsymbol{\mathcal{E}} \cdot \mathbf{n} \, dS \quad (3.27)$$

The evolution of the order parameter is calculated in the following manner using backward-Euler method.

$$\dot{\phi} = \frac{\phi_{t+1} - \phi_t}{\Delta t} \quad (3.28)$$

The tangent can be also written in the following manner,

$$K_{\phi\phi}^{AB} = -\frac{\partial R_\phi^A}{\partial \phi^B} = -\int_{\Omega^e} \left[\beta \frac{N_A N_B}{\Delta t} + \alpha \nabla N_A \nabla N_B + 3N_A N_B (1 - 2\phi)\mathcal{C} + N_A N_B \chi \frac{\partial \mathcal{D}}{\partial \phi} \right] dV - \int_{\partial\Omega_\varepsilon} N_A N_B \frac{\partial \boldsymbol{\mathcal{E}}}{\partial \phi} \cdot \mathbf{n} \, dS \quad (3.29)$$

Non-zero off-diagonal terms of stiffness matrix are as follows,

$$K_{\phi c}^{AB} = -\frac{\partial R_\phi^A}{\partial c^B} = -\int_{\Omega^e} 3N_A N_B \phi (1 - \phi) \frac{\partial \mathcal{C}}{\partial c} \, dV \quad (3.30)$$

3.3 Results

The parameters related to the thickness of the interphase region and kinetics of phase interface are found by analyzing 1D equilibrium state of the phases (static interface) following Kim et al. [71]. In the equilibrium state equation (3.2) reduces to,

$$\alpha \frac{\partial^2 \phi}{\partial x^2} = \frac{\partial \psi_0}{\partial \phi} \quad (3.31)$$

A non-equilibrium initial state for the system is used to validate the evolved numerical solution with the analytical one. The initial values for ϕ are varied in the range [0.,1.] with a hyperbolic change in the interphase region, which coincides with the analytically calculated interface profile. The energy σ and the interphase thickness δ can be found as [71],

$$\delta = 2.94 \sqrt{\frac{2\alpha}{\chi}} \quad (3.32)$$

$$\sigma = \frac{\sqrt{2}}{6} \sqrt{\alpha\chi} \quad (3.33)$$

The analytical solution of equation (3.31) for ϕ reads,

$$\phi = \frac{1}{2} \left(1 - \tanh\left(\frac{\sqrt{\chi}}{\sqrt{2\sqrt{\alpha}}}x\right) \right) \quad (3.34)$$

For the normalized concentration, an initial value equal to $c = 0.5$ is used in order to make the system unstable, since at a specific state the homogeneous domain has to segregate into two distinct phases predefined as $c_1 = 0.8$ and $c_2 = 0.2$. In this test an initial condition was defined for the order parameter ϕ and the evolution of the concentration was investigated. A system of two following equations were solved for

the one dimensional problem specified.

$$\begin{cases} \dot{c} = \text{Div}(\mathcal{M}(\phi)\nabla(\frac{\partial\psi(c, \phi, \nabla\phi)}{\partial c})) \\ \alpha \frac{\partial^2\phi}{\partial x^2} = \frac{\partial\psi_0}{\partial\phi} \end{cases} \quad (3.35)$$

The analytical solution was carried out using commercial software MATLAB and for the initial-boundary value problem the following solution was achieved.

$$c = 4.5 \times 10^5 (\tanh(10^5 x - 15)^2 - 1) \quad (3.36)$$

As Results for initial phase value and no flux boundary conditions show, a perfect match between two solutions as depicted in Figure 3.3.

A further analysis is carried out for a 2D model, which would be suitable for simulation of oxidation phenomena in TBC systems in the non-equilibrium state with a moving interface. To this end, the actual concentration used in equation (3.8) for c_1 and c_2 are 0.14 and 0.90 respectively. Parameters used in the analysis can be found in Table 3.1. An initial condition obeying equation (3.34) is given for the phase field and the concentration in the domain. The initial condition in the domain is defined by a hyperbolic function with the minimum and the maximum values 0.12 and 0.92 for the normalized concentration and $\phi = 0$ and $\phi = 1$ for the order parameter at the right and left domains, respectively (Figure 3.4). These values are adopted in order to trigger diffusion, boundary conditions are supersaturated and undersaturated at two sides of the interface.

In Figure 3.2 it can be seen that the phase transition interphase region length should be in nano-meters scale, however due to the limitations in the computational power the length is set to total length of $1\mu\text{m}$. A mesh dependency test was carried out for $1\mu\text{m}$, $0.5\mu\text{m}$ and $0.25\mu\text{m}$ size quadrilateral elements. The results for concentration are given in the Figure 3.4. It can be observed that $0.5\mu\text{m}$ size mesh is small enough to provide a mesh independent solution.

Figure 3.6 shows the propagation of the phase interface in the domain. The evolution of the interphase concentration profile with respect to time is also presented in Figure

Table 3.1: Material and analysis parameters at 1200°C

Material parameters	Value	Unit
D	1.6×10^{-13}	$\text{m}^3 \cdot \text{s}$
β	$1. \times 10^8$	—
α	1×10^{-10}	m^2
χ	0.392	—
k_1	8.314	$\text{J} \cdot \text{mol}^{-1} \cdot \text{m}^{-3}$
k_2	8.314	$\text{J} \cdot \text{mol}^{-1} \cdot \text{m}^{-3}$
c_1	0.90	—
c_2	0.14	—

3.7.

A parameteric study was conducted to investigate the effect of the change in the G-L parameters α and k . According to the equation (3.32) an increase in the α should increase the thickness of interphase region, which can be clearly observed in the results in Figure 3.8.

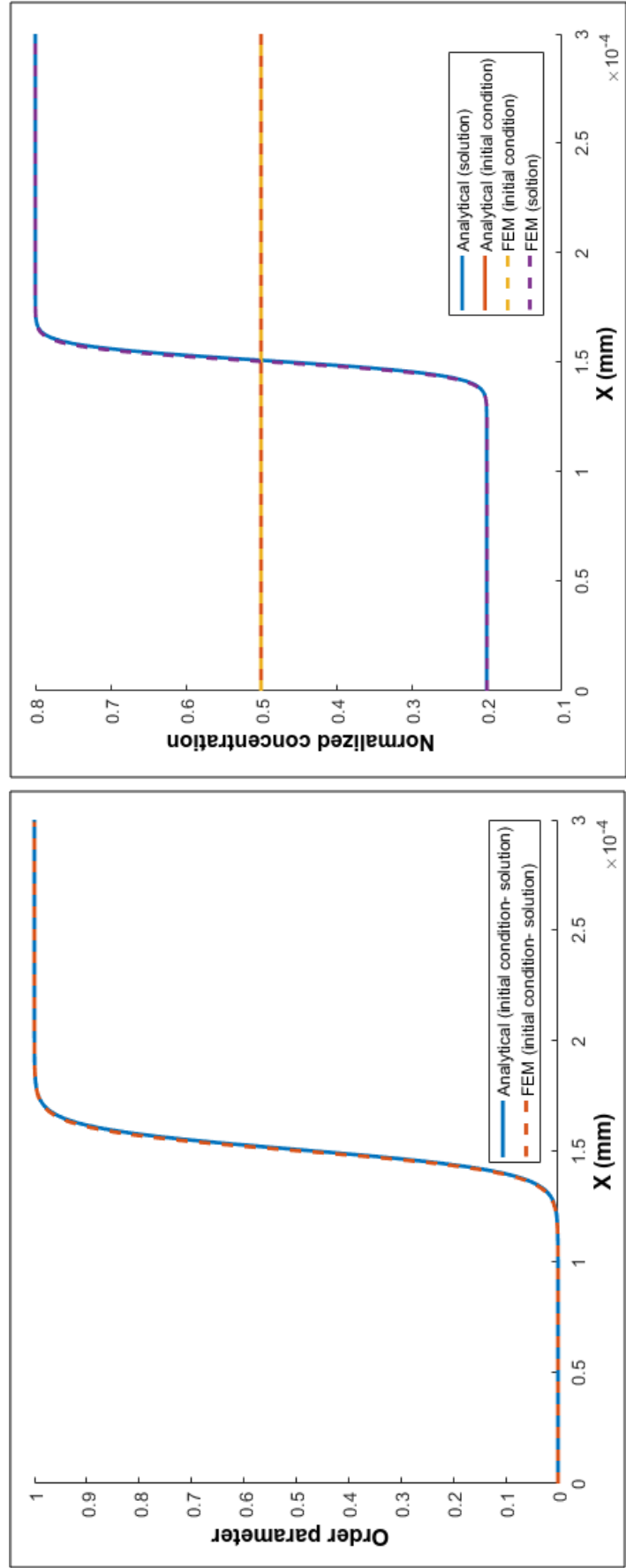


Figure 3.3: Comparison of analytical and numerical solutions for the phase field and the concentration

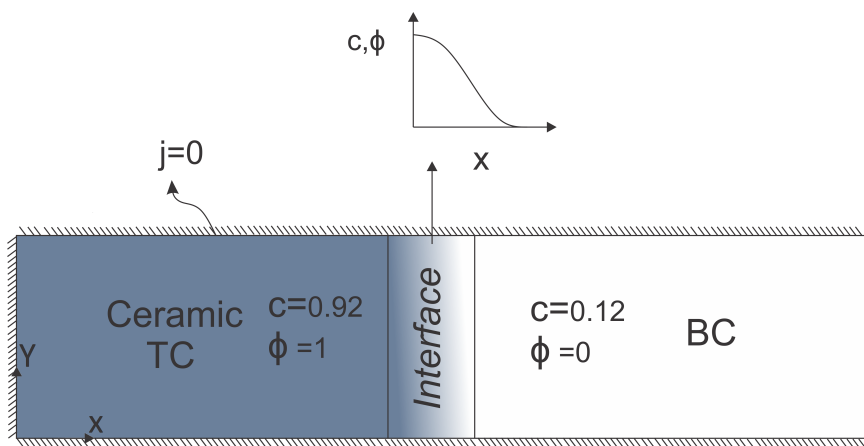


Figure 3.4: Schematic of hyperbolic initial conditions and no-flux boundary condition imposed on the model

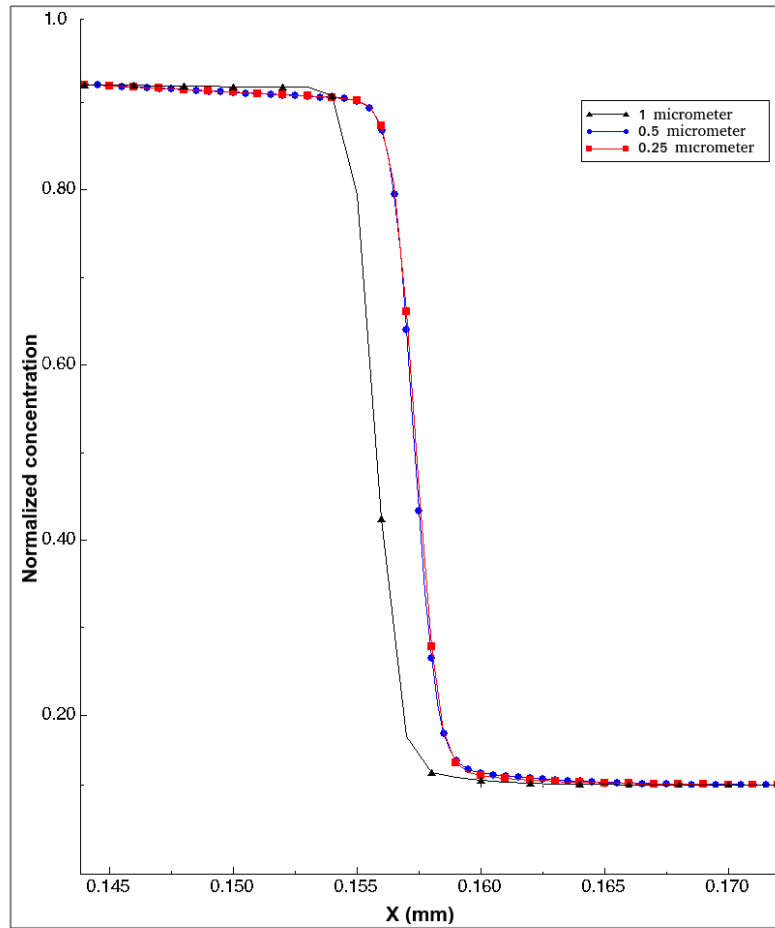


Figure 3.5: Normalized concentration profile after 10 hrs for different mesh sizes.

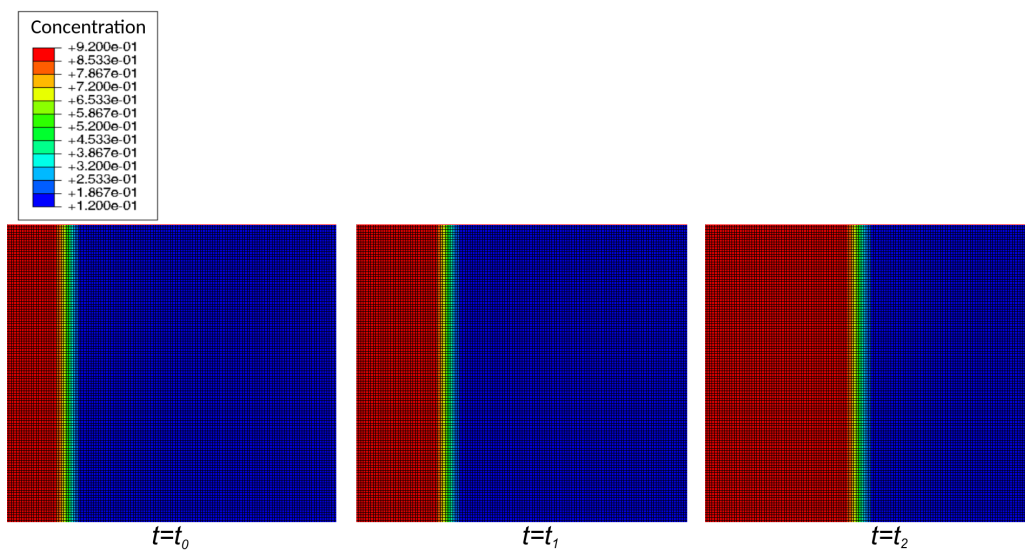


Figure 3.6: Normalized concentration contour evolution in time $t_0 < t_1 < t_2$.

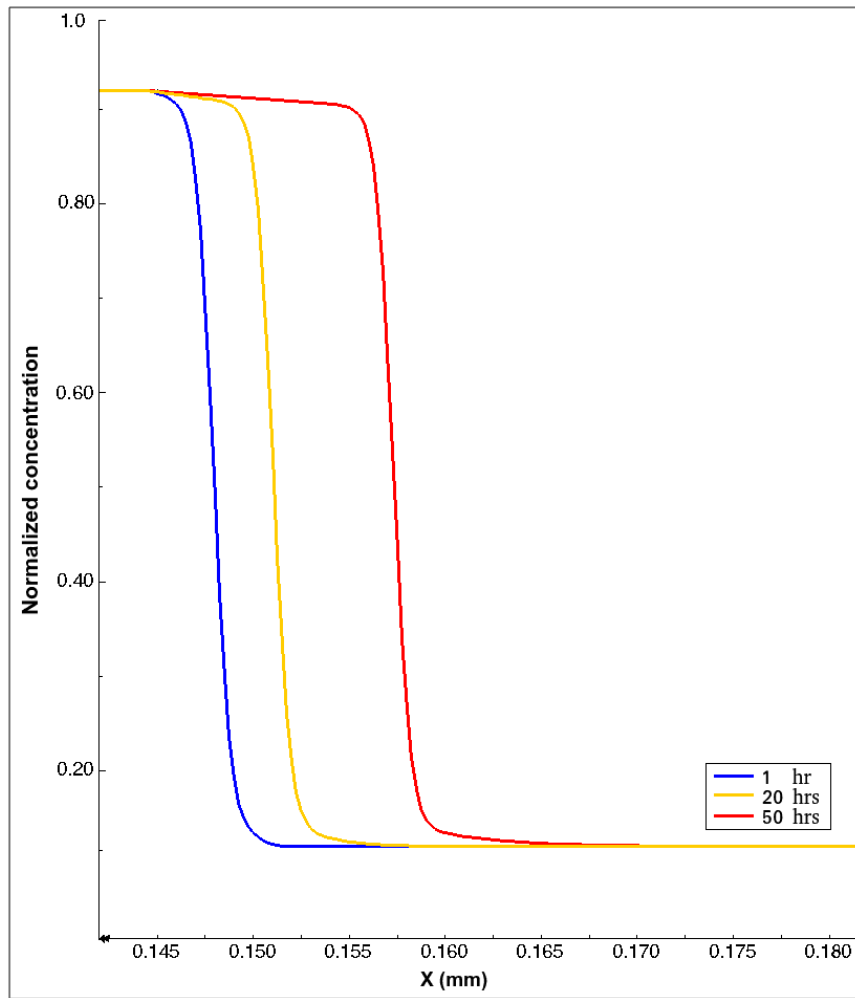


Figure 3.7: Time evolution of the interfacial concentration in 50 hrs.

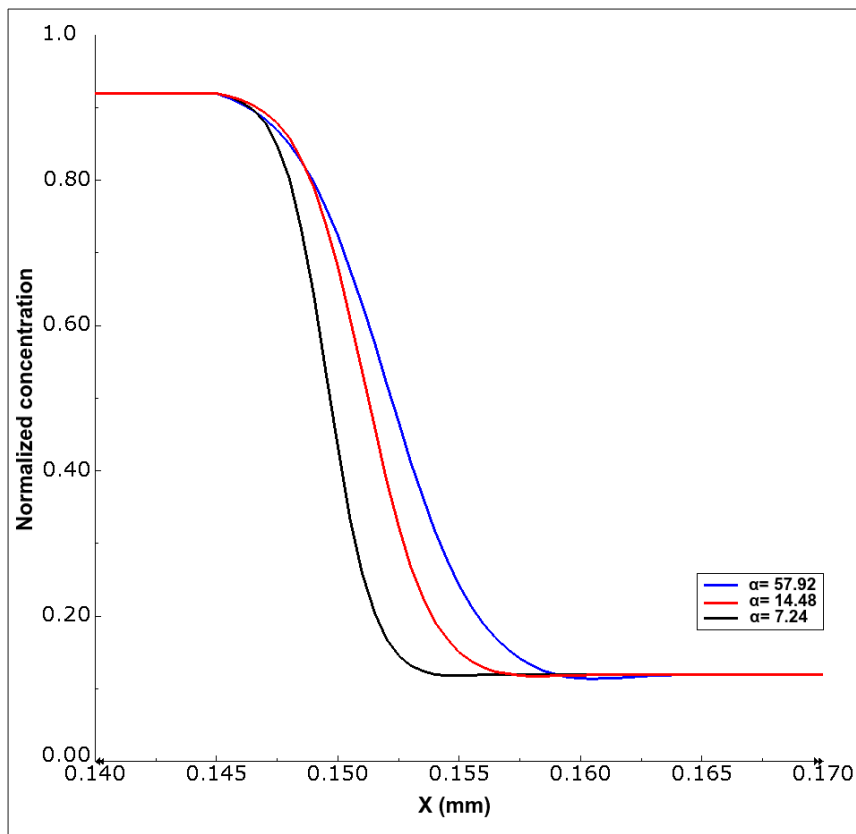


Figure 3.8: Diffuse interface thickness for different values of α .

CHAPTER 4

PHASE TRANSFORMATION AND DEFORMATION COUPLED ANALYSIS

4.1 Kinematics

Considering a smooth function $\mathbf{x} = \chi(\mathbf{X}, t)$ mapping the motion of a point of body B in the reference configuration denoted by \mathbf{X} to the spatial point \mathbf{x} at time t , the deformation gradient, the velocity, the velocity gradient and the Jacobian are given by

$$\mathbf{F} = \nabla\chi, \quad \mathbf{v} = \dot{\chi}, \quad \mathbf{L} = \text{grad}(\mathbf{v}) = \dot{\mathbf{F}}\mathbf{F}^{-1}, \quad J = \det\mathbf{F} \quad (4.1)$$

Note that vectors and second order tensors are shown in bold. The Kröner's decomposition [85] is used for the deformation gradient,

$$\mathbf{F} = \mathbf{F}^e \mathbf{F}^i \quad (4.2)$$

where \mathbf{F}^e is the elastic distortion which represents the stretch and rotation and \mathbf{F}^i is the inelastic distortion. Then the velocity gradient is decomposed in the following form.

$$\mathbf{L} = \mathbf{L}^e + \mathbf{F}^e \mathbf{L}^i \mathbf{F}^{e-1} \quad (4.3)$$

where,

$$\mathbf{L}^e = \dot{\mathbf{F}}^e \mathbf{F}^{e-1}, \quad \mathbf{L}^i = \dot{\mathbf{F}}^i \mathbf{F}^{i-1} \quad (4.4)$$

The right polar decomposition of \mathbf{F}^e yields,

$$\mathbf{F}^e = \mathbf{R}^e \mathbf{U}^e \quad (4.5)$$

in terms of the right stretch tensor \mathbf{U}^e and the rotation tensor \mathbf{R}^e . The Hencky's strain,

$$\mathbf{E}^e = \ln(\mathbf{U}^e) \quad (4.6)$$

is chosen as the strain measure. Following the decomposition given in equation (4.2), the Jacobian can also be decomposed as,

$$J = J^e J^i, \quad J^e = \det \mathbf{F}^e > 0, \quad J^i = \det \mathbf{F}^i > 0. \quad (4.7)$$

The elastic and inelastic stretching and spin tensors are,

$$\mathbf{D}^e = \text{sym} \mathbf{L}^e, \quad \mathbf{D}^i = \text{sym} \mathbf{L}^i \quad (4.8)$$

$$\mathbf{W}^e = \text{skew} \mathbf{L}^e, \quad \mathbf{W}^i = \text{skew} \mathbf{L}^i \quad (4.9)$$

Assuming an irrotational plastic flow i.e.,

$$\mathbf{W}^i = 0 \quad (4.10)$$

the total inelastic deformation gradient would be,

$$\dot{\mathbf{F}}^i = \mathbf{D}^i \mathbf{F}^i. \quad (4.11)$$

The total stretching tensor is decomposed in an additive manner [50],

$$\mathbf{D} = \mathbf{D}^e + \mathbf{D}^i. \quad (4.12)$$

From here on, the equations defining the plastic response of the different layers are formulated separately for the top-coat ceramic material and the bond-coat/TGO two-phase material.

Inelastic stretching tensor for a multiphase region (the bond-coat and the TGO) is defined as,

$$\mathbf{D}^i = \mathbf{D}^s + \mathbf{D}^p \quad (4.13)$$

where \mathbf{D}^s is the swelling stretching and \mathbf{D}^p is due to the viscoplastic deformation. The swelling stretching \mathbf{D}^s due to oxidation is defined as below,

$$\mathbf{D}^s = \dot{\phi} \mathbf{S} \quad (4.14)$$

where ϕ is the phase field variable defining the content of the new phase in the region, and \mathbf{S} is the swelling strain tensor defined using β_l (normal to interface), β_t (in-plane) growth parameters [10, 86] and \mathbf{n} is the surface normal to the interface profile as follows.

$$\mathbf{S} = \beta_l \mathbf{n} \otimes \mathbf{n} + \beta_t (\mathbf{1} - \mathbf{n} \otimes \mathbf{n}) \quad (4.15)$$

\mathbf{D}^p is assumed to be the volume average of inelastic stretching of the bond-coat and the TGO, i.e.,

$$\mathbf{D}^p = (1 - \phi) \mathbf{D}_{bc}^p + \phi \mathbf{D}_{ox}^p \quad (4.16)$$

where \mathbf{D}_{bc}^p and \mathbf{D}_{ox}^p are the viscoplastic flow rate in the bond-coat and the TGO respectively. For both the oxide ($\alpha = ox$) and the bond-coat material ($\alpha = bc$) the plastic stretching is

$$\mathbf{D}_\alpha^p = \sqrt{\frac{3}{2}} \mathbf{N}^p \dot{\tilde{\epsilon}}_\alpha^p \quad (4.17)$$

where $\dot{\tilde{\epsilon}}_\alpha^p$ is the plastic strain rate. \mathbf{N}^p is the plastic flow direction and assumed to be colinear to the Mandel stress \mathbf{M}^e and codirectional for both phases. The second Piola

stress can be expressed as,

$$\mathbf{T}^e = \mathbf{F}^{e-1} \mathbf{F}^{e-T} \mathbf{M}^e \quad (4.18)$$

Thus, the Cauchy stress can be computed using the equation below.

$$\mathbf{T} = J^{-1} \mathbf{F}^e \mathbf{M}^e \mathbf{F}^{eT} \quad (4.19)$$

Under isotropy assumption the Cauchy stress may also be expressed as [41],

$$\mathbf{T} = J^{-1} \mathbf{R}^e \mathbf{M}^e \mathbf{R}^{eT} \quad (4.20)$$

The first Piola stress then reads,

$$\mathbf{T}_R = J \mathbf{T} \mathbf{F}^{-T} \quad (4.21)$$

Calculating the deviatoric part of the Mandel Stress,

$$\mathbf{M}_0^e = \mathbf{M}^e - \frac{1}{3} \text{tr}(\mathbf{M}^e) \mathbf{1} \quad (4.22)$$

the plastic flow direction is expressed as,

$$\mathbf{N}^p = \sqrt{\frac{3}{2}} \frac{\mathbf{M}_0^e}{\bar{\sigma}} \quad (4.23)$$

where $\bar{\sigma}$ is the equivalent stress. The equivalent stress is defined as,

$$\bar{\sigma} = \sqrt{\frac{3}{2}} |\mathbf{M}_0^e| \quad (4.24)$$

The microforce balance including a power-law rate dependence reads,

$$\bar{\sigma} = g(S_\alpha, \dot{\bar{\epsilon}}_\alpha^p) = S_\alpha \left(\frac{\dot{\bar{\epsilon}}_\alpha^p}{\dot{\bar{\epsilon}}_0} \right)^m + \Delta t h \dot{\bar{\epsilon}}_\alpha^p \quad \text{when } \dot{\bar{\epsilon}}_\alpha^p > 0 \quad (4.25)$$

Parameter S_α is known as the material or deformation saturation resistance. m is the rate sensitivity parameter, $\dot{\epsilon}_0$ is the reference plastic flow rate and h is the hardening parameter.

4.2 Balance Equations

The balance equations solved through the numerical process are presented below. The definitions for the variables used in this section is given in Table 4.1. Neglecting inertial effects in the body, the balance of linear momentum can be expressed as,

$$\text{Div}(\mathbf{T}_R) + \mathbf{b} = 0 \quad (4.26)$$

where \mathbf{T}_R and \mathbf{b} are the 1st Piola-Kirchhoff stress tensor and the body force vector, respectively. The isotropic version of the Allen-Cahn phase field model, which is also known as time dependent Ginzburg-Landau model is used previously by [43] for the modeling of oxide growth in a bulk metal. In contrast to bulk metal oxidation, the TGO/bond-coat interface profile would not undergo shape smoothing evolution. The isotropic model is then incapable of maintaining the interface profile shape, due to the interface smoothing solution of the phase kinetic equations. In other words, in the case of undulation smoothing, the Fick's and the Allen-Cahn (Ginzburg-Landau) models work pretty well since according to the nature of these equations, gradients of the concentration and field variable in 3D affect the solution. The surface smoothening property of the Fick's law can be accepted to be physically feasible, since normally it is used to express diffusion of a phase in another one and retreat of species from regions already occupied by the diffusing phase is possible. However, in the case of oxidation and TGO interface propagation, an already oxidized region can not get back to the base metal. To demonstrate this difficulty the classical Allen-Cahn model is implemented for undulated interface and results for phase propagation are presented in Figure 4.1.

To overcome this handicap of the Allen-Cahn model, the model is extended such that it allows anisotropic interface propagation in accordance with the experimental observations.

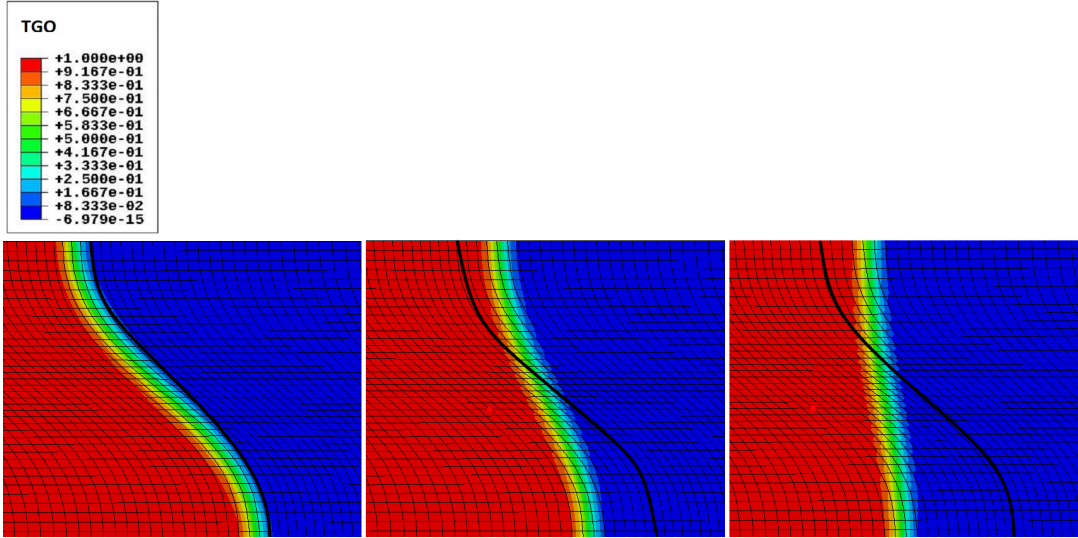


Figure 4.1: Phase propagation with an initially undulated surface.

The anisotropic Fick's law can be expressed as below,

$$\dot{c} = \text{Div}(\mathcal{M}\nabla(\frac{\partial\psi_0(\Phi)}{\partial c})) \quad (4.27)$$

where the symmetric second order tensor \mathcal{M} is expressed as,

$$\mathcal{M} = \begin{bmatrix} \mathcal{M}_{11} & \mathcal{M}_{12} & \mathcal{M}_{13} \\ \mathcal{M}_{12} & \mathcal{M}_{22} & \mathcal{M}_{23} \\ \mathcal{M}_{13} & \mathcal{M}_{23} & \mathcal{M}_{33} \end{bmatrix}$$

Then the Fick's law can be written in the following explicit manner for two-dimensional problems,

$$\dot{c} = \mathcal{M}_{11} \frac{\partial^2\psi_0(\Phi)_{,c}}{\partial x_1^2} + 2\mathcal{M}_{12} \frac{\partial^2\psi_0(\Phi)_{,c}}{\partial x_1\partial x_2} + \mathcal{M}_{22} \frac{\partial^2\psi_0(\Phi)_{,c}}{\partial x_2^2} \quad (4.28)$$

where $(\cdot)_{,c} = \frac{\partial(\cdot)}{\partial c}$.

For our purpose defining $\mathcal{M}_{22} \gg \mathcal{M}_{11} \simeq \mathcal{M}_{12}$ results undulation shape maintenance, since undulation profile has a large gradient in transverse direction. Thus neglecting

minor terms,

$$\dot{c} = \mathcal{M}_{11} \frac{\partial^2 \psi_0(\Phi),c}{\partial x_1^2} \quad (4.29)$$

In a similar way a modification is needed for the G-L equation. The standard G-L equation reads

$$\beta \dot{\phi} = \alpha \Delta \phi - \frac{\partial \psi_0}{\partial \phi} \quad (4.30)$$

Parameter α now can be defined as a tensor. With this modification equation (4.30) can be rewritten in the following form.

$$\beta \dot{\phi} = \text{Div}(\boldsymbol{\alpha} \nabla \phi) - \frac{\partial \psi_0}{\partial \phi} \quad (4.31)$$

The symmetric α matrix is defined as,

$$\boldsymbol{\alpha} = \begin{bmatrix} \alpha_{11} & \alpha_{12} & \alpha_{13} \\ \alpha_{12} & \alpha_{22} & \alpha_{23} \\ \alpha_{13} & \alpha_{23} & \alpha_{33} \end{bmatrix}$$

Then equation (4.31) can be expressed as,

$$\beta \dot{\phi} = \alpha_{11} \frac{\partial^2 \phi}{\partial x_1^2} + 2\alpha_{12} \frac{\partial^2 \phi}{\partial x_1 \partial x_2} + \alpha_{22} \frac{\partial^2 \phi}{\partial x_2^2} - \frac{\partial \psi_0}{\partial \phi} \quad (4.32)$$

Assuming $\alpha_{22} \gg \alpha_{11} \simeq \alpha_{12}$ is assumed. Neglecting the minor terms,

$$\beta \dot{\phi} = \alpha_{11} \frac{\partial^2 \phi}{\partial x_1^2} - \frac{\partial \psi_0}{\partial \phi} \quad (4.33)$$

Implementing the modified model, the phase propagation changes as shown in Figure 4.2.

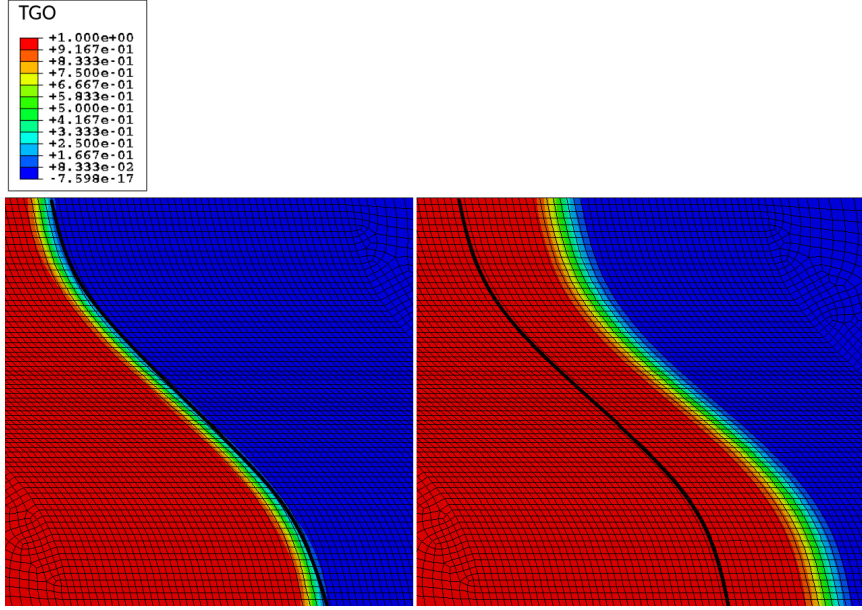


Figure 4.2: Phase propagation in undulated surface after modification.

In conclusion, the modified equations for the normalized concentration of species c ($0 \leq c \leq 1$) and the phase field ϕ ($0 \leq \phi \leq 1$) balance proposed in [86] are as follows,

$$\dot{c} = \text{Div}(\mathcal{M}\nabla(\frac{\partial\psi_0(c, \phi, \mathbf{E}^e)}{\partial c})) \quad (4.34)$$

$$\beta\dot{\phi} = \text{Div}(\boldsymbol{\alpha}\nabla\phi) - \frac{\partial\psi_0}{\partial\phi} \quad (4.35)$$

where ψ_0 , \mathcal{M} , $\boldsymbol{\alpha}$ and β represent the free energy density, the mobility tensor, a tensorial and a scalar phase field parameter, respectively. Furthermore, following [87] an auxiliary equation is defined with a scalar parameter π , providing the gradient of $\text{tr}(\mathbf{E}^e)$ term needed in numerical implementation of the equations coupling diffusion and mechanical solutions.

$$P = \pi\text{tr}(\mathbf{E}^e) \quad (4.36)$$

In the equation above, P is a scalar auxiliary field variable, and \mathbf{E}^e is the elastic strain

tensor. Briefly, the system of equations solved for the analysis is as follows,

$$\begin{cases} \text{Div}(\mathbf{T}_R) + \mathbf{b} = 0 \\ \dot{c} = \text{Div}(\mathcal{M}\nabla(\frac{\partial\psi_0(c, \phi, \mathbf{E}^e)}{\partial c})) \\ \beta\dot{\phi} = \text{Div}(\boldsymbol{\alpha}\nabla\phi) - \frac{\partial\psi_0}{\partial\phi} \\ P = \pi\text{tr}(\mathbf{E}^e) \end{cases} \quad (4.37)$$

Following [88, 89] neglecting the kinetic energy, and assuming that the variation of any independent variable in the system will cause an energy change, the balance of energy in the reference configuration can be written as,

$$\begin{aligned} \frac{d}{dt} \int_V \varepsilon dV = & \int_S (\mathbf{T}_R \mathbf{n}) \cdot \mathbf{v} dS + \int_V \mathbf{b} \cdot \mathbf{v} dV - \int_S \mathbf{q} \cdot \mathbf{n} dS + \int_V q dV \\ & - \int_S \mu \mathbf{j} \cdot \mathbf{n} dS - \int_V \mathcal{P} \dot{\phi} dV + \int_V \boldsymbol{\mathcal{E}} \cdot \nabla \dot{\phi} dV \end{aligned} \quad (4.38)$$

where ε , \mathbf{j} , \mathcal{P} and $\boldsymbol{\mathcal{E}}$ are the internal energy, species flux, energy conjugate variables of ϕ and $\nabla\phi$, respectively. μ , \mathbf{q} and q represent the chemical potential, the heat flux and the external heat supply.

The term with species flux \mathbf{j} in the equation above refers to the amount of energy carried into the system by diffusing species. Application of divergence theorem leads to

$$\begin{aligned} \int_V \left[\frac{d\varepsilon}{dt} - [\text{Div}(\mathbf{T}_R) + \mathbf{b}] \cdot \mathbf{v} - \mathbf{T}_R : \dot{\mathbf{F}} + \text{Div}(\mathbf{q}) - q + \mu \text{Div}(\mathbf{j}) + \mathbf{j} \cdot \nabla \mu \right. \\ \left. + \mathcal{P} \dot{\phi} - \boldsymbol{\mathcal{E}} \cdot \nabla \dot{\phi} \right] dV = 0. \end{aligned} \quad (4.39)$$

Knowing the local balance of diffusion equation,

$$\dot{c} = -\text{Div}(\mathbf{j}), \quad (4.40)$$

equation (4.39) can be written as,

$$\dot{\varepsilon} = \mathbf{T}_R : \dot{\mathbf{F}} - \text{Div}(\mathbf{q}) + q + \mu\dot{c} - \mathbf{j} \cdot \nabla\mu - \mathcal{P}\dot{\phi} + \boldsymbol{\varepsilon} \cdot \nabla\dot{\phi} \quad (4.41)$$

The second law of thermodynamics for the imbalance of entropy (η) reads,

$$\frac{d}{dt} \int_V \eta dV \geq \int_V \frac{q}{\nu} dV - \int_S \frac{\mathbf{q} \cdot \mathbf{n}}{\nu} dS \quad (4.42)$$

where ν is the temperature. Using the divergence theorem, the energy balance equation and also keeping in mind that $\frac{\mathbf{q}}{\nu}$ (Entropy flow) is present, whenever the heat flux is available and neither of them can vanish without the other one [88], one can write,

$$\dot{\eta} \geq \frac{q}{\nu} - \text{Div}\left(\frac{\mathbf{q}}{\nu}\right) \quad (4.43)$$

Then using equations (4.41) and (4.43) one obtains,

$$(\dot{\varepsilon} - \nu\dot{\eta}) - \mathbf{T}_R : \dot{\mathbf{F}} - \mu\dot{c} + \frac{1}{\nu}\mathbf{q} \cdot \nabla\nu + \mathbf{j} \cdot \nabla\mu + \mathcal{P}\dot{\phi} - \boldsymbol{\varepsilon} \cdot \nabla\dot{\phi} \leq 0 \quad (4.44)$$

Having introduced a specific free energy,

$$\psi = \varepsilon - \nu\eta \quad (4.45)$$

the following local imbalance of energy can be written,

$$\dot{\psi} + \eta\dot{\nu} - \mathbf{T}_R : \dot{\mathbf{F}} - \mu\dot{c} + \frac{1}{\nu}\mathbf{q} \cdot \nabla\nu + \mathbf{j} \cdot \nabla\mu + \mathcal{P}\dot{\phi} - \boldsymbol{\varepsilon} \cdot \nabla\dot{\phi} \leq 0 \quad (4.46)$$

4.3 Constitutive Equations

Considering the balance of energy found in the previous section, following forms are assumed for the free energy, the stress, the chemical potential and the entropy.

$$\left\{ \begin{array}{l} \psi = \bar{\psi}(\Phi) \\ \mathbf{T}^e = \bar{\mathbf{T}}(\Phi) \\ \mu = \bar{\mu}(\Phi) \\ \eta = \bar{\eta}(\Phi) \\ \mathcal{P} = \bar{\mathcal{P}}(\Phi) \\ \mathcal{E} = \bar{\mathcal{E}}(\Phi) \end{array} \right. \quad (4.47)$$

where Φ represents the set of variables $\{\mathbf{C}^e, \nu, c, \phi, \nabla\phi\}$. Stress power for a unit volume of the material may be written as

$$\begin{aligned} \mathbf{T}_R : \dot{\mathbf{F}} &= \mathbf{T}_R : (\dot{\mathbf{F}}^e \mathbf{F}^i + \mathbf{F}^e \dot{\mathbf{F}}^i) \\ &= (J\mathbf{F}^{e-1} \mathbf{T} \mathbf{F}^{e-T}) : (\mathbf{F}^{eT} \dot{\mathbf{F}}^e) + (\mathbf{C}^e J\mathbf{F}^{e-1} \mathbf{T} \mathbf{F}^{e-T}) : \mathbf{L}^i \end{aligned} \quad (4.48)$$

Knowing that the right Cauchy-Green tensor is defined as,

$$\mathbf{C}^e = \mathbf{F}^{eT} \mathbf{F}^e \quad (4.49)$$

then the time derivative reads

$$\dot{\mathbf{C}}^e = \mathbf{F}^{eT} \dot{\mathbf{F}}^e + \mathbf{F}^{eT} \dot{\mathbf{F}}^e \quad (4.50)$$

Thus using equation (4.18), (4.19) and (4.50) the stress power (4.48) for a unit volume of the multiphase material can be written as,

$$\mathbf{T}_R : \dot{\mathbf{F}} = \frac{1}{2} \mathbf{T}^e : \dot{\mathbf{C}}^e + \mathbf{M}^e : \mathbf{L}^i \quad (4.51)$$

Then using equation (5.8), (4.14) and (4.16)

$$\mathbf{T}_R : \dot{\mathbf{F}} = \frac{1}{2} \mathbf{T}^e : \dot{\mathbf{C}}^e + (1 - \phi) \mathbf{M}^e : \mathbf{D}_{bc}^p + \phi \mathbf{M}^e : \mathbf{D}_{ox}^p + \dot{\phi} \mathbf{M}^e : \mathbf{S} \quad (4.52)$$

Then the free energy imbalance equation (4.46) can be written as,

$$\begin{aligned} \dot{\psi} + \eta \dot{\nu} - \frac{1}{2} \mathbf{T}^e : \dot{\mathbf{C}}^e - (1 - \phi) \mathbf{M}^e : \mathbf{D}_{bc}^p - \phi \mathbf{M}^e : \mathbf{D}_{ox}^p - \dot{\phi} \mathbf{M}^e : \mathbf{S} \\ - \mu \dot{c} + \frac{1}{\nu} \mathbf{q} \cdot \nabla \nu + \mathbf{j} \cdot \nabla \mu + \mathcal{P} \dot{\phi} - \boldsymbol{\varepsilon} \cdot \nabla \dot{\phi} \leq 0 \end{aligned} \quad (4.53)$$

Considering the dependence of the free energy given in equation (4.47), it is possible to reformulate equation (4.53) as,

$$\begin{aligned} \left(\frac{\partial \psi(\Phi)}{\partial \mathbf{C}^e} - \frac{1}{2} \mathbf{T}^e \right) : \dot{\mathbf{C}}^e + \dot{\nu} \left(\frac{\partial \psi(\Phi)}{\partial \nu} + \eta \right) - (1 - \phi) \mathbf{M}^e : \mathbf{D}_{bc}^p - \phi \mathbf{M}^e : \mathbf{D}_{ox}^p \\ - \dot{\phi} \left(\mathbf{M}^e : \mathbf{S} - \frac{\partial \psi(\Phi)}{\partial \phi} + \mathcal{P} \right) - \left(\mu - \frac{\partial \psi(\Phi)}{\partial c} \right) \dot{c} + \left(\frac{\partial \psi(\Phi)}{\partial \nabla \phi} - \boldsymbol{\varepsilon} \right) \nabla \dot{\phi} \\ + \frac{1}{\nu} \mathbf{q} \cdot \nabla \nu + \mathbf{j} \cdot \nabla \mu \leq 0 \end{aligned} \quad (4.54)$$

This equation must hold for all values of Φ . Therefore, the following equations can be inferred,

$$\left\{ \begin{array}{l} \mathbf{T}^e = 2 \frac{\partial \psi(\Phi)}{\partial \mathbf{C}^e} \\ \eta = - \frac{\partial \psi(\Phi)}{\partial \nu} \\ \mu = \frac{\partial \psi(\Phi)}{\partial c} \\ \boldsymbol{\varepsilon} = \frac{\partial \psi(\Phi)}{\partial \nabla \phi} \\ \mathcal{P} = \frac{\partial \psi(\Phi)}{\partial \phi} - \mathbf{M}^e : \mathbf{S} \end{array} \right. \quad (4.55)$$

with dissipative thermodynamic force \mathcal{P} and energetic constitutive response function

\tilde{A} ,

$$\tilde{A}(\Phi) = -\frac{\partial\psi(\Phi)}{\partial\phi} \quad (4.56)$$

Then the inequality simplifies to the following form,

$$(1 - \phi)\mathbf{M}^e : \mathbf{D}_{bc}^p + \phi\mathbf{M}^e : \mathbf{D}_{ox}^p - \frac{1}{\nu}\mathbf{q} \cdot \nabla\nu - \mathbf{j} \cdot \nabla\mu \geq 0 \quad (4.57)$$

Using the heat conduction equation $\mathbf{q} = -\mathbf{K}\nabla\nu$, diffusion of species (4.34), and defining \mathbf{K} as the thermal conductivity tensor and \mathcal{M} as the mobility tensor, inequality (4.57) can be rewritten as,

$$(1 - \phi)\mathbf{M}^e : \mathbf{D}_{bc}^p + \phi\mathbf{M}^e : \mathbf{D}_{ox}^p + \frac{1}{\nu}\mathbf{K}\nabla\nu \cdot \nabla\nu + \mathcal{M}\nabla\mu \cdot \nabla\mu \geq 0 \quad (4.58)$$

4.4 Specialization of the Constitutive equations

4.4.1 Bond-coat

Considering the Allen-Cahn definition of total free energy density, ψ is given by,

$$\psi(\Phi) = \psi_0(\Phi) + \frac{1}{2}\nabla\phi \cdot (\boldsymbol{\alpha}\nabla\phi) \quad (4.59)$$

As a consequence of isotropy of the material, the free energy density, given in terms of $\Phi(\mathbf{C}^e, \nu, c, \phi, \nabla\phi)$, can also be defined in terms of $\Phi(\mathbf{E}^e, \nu, c, \phi, \nabla\phi)$ [41]. A specific form of free energy density for isothermal analysis can be written as,

$$\psi_0(\Phi) = \psi^M(\phi, \mathbf{E}^e) + \psi^\phi(\phi, c) + \psi^P(\phi, \mathbf{E}^e, c) \quad (4.60)$$

with mechanical part of the free energy density defined as,

$$\psi^M(\phi, \mathbf{E}^e) = G(\phi)|\mathbf{E}^e|^2 + \frac{1}{2}[K(\phi) - \frac{2}{3}G(\phi)]\text{tr}(\mathbf{E}^e)^2 \quad (4.61)$$

where $G(\phi)$ and $K(\phi)$ denote the shear and the bulk modulus of the two phase material, respectively. Material properties which have phase field variable dependency are defined as a linear function of phase field.

$$K(\phi) = K_{bc}(1 - \phi) + K_{ox}\phi \quad (4.62)$$

$$G(\phi) = G_{bc}(1 - \phi) + G_{ox}\phi \quad (4.63)$$

The phase field part is adapted from [90],

$$\psi^\phi(\phi, c) = \phi^2(3 - 2\phi)\psi_1(c) + [1 - \phi^2(3 - 2\phi)]\psi_2(c) + \chi\phi^2(1 - \phi)^2 \quad (4.64)$$

$$\psi_i(c) = \frac{1}{2}k_i(c - c_i)^2 \quad (i = 1, 2) \quad (4.65)$$

where k_i and χ are material phase parameters. c_1 and c_2 are the maximum and minimum normalized concentration of species in the domain. The coupling part of the free energy density is formulated as,

$$\psi^P(\phi, \mathbf{E}^e, c) = -c_{max}K(\phi)P(c - c_0) \quad (4.66)$$

where c_{max} is the maximum oxygen concentration in the alumina [91] and c_0 is the initial normalized concentration.

Using (4.18), (4.55), (4.60) and (4.59), the Mandel Stress \mathbf{M}^e , dissipative thermodynamic force $\tilde{A}(\Phi)$, \mathcal{E} and \mathcal{P} can be derived in the following form,

$$\mathbf{M}^e = 2G\mathbf{E}^e + \lambda\text{tr}(\mathbf{E}^e)\mathbf{1} \quad (4.67)$$

$$\tilde{A}(\Phi) = (3\phi - 2)(\psi_1 - \psi_2) - 2\chi\phi(1 - \phi)(1 - 2\phi) - (K_{ox} - K_{bc})(c - c_0)c_{max}P \quad (4.68)$$

$$\mathcal{E} = 2(\boldsymbol{\alpha}\nabla\phi) \quad (4.69)$$

$$\mathcal{P} = \mathbf{M}^e : \mathbf{S} + \tilde{A}(\Phi) \quad (4.70)$$

where, λ is the lame constant and $\mathbf{1}$ is the identity tensor. The chemical potential μ can be calculated using equation (5.16).

$$\mu = k_1(c - c_1)\phi^2(3 - 2\phi) + k_2(c - c_2)(1 - \phi^2(3 - 2\phi)) - c_{max}K(\phi)P \quad (4.71)$$

4.4.2 Topcoat

Creep resistant bond-coats are more desirable due to less interface oxidation roughening under severe thermo-mechanical conditions [92]. However the top-coat creep is believed to be one of the major mechanisms extending coating life via lowering stress levels in the TBC system. Thus, in our modeling attempt, the top-coat creep is considered and a rate-dependent Gurson type plasticity [93] for porous material is adopted to the overall model. In addition to volumetric plasticity, the model can also describe creep relaxation and plastic flow due to deviatoric stresses, [94]. For the top-coat, the pure mechanical free energy density presented in equation (4.61) is considered by taking $\phi = 0$. The plastic stretching tensor is defined as

$$\mathbf{D}^p = \sqrt{\frac{3}{2}}\mathbf{N}^p\frac{\partial\varphi}{\partial\bar{\sigma}} + \frac{1}{3}\frac{\partial\varphi}{\partial\bar{\sigma}^v}\mathbf{1} \quad (4.72)$$

where,

$$\mathbf{N}^p = \sqrt{\frac{3}{2}} \frac{\mathbf{M}_0^e}{\bar{\sigma}} \quad (4.73)$$

$$\bar{\sigma}^v = \frac{1}{3} \text{tr}(\mathbf{M}^e) \quad (4.74)$$

$$\bar{\sigma} = \sqrt{\frac{3}{2}} |\mathbf{M}_0^e| \quad (4.75)$$

In equation (4.72) \mathbf{N}^p , $\bar{\sigma}^v$, $\bar{\sigma}$ and φ are the plastic strain direction, the equivalent volumetric stress, the equivalent deviatoric stress and the viscoplastic potential respectively. In order to include creep in the model the volumetric plastic deformation rate tensor is also added to the plastic deformation rate tensor [95].

The effective equivalent plastic strain rate of the dense material was described using an evolution function formulated for creep at elevated temperatures [96].

$$\dot{\bar{\epsilon}}_m^p = \dot{\epsilon}_0 \left(\frac{\bar{\sigma}_m}{S} \right)^{\frac{1}{m}} \quad (4.76)$$

Expressing a rate-dependent behavior for the porous material, the viscoplastic potential function φ and the effective equivalent stress in the matrix (material without pores) $\bar{\sigma}_m$ are formulated as,

$$\varphi = F(X, m) \left[\frac{\dot{\epsilon}_0 S}{1/m + 1} \left(\frac{\bar{\sigma}_m}{S} \right)^{1/m+1} \right] \quad (4.77)$$

$$\bar{\sigma}_m = \kappa(F)^{\frac{m}{m+1}} \cdot \bar{\sigma} \quad (4.78)$$

where, F is a function amplifying potential due to presence of the voids. κ , m and X represent a porosity parameter, the rate sensitivity parameter and the triaxiality

respectively. F and X are given as,

$$F = A_1 + (A_2 X^2 + A_3)^{(1/m+1)/2} \quad (4.79)$$

$$X = \frac{\bar{\sigma}^v}{\bar{\sigma}} \quad (4.80)$$

where A_1 , A_2 and A_3 are adopted in the specific form introduced in [94]. The evolution of deformation resistance for top-coat material is defined as,

$$\dot{S} = h \dot{\varepsilon}_m^p \left(1 - \frac{S}{S_{sat}}\right)^q \quad (4.81)$$

where S_0 , S_{sat} , q and h respectively denote the initial deformation resistance, the saturation resistance and the hardening parameters.

4.5 Surface Undulation

Surface roughness is usually modeled as a sinusoidal profile, but in order to determine an average value of the wave amplitude in the profile several experiments have been carried out in the literature [45]. Image processing analyses of samples show that a profile can be taken as,

$$y(x) = a \cdot \cos\left(\frac{\pi x}{w}\right) \quad (4.82)$$

Image processing techniques are used to determine the roughness parameters and the interface surface profile. The interface profile function is then approximated as a sinusoidal function by the means of the Fourier transformation. The amplitude and wavelength of the profile are assumed to be equal to the average amplitude value of the TGO-YSZ and TGO-BC interfaces and the average wavelength. This values are found using the images captured by an electron microscope (SEM), see Figure 4.3 [97].

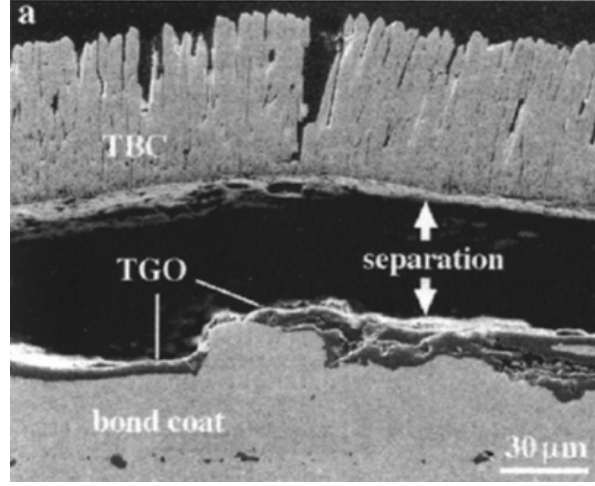


Figure 4.3: Image captured by SEM

The profile amplitude a and wavelength w are set to be equal to $10\mu\text{m}$ and $30\mu\text{m}$ respectively. Then after choosing a proper origin for the coordinate system, the unit normal vector to the surface is found to be,

$$\mathbf{n}_R(x) = \left(-\frac{\pi}{3}\sin\left(\frac{x\pi}{30}\right)\mathbf{i} + \mathbf{j}\right)/N \quad (4.83)$$

where N , i and j are the magnitude of normal vector and unit vectors in horizontal and vertical directions respectively. The unit surface normal vector in the current configuration \mathbf{n} can be found by pushing forward \mathbf{n}_R to the deformed configuration as expressed below [88],

$$\mathbf{n}_R da_R = J\mathbf{F}^T \mathbf{n} da \quad (4.84)$$

and,

$$\mathbf{n} da = J\mathbf{F}^{-T} \mathbf{n}_R da_R \quad (4.85)$$

Then following expression is achieved for the normal vector of the undulated surface,

which can be addressed in the geometry dependent parts of the model.

$$\mathbf{n} = \frac{\mathbf{F}^{-T} \mathbf{n}_R}{|\mathbf{F}^{-T} \mathbf{n}_R|} \quad (4.86)$$

4.6 Numerical Implementation

Implementation of the model is carried out by using a User Element (UEL) subroutine in ABAQUS software. In addition to the displacement degrees of freedom (u_1 and u_2 in two-dimensional problems), the normalized concentration of species (c), the phase field variable (ϕ) and the mechanical coupling term P defined in equation (4.36) are defined as nodal degrees of freedom of the finite element formulation. The extra degree of freedom (P) provides ease in the calculation of its gradient through shape functions. This gradient term is used in the calculation of the residual vector given in equation (4.101) for the normalized concentration, R_c .

For the displacement degrees of freedom the boundary is decomposed into two parts such that $\partial\Omega = \partial\Omega_u \cup \partial\Omega_t$, where Ω_u and Ω_t denote the boundaries where the essential and the natural boundary conditions are prescribed, respectively.

$$\begin{cases} u = u_0 \text{ on } \partial\Omega_u \\ t = t_0 \text{ on } \partial\Omega_t \end{cases} \quad (4.87)$$

$$\text{Div}(\mathbf{T}_R) + \mathbf{b} = 0 \quad (4.88)$$

The boundary conditions and the governing differential equation of the problem are defined.

$$\begin{cases} c = c_0 \text{ on } \partial\Omega_c \\ -D \frac{\partial c}{\partial \mathbf{X}} = \mathbf{j}_0 \text{ on } \partial\Omega_j \end{cases} \quad (4.89)$$

$$\dot{c} = \text{Div}(\mathcal{M}\nabla\left(\frac{\partial\psi_0(c, \phi, \mathbf{E}^e)}{\partial c}\right)) \quad (4.90)$$

The G-L equation the related boundary conditions are as below.

$$\begin{cases} \phi = \phi_0 \text{ on } \partial\Omega_\phi \\ \alpha \frac{\partial\phi}{\partial\mathbf{X}} = \mathcal{E} \text{ on } \partial\Omega_\mathcal{E} \end{cases} \quad (4.91)$$

$$\beta\dot{\phi} = \text{Div}(\alpha\nabla\phi) - \frac{\partial\psi_0}{\partial\phi} \quad (4.92)$$

The additional equation solved for auxiliary field variable is given as

$$P = \pi \text{tr}(\mathbf{E}^e) \quad (4.93)$$

The displacement \mathbf{u} , the mechanical-diffusional coupling term e , the concentration c and the phase field variable ϕ and their spatial derivatives are interpolated with the help of shape functions

$$\mathbf{u} = \sum_{i=1}^n N_i \mathbf{u}_i, \nabla \mathbf{u} = \sum_{i=1}^n \mathbf{B}_i \mathbf{u}_i \quad (4.94)$$

$$e = \sum_{i=1}^n N_i e_i, \nabla e = \sum_{i=1}^n \mathbf{B}_i e_i \quad (4.95)$$

$$c = \sum_{i=1}^n N_i c_i, \nabla c = \sum_{i=1}^n \mathbf{B}_i c_i \quad (4.96)$$

$$\phi = \sum_{i=1}^n N_i \phi_i, \nabla \phi = \sum_{i=1}^n \mathbf{B}_i \phi_i \quad (4.97)$$

The calculated residual vectors and tangent matrices are presented in the equations below. It should be mentioned that implementing off-diagonal terms in the tangent tensor will only effect the convergence speed and will not change final solution of

the problem. The element residual vector and the tangent matrix can be presented as below,

$$\mathbf{R} = \begin{bmatrix} [\mathbf{R}_u] \\ [\mathbf{R}_c] \\ [\mathbf{R}_\phi] \\ [\mathbf{R}_e] \end{bmatrix}$$

$$\mathbf{K} = \begin{bmatrix} [\mathbf{K}_{uu}] & [\mathbf{K}_{uc}] & [\mathbf{K}_{u\phi}] & [\mathbf{K}_{ue}] \\ [\mathbf{K}_{cu}] & [\mathbf{K}_{cc}] & [\mathbf{K}_{c\phi}] & [\mathbf{K}_{ce}] \\ [\mathbf{K}_{\phi u}] & [\mathbf{K}_{\phi c}] & [\mathbf{K}_{\phi\phi}] & [\mathbf{K}_{\phi e}] \\ [\mathbf{K}_{eu}] & [\mathbf{K}_{ec}] & [\mathbf{K}_{e\phi}] & [\mathbf{K}_{ee}] \end{bmatrix}$$

We define,

$$a = k_1\phi^2(3 - 2\phi) + k_2(1 - \phi^2(3 - 2\phi)) \quad (4.98)$$

$$b = k_1(c - c_1) - k_2(c - c_2) \quad (4.99)$$

for a compact representation. Let N_A be the shape function for the interpolation of node A, then the residuals for the displacement \mathbf{u} , phase field ϕ , normalized concentration c and the mechanical coupling term P for each element are expressed as,

$$\mathbf{R}_u = \int_{\Omega^e} (N_A \mathbf{b} - \nabla N_A \mathbf{T}_R) + \int_{\partial\Omega_t} N_A \mathbf{t} dS \quad (4.100)$$

$$\begin{aligned} R_c = \int_{\Omega^e} (N_A \dot{c} + c_{max} K(\phi) \nabla N_A \nabla P - \mathcal{M} a \nabla N_A \nabla c + 6\mathcal{M} b \phi (1 - \phi) \nabla N_A \nabla \phi) dV \\ - \int_{\partial\Omega_j} N_A \mathbf{j} \cdot \mathbf{n} dS = 0 \end{aligned} \quad (4.101)$$

$$R_\phi = \int_{\phi^e} (N_A(\beta\dot{\phi} + 3\phi(1-\phi)\mathcal{C} + \chi\mathcal{D}) + \boldsymbol{\alpha}\nabla N_A\nabla\phi) dV + \int_{\partial\Omega_\varepsilon} N_A\boldsymbol{\mathcal{E}} \cdot \mathbf{n} dS \quad (4.102)$$

$$R_e = \int_{\Omega^e} N_A(P - \pi\text{tr}(\mathbf{E}^e)) dV \quad (4.103)$$

where $\boldsymbol{\mathcal{E}}$ is an energy conjugate for $\nabla\phi$ and scalar values \mathcal{C} and \mathcal{D} are defined as,

$$\mathcal{C} = k_1(c - c_1)^2 - k_2(c - c_2)^2 \quad (4.104)$$

$$\mathcal{D} = 4\phi^3 - 6\phi^2 + 2\phi \quad (4.105)$$

Note that the mobility of the species \mathcal{M} and parameter $\boldsymbol{\alpha}$ are second order tensors. The components of these tensors are chosen such that they prevent lateral propagation of the oxide supporting the experimental results claiming negligible lateral growth against rapid growth in the direction normal to the interface. All the elements of these tensors other than the diagonal element that defines the mobility normal to the interface are assumed to be sufficiently small. This modification results in a controllable oxidation interface profile shape in agreement with the experiments. Neglecting body forces, non-zero elements of the stiffness matrix are derived in the following form,

$$\begin{aligned} \mathbf{K}_{cc}^{AB} = & - \int_{\Omega^e} \left(\frac{N_A N_B}{\Delta t} + a\mathcal{M}\nabla N_A\nabla N_B + 6\mathcal{M}\phi(1-\phi)\frac{\partial b}{\partial c}N_B\nabla N_A\nabla\phi \right) dV \\ & - \int_{\partial\Omega_j} N_A N_B \frac{\partial \mathbf{j}}{\partial c} \cdot \mathbf{n} dS \end{aligned} \quad (4.106)$$

$$\begin{aligned} \mathbf{K}_{\phi\phi}^{AB} = & - \int_{\Omega^e} \left(\beta \frac{N_A N_B}{\Delta t} + \boldsymbol{\alpha}\nabla N_A\nabla N_B + 3N_A N_B(1-2\phi)\mathcal{C} + N_A N_B \chi \frac{\partial \mathcal{D}}{\partial \phi} \right) dV \\ & - \int_{\partial\Omega_\varepsilon} N_A N_B \frac{\partial \boldsymbol{\mathcal{E}}}{\partial \phi} \cdot \mathbf{n} dS \end{aligned} \quad (4.107)$$

$$\mathbf{K}_{ee}^{AB} = - \int_{\Omega^e} (N_A N_B) dV \quad (4.108)$$

$$\mathbf{K}_{c\phi}^{AB} = - \int_{\Omega^e} \left(N_A N_B \frac{\partial K(\phi)}{\partial \phi} + 6b\mathcal{M} \nabla N_A \nabla N_B \right) dV \quad (4.109)$$

$$\mathbf{K}_{ce}^{AB} = - \int_{\Omega^e} (3N_A N_B K(\phi)) dV \quad (4.110)$$

$$\mathbf{K}_{\phi c}^{AB} = - \int_{\Omega^e} (2N_A N_B k_1 \phi (1 - \phi) (c - c_1)) dV \quad (4.111)$$

\mathbf{K}_{uu} for the viscoplastic material is obtained from the work [98].

$$\mathbf{K}_{uu}^{AB} = \int_{\Omega^e} \mathbf{G}^T \mathbf{A} \mathbf{G} dV \quad (4.112)$$

where \mathbf{G} is known as element discrete spatial gradient operator (Appendix D). \mathbf{A} is the consistent tangent modulus.

$$A_{ijkl} = \frac{\partial T_{ij}}{\partial F_{km}} F_{lm} - T_{il} \delta_{jk} \quad (4.113)$$

$$A_{ijkl} = \frac{\partial T_{Rij}}{\partial F_{kl}} \quad (4.114)$$

Details regarding $\frac{\partial \mathbf{T}}{\partial \mathbf{F}}$ for viscoplastic material can be found in Appendix A.

$K_{u\phi}$ can be written as,

$$\mathbf{K}_{u\phi}^{AB} = \int_{\Omega^e} \nabla N_A \frac{\partial \mathbf{T}_R}{\partial \phi} N_B dV \quad (4.115)$$

Expression for $\frac{\partial \mathbf{T}_R}{\partial \phi}$ can be calculated using equations (4.67), (4.62), (4.63) and (A.34) in the following manner. Solution parameters used in the analysis can be

found in Table 4.2. Making an approximation for the derivative of the Piola stress we get

$$\frac{\partial \mathbf{T}_R}{\partial \phi} \approx \frac{\partial \mathbf{M}^e}{\partial \phi} = 2 \frac{\partial G}{\partial \phi} \mathbf{E}^e + \frac{\partial K}{\partial \phi} \text{tr}(\mathbf{E}^e) \mathbf{1} + 2G\mathbf{S} + K\text{tr}(\mathbf{S})\mathbf{1} \quad (4.116)$$

where,

$$\frac{\partial G}{\partial \phi} = G_{ox} - G_m \quad (4.117)$$

$$\frac{\partial K}{\partial \phi} = K_{ox} - K_m \quad (4.118)$$

The rest of the elements in the tangent matrix are either zero or because of complexity adopted as zero.

It should be noted that the residual vector and the tangent matrix for the displacement degrees of freedom are formulized and implemented in the current configuration to keep the symmetry of the tangent tensor following the finite element implementation of Chester [84]. For the rest of the DOFs these vectors and matrices are formulated and implemented in the reference configuration. Mechanical properties are taken from a previous work by He et al. [32], assuming that temperature at interface is around 400°C [99] (see Appendix C for more details).

For the simulation of a TBC system a two-layer geometric model is created with a top-coat and a bond-coat (see Figure 4.4) with a total number of 8235 elements. The problem is assumed to be isothermal at 1200°C . No species flux boundary condition is applied on the left and right edges of the medium. In a similar manner explained in the previous chapter, the phase field and the concentration variables are set as $\phi = 1$ and $c = 0.92$ at the top edge and $\phi = 0$ and $c = 0.12$ at the bottom edge. The initial conditions for the phase field and the concentration variables are consistent with the boundary conditions and follow a hyperbolic tangent transition function in the interphase region. Although the physical length of the transition region is not clearly defined in the literature for a growing oxide in a TBC system, $2\mu\text{m}$ transition length is chosen for the hyperbolic tangent transition function (Figure 4.4). This length is

in accordance with the mesh sizes in the interface region of our finite element model [90, 43]. The displacement of the left edge is constrained in the horizontal direction and the vertical displacement is constrained at the bottom boundary as depicted in Figure 4.5. The right boundary is constrained to remain vertical to mimic the continuity of the sinusoidal pattern in the system. The mesh used has a minimum size of $0.5\mu\text{m}$ as a result of the mesh sensitivity study presented in the previous chapter.

The top-coat/bond-coat interface is magnified in Figure 4.5, where the progression of the oxide front in the bond-coat can be clearly observed. There is no experiment in the literature showing the effect of volumetric pressure on the species diffusion in porous materials to the best knowledge of the authors, but numerical and physical validation of the hypothesis can be observed in the result presented in Figure 4.6. The results show that for higher values of the parameter π the TGO growth speed is lower as expected due to the increase in the scaled compressive pressure. The parameter π is calibrated in accordance with the experimental data provided in [14].

Due to the lack of creep data for EB-PVD coatings, experimental results provided for APS ceramic tested at 1050°C are used for the calibration of creep parameters q and A_3 [100]. The remaining creep parameters A_1 , A_2 and κ are taken from [94]. The numerical results showing creep strain for one element medium under different compressive loads are presented in Figure 4.7.

After identification of some material constants a brief parametric study investigating the effects of the mobility parameter \mathcal{M} and the phase field parameter β is conducted. The results are shown in Figure 4.8 and Figure 4.9. As expected, an increase in \mathcal{M} and a decrease in β accelerates the growth of TGO.

The contour plots showing the distribution of Cauchy stress components σ_{11} , σ_{22} , equivalent deviatoric stresses and the plastic strain are shown in the bond-coat and the top-coat in Figure 4.10 and Figure 4.11. During the phase transformation, large plastic strains due to high compressive stresses are generated in the multiphase region, which later transforms into a single oxide phase. Figure 4.12 shows the evolution of stress components σ_{11} and σ_{22} at a point in the vicinity of the interface in the TGO region. Figure 4.13 shows evolution of the same stress components in the vicinity of the interface in the top-coat region. The stress magnitudes generated in the oxide

region are in good agreement with the experimental results provided in [101] for a similar system, which reports a maximum of 800 MPa compressive stress (see Figure 4.12 and Figure 4.13). Figure 4.15 shows two stress distributions in the bond-coat for the purely elastic top-coat and plasticity-creep included top-coat material models. It can be seen from the figure that the maximum tensile and compressive stresses in the TGO and the bond-coat are significantly reduced.

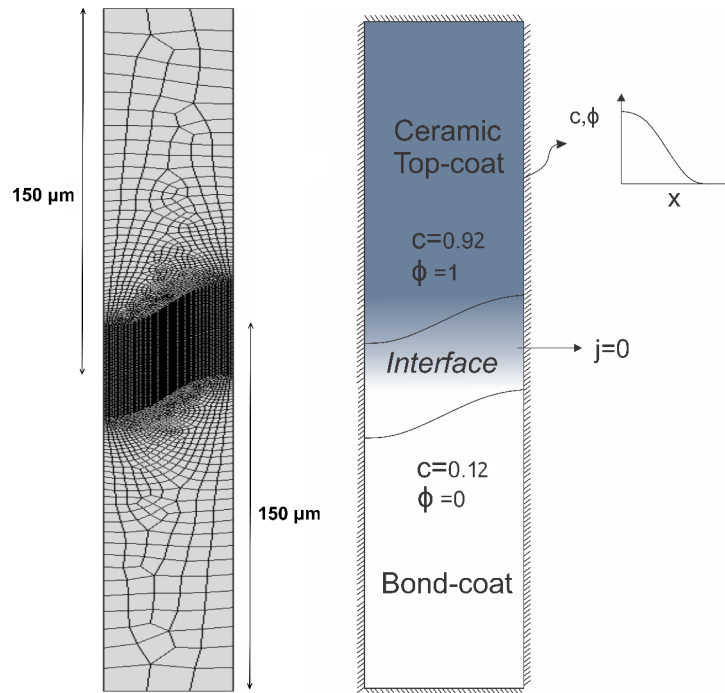


Figure 4.4: Initial conditions specified for the concentration and phase field variable.

Results for the model with creep is compared with no-creep condition for the top-coat in Figure 4.15. As it was expected the normal stress in lateral direction is considerably higher in the model with no creep due to absence of relaxation mechanism. In Figure 4.11 results related to stress and plastic strain in the bond-coat is demonstrated. Although the yield stress of the TGO is high, during phase transformation large plastic strain is generated in multiphase region, which later transforms to single oxide phase.

The contour results for the stresses presented in Figure 4.11 is incapable of showing the stress level in the TGO/bond-coat interface due to the small thickness of the interface and the result averaging in the region. The stress transition along the interphase region is shown in Figure 4.14, where a stress level as high as 3 GPa can be observed. These results are also confirmed by the experiments reporting a maximum of 2 – 4

GPa stresses in the TGO/bond-coat interface [102].

Table 4.1: Definition of variables

	Normalized concentration of species	\mathbf{C}^e	Right Cauchy-Green tensor
c		J	Jacobian
ϕ	Phase field variable	$\dot{\epsilon}^p$	Equivalent plastic strain rate
P	Auxiliary field variable	$\dot{\epsilon}_m^p$	Matrix equivalent plastic strain rate
ν	Absolute temperature	\mathbf{N}^p	Plastic flow direction
μ	Chemical potential	\mathbf{n}	Unit normal vector of the surface
ψ	Helmholtz free energy per unit reference volume	φ	Viscoplastic potential
η	Entropy per unit reference volume	\mathbf{T}	Cauchy stress
ε	Internal energy per unit reference volume	\mathbf{T}_R	1 st Piola-Kirchhoff stress
\mathbf{q}	Heat flux per unit reference area	\mathbf{T}^e	2 nd Piola-Kirchhoff stress
q	Heat flux with external source per unit reference volume	\mathbf{M}^e	Mandel stress
\mathbf{j}	Species flux per unit reference area	\mathbf{M}_0^e	Deviatoric Mandel stress
\mathcal{P}	Energy conjugate to ϕ (Scalar)	$\bar{\sigma}$	Equivalent stress
\mathcal{E}	Energy conjugate to $\nabla\phi$ (vector)	$\bar{\sigma}_m$	Matrix equivalent stress
\mathbf{F}	Deformation gradient	F	Amplifying function
\mathbf{E}^e	Elastic strain tensor	X	Triaxiality
\mathbf{v}	Velocity		
\mathbf{D}	Stretching tensor		
\mathbf{W}	Spin tensor		

Table 4.2: Material and analysis parameters

Parameters	Top-coat	Bond-coat	TGO	Unit
G	15.68×10^3	92.31×10^3	$154. \times 10^3$	MPa
K	19.27×10^3	200.00×10^3	$231. \times 10^3$	MPa
S_α	3.0×10^4	$5. \times 10^2$	$1. \times 10^4$	MPa
S_0	2.2×10^2	3.5×10^2	7.0×10^4	MPa
h	9.0×10^3	1.0×10^3	1.0×10^3	MPa
m	0.25	0.25	0.25	-
ε_0	0.5×10^{-10}	1×10^{-4}	1×10^{-4}	-
\mathcal{M}_{22}	2×10^{-17}	2×10^{-17}	2×10^{-17}	$\text{m}^5 \cdot \text{s} \cdot \text{mol} \cdot \text{J}^{-1}$
α_{22}	3.62×10^{-7}	3.62×10^{-7}	3.62×10^{-7}	$\text{J} \cdot \text{m}^{-1}$
β	0.95×10^6	0.95×10^6	0.95×10^6	$\text{J} \cdot \text{m}^{-3}$
χ	3.92×10^{-1}	3.92×10^{-1}	3.92×10^{-1}	-
k_1, k_2	6.0×10^3	6.0×10^3	6.0×10^3	$\text{J} \cdot \text{mol}^{-1} \cdot \text{m}^{-3}$
c_1	0.14	0.14	0.14	-
c_2	0.90	0.90	0.90	-
β_l	-	-	1.4×10^{-1}	-
β_t	-	-	1.6×10^{-3}	-
π	-	-	1×10^{-2}	-
q	1.3	-	-	-
A_1	1.0	-	-	-
A_2	20.3×10^5	-	-	-
A_3	1.3	-	-	-
κ	1.02	-	-	-

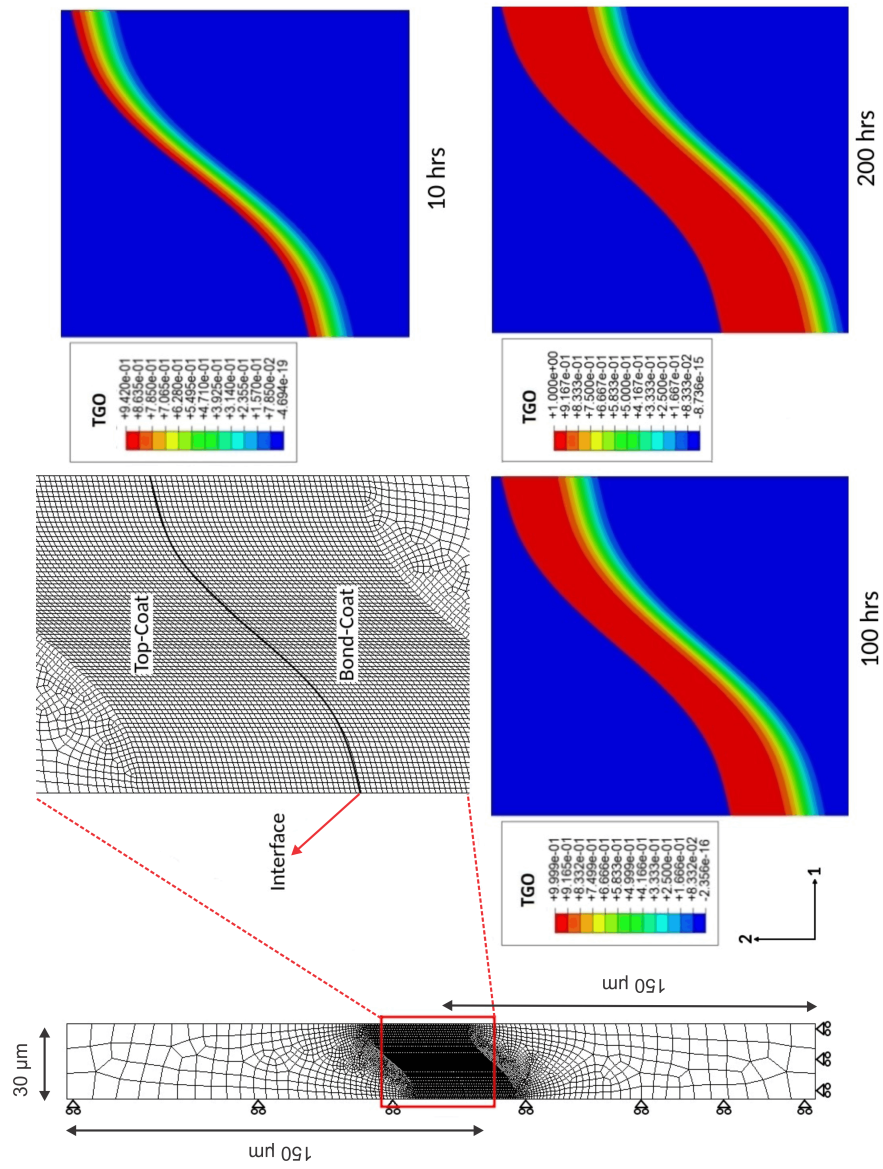


Figure 4.5: Mechanical boundary condition and TGO evolution in time after 10, 100 and 200 hrs.

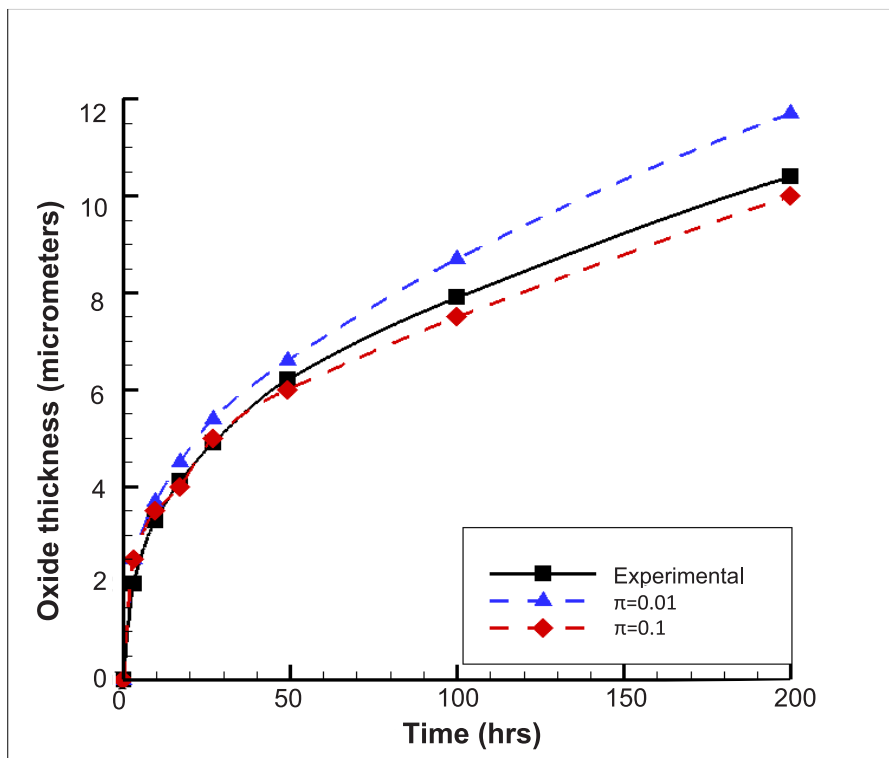


Figure 4.6: Calibration of parameter π of mechanical stresses on TGO growth. Experimental data is taken from [14].

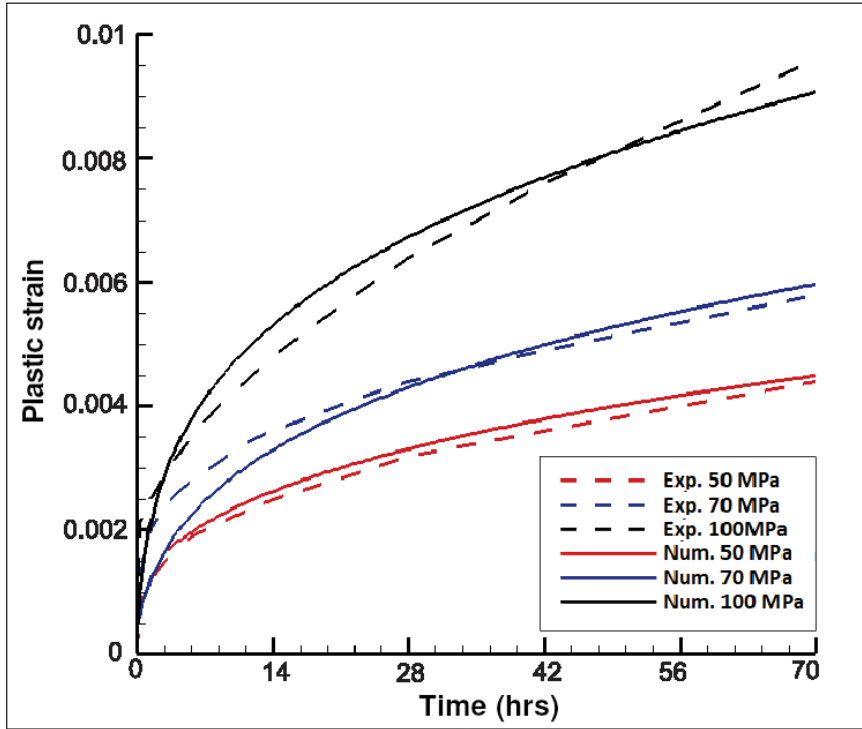


Figure 4.7: Validation of creep strain in 1050°C

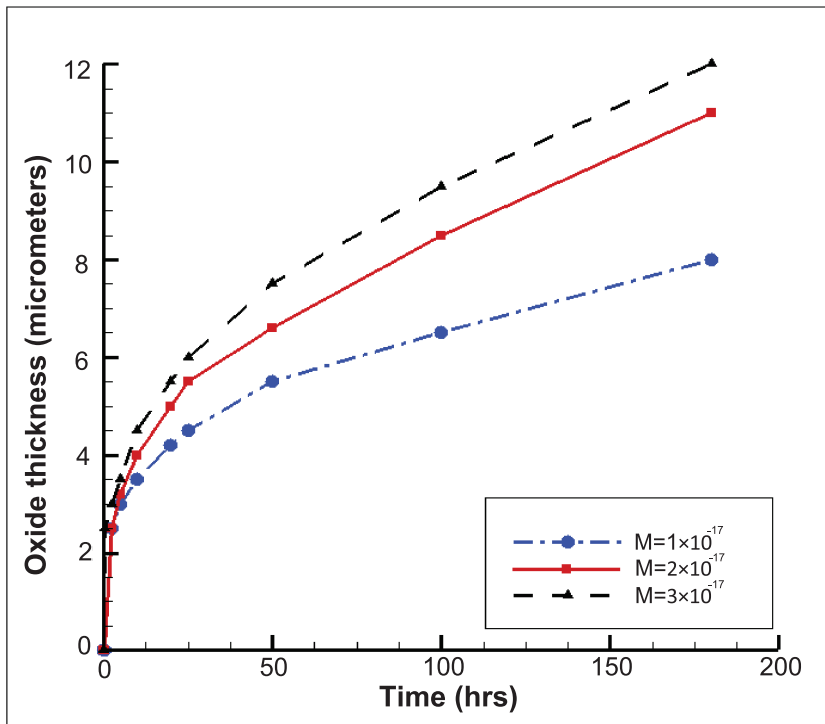


Figure 4.8: TGO thickness versus time for the increasing values of mobility parameter \mathcal{M} .

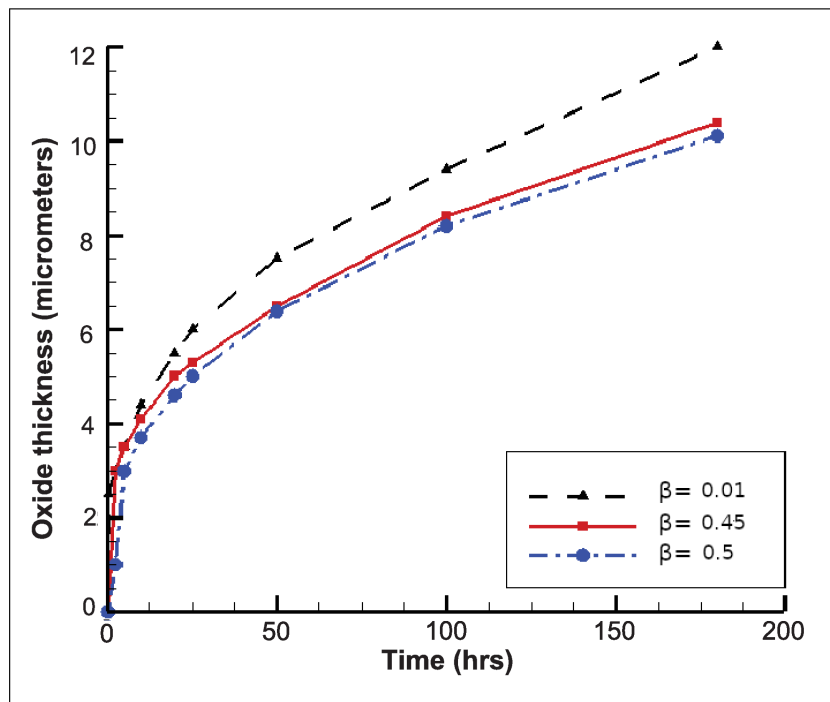


Figure 4.9: TGO thickness versus time for the increasing values of phase field parameter β .

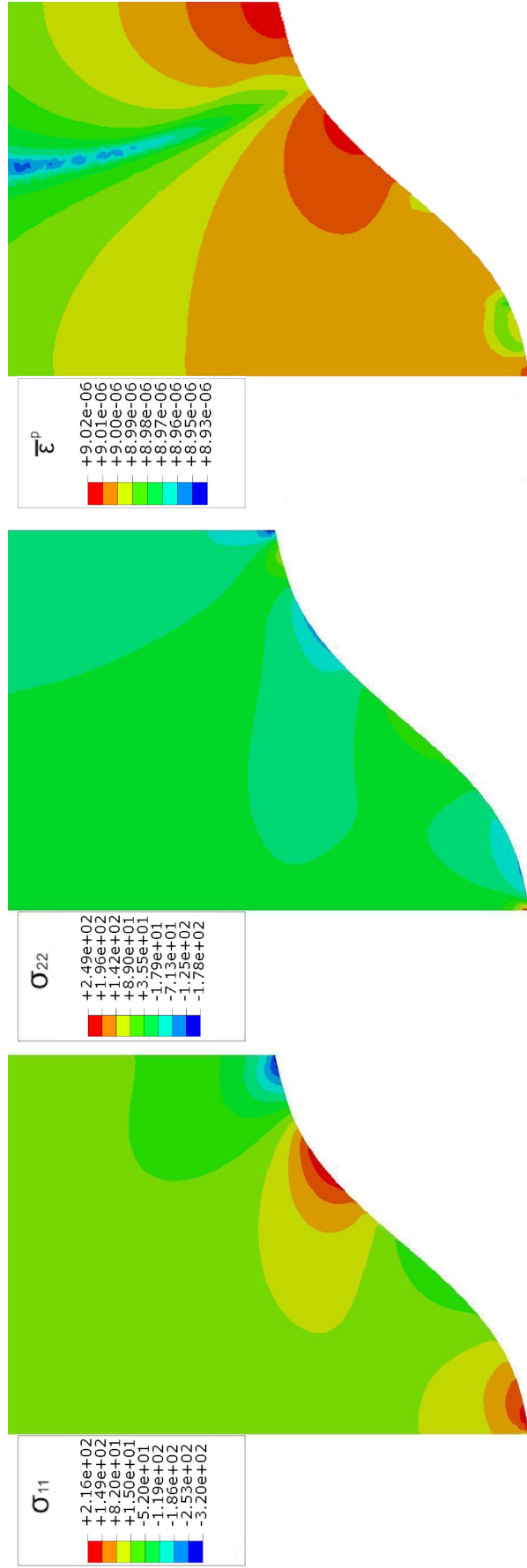


Figure 4.10: The normal Cauchy stress components (MPa) and equivalent plastic strain in the top-coat after 100 hrs of isothermal service.

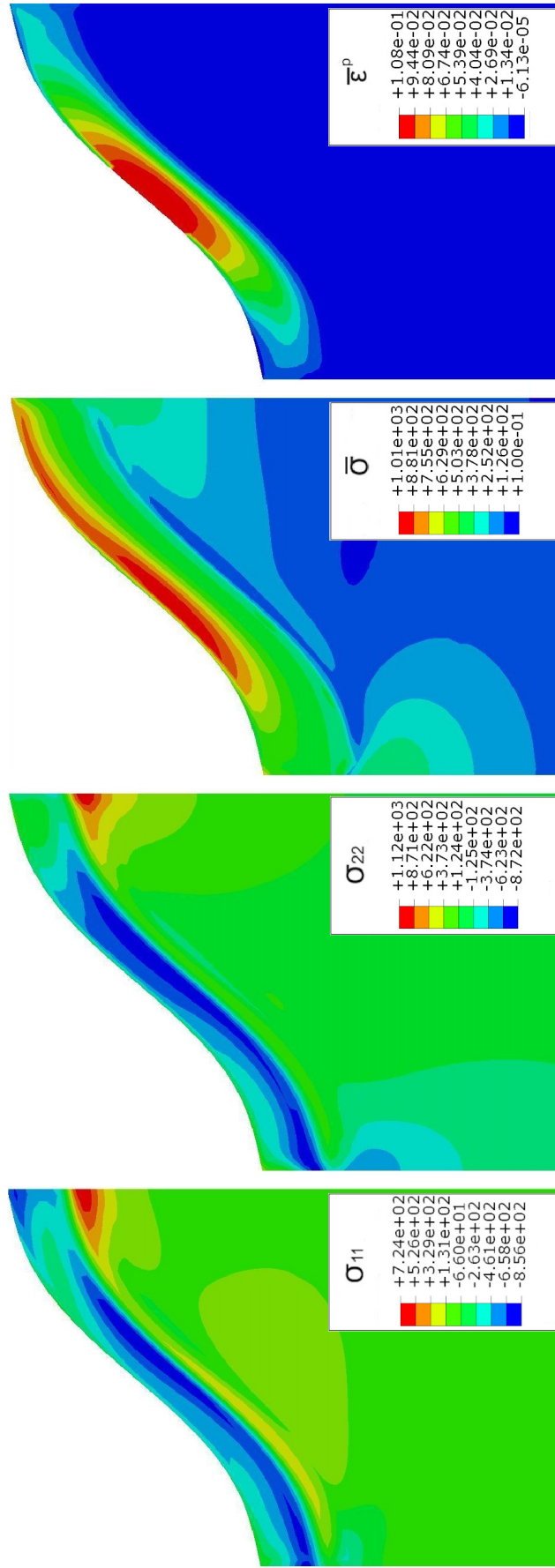


Figure 4.1.1: The normal Cauchy stress components (MPa) and equivalent plastic strain in the bond-coat after 100 hrs of isothermal service.

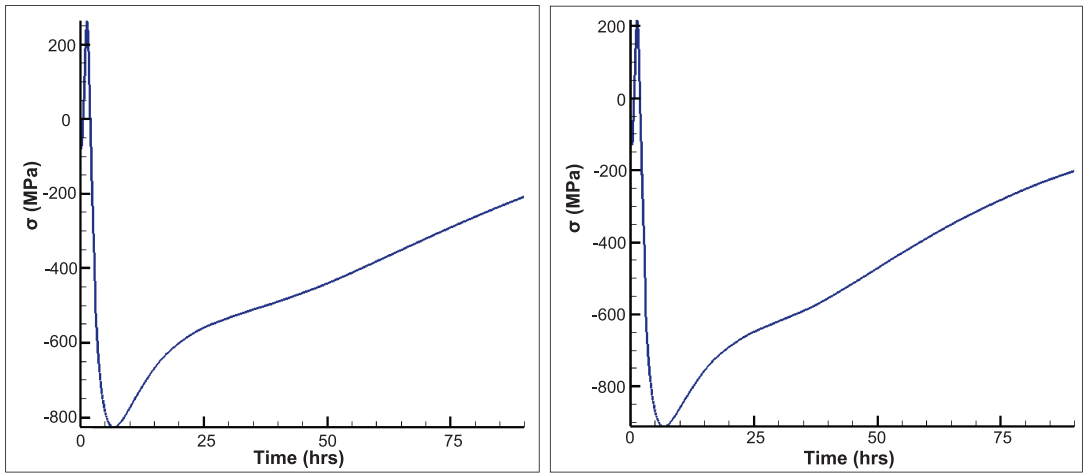


Figure 4.12: Evolution of stress component in TGO, in transverse σ_{11} (left) and lateral σ_{22} (right) directions.

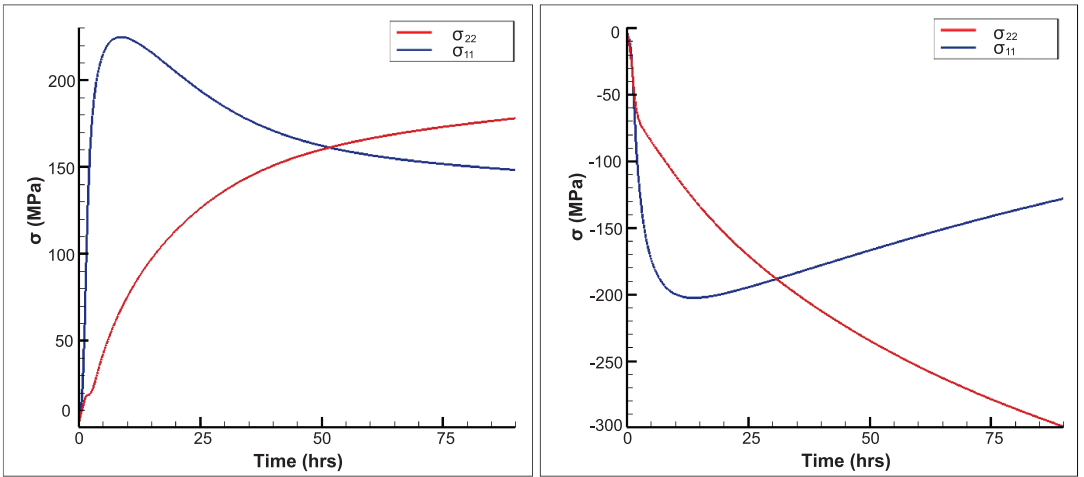


Figure 4.13: Evolution of lateral and transverse stresses in top-coat in downhill (left) and uphill of the interface (right).

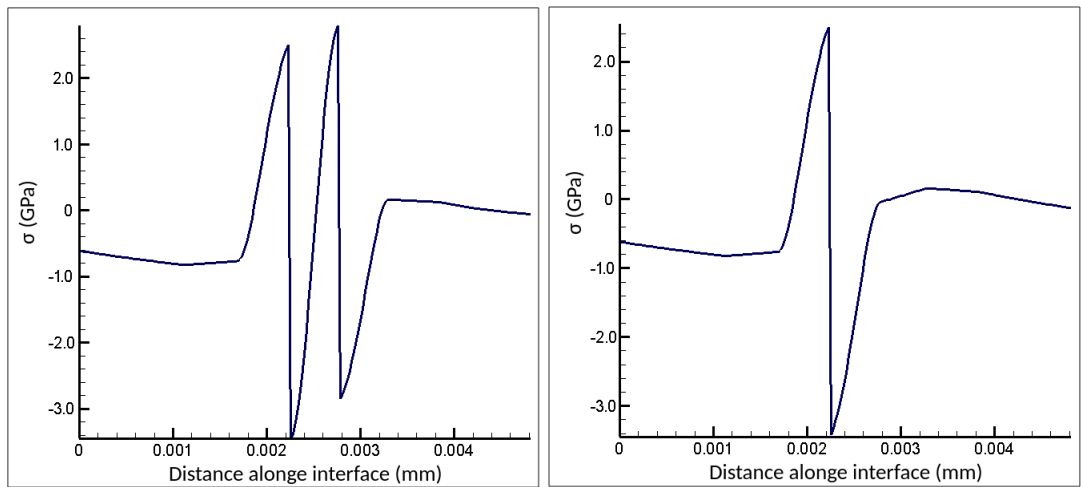


Figure 4.14: Evolution of stresses along the TGO/bond-coat interface, in transverse (left) and lateral (right) directions.

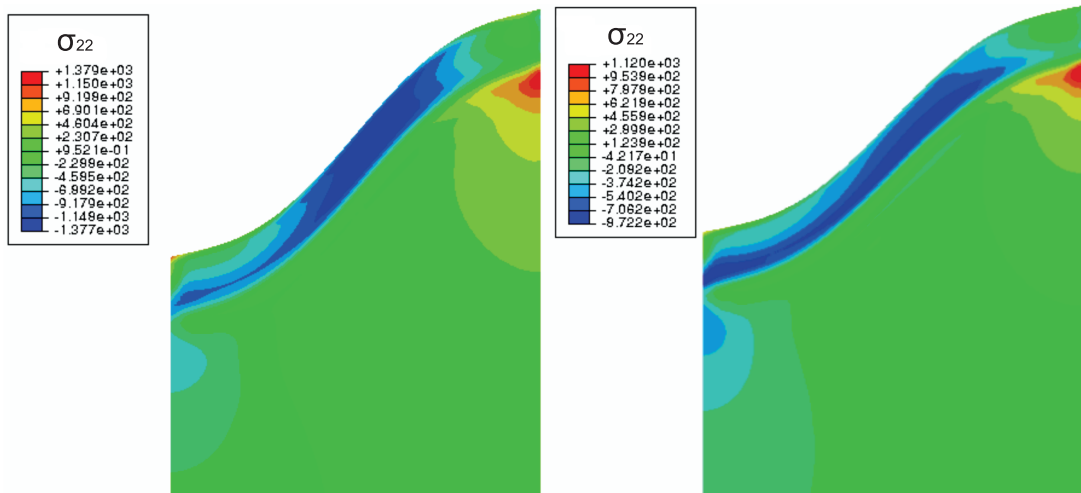


Figure 4.15: The normal Cauchy stress component (MPa) in the lateral direction in the bond-coat and the TGO without top-coat creep (elastic top-coat) (left) and with creep (right) after 100 hrs.

CHAPTER 5

FAILURE MODELING IN THERMAL BARRIER COATINGS

In the previous chapters a model capable of describing the oxidation process and oxidation induced elasto-viscoplastic deformation was introduced and implemented. Knowing the stress state in time, the simulation will be more valuable if the lifetime estimation mechanism of the TBC is also incorporated into the model. The following section is dedicated to the failure analysis of the system with an EB-PVD top-coat.

Lifetime estimation of the coating systems has always been a major challenge for the researchers, for the reason that these systems are utilized in technically critical and expensive elements. In the past two decades numerous experimental and numerical analyses have been conducted to understand and model the mechanisms playing role in the failure of those systems. In 1987 Chang et al. [27] numerically analyzed the thermo-mechanical behavior of a PS (Plasma sprayed) coating system using the finite element method. An elastic behavior for the materials was adopted and an initially existing crack for the failure was taken into account. In most of the cases the metal/ceramic interface is not a planer one [27]. To this end Evans et al. [103, 104] searched for the reason for the formation of initial crack leading to failure in undulated interfaces. Buckling and crack propagation were already known to be the reasons for the spallation of the ceramic coat [105], but searching for the mechanisms controlling the durability of the TBC, Evans et al. [24, 104] claimed that the initial crack is a result of cyclic plastic strain. Later, they [32] investigated the change in the material parameters and stresses induced by cycling loading by changing the number of cycles. They found that the TGO growth induces tensile stress in the TBC which is linearly dependent on the number of cycles. This dependency is related to the TGO/-topcoat interface undulation change because of the instabilities in the displacement

of the EB-PVD type ceramic topcoats. They also found the fracture parameters for a predefined crack in a TBC system and their relation with thermal cycling. Caliez et al. [106] used a damage failure model based on the critical thickness of the TGO for an isothermal test. The finite element method was used to find the evolution of stress in the system along with cohesive elements for the delaminating region to simulate the failure propagation. Aktaa et al. [107] simulated the TGO growth using the controlled movement of the nodes in a thermo-mechanical analysis. They also carried out a fracture analysis procedure for a crack at probable initiation site for the simulation of failure. Later, Bialas [108] used the swelling option of commercial software ABAQUS [109, 110] for simulation of the TGO growth and also took creep of the system materials into account to observe its effect on residual stresses and failure mechanism. There are also failure simulations based on cohesive element modeling, which are capable of predicting failure at the TC/TGO interface or the TGO/BC interface or any predefined failure surface [111, 108, 106, 109]. However, these models are incapable of predicting failure in the whole domain.

In this chapter of the study, a plasticity induced damage model is implemented using a model with a plastic material response for softening. The damage planes of the coating system are chosen in accordance with the experimental results published for the TBC failure in both the isothermal and cyclic loading. The presented model a simplistic approach toward modelling the initiation and progress of the failure over the entire simulated domain which should be further improved.

5.1 Kinematics

Defining \mathbf{F}^d to be the damage related part of the deformation gradient and using the Kröner's decomposition [112, 113] one can write,

$$\mathbf{F} = \mathbf{F}^e \mathbf{F}^d \quad (5.1)$$

$$\dot{\mathbf{F}}^d = \mathbf{L}^d \mathbf{F}^d \quad (5.2)$$

where \mathbf{F}^e is the elastic distortion which represents the stretch and rotation and \mathbf{F}^d is the damage distortion. Then the velocity gradient is decomposed in the following form.

$$\mathbf{L} = \mathbf{L}^e + \mathbf{F}^e \mathbf{L}^d \mathbf{F}^{e-1} \quad (5.3)$$

where,

$$\mathbf{L}^e = \dot{\mathbf{F}}^e \mathbf{F}^{e-1}, \quad \mathbf{L}^d = \dot{\mathbf{F}}^d \mathbf{F}^{d-1} \quad (5.4)$$

The right polar decomposition of \mathbf{F}^e yields,

$$\mathbf{F}^e = \mathbf{R}^e \mathbf{U}^e \quad (5.5)$$

The Hencky's strain,

$$\mathbf{E}^e = \ln(\mathbf{U}^e) \quad (5.6)$$

is chosen as the strain measure. Following the decomposition given in equation (5.1), the Jacobian can also be decomposed as,

$$J = J^e J^d, \quad J^e = \det \mathbf{F}^e > 0, \quad J^d = \det \mathbf{F}^d > 0. \quad (5.7)$$

The elastic and damage related stretching and spin tensors are,

$$\mathbf{D}^e = \text{sym} \mathbf{L}^e, \quad \mathbf{D}^d = \text{sym} \mathbf{L}^d \quad (5.8)$$

$$\mathbf{W}^e = \text{skew} \mathbf{L}^e, \quad \mathbf{W}^d = \text{skew} \mathbf{L}^d \quad (5.9)$$

An irrotational damage flow is assumed, i.e.,

$$\mathbf{W}^d = 0 \quad (5.10)$$

The damage stretching is defined as

$$\mathbf{D}^d = \dot{\varepsilon}^d \mathbf{N}^d \quad (5.11)$$

where $\dot{\varepsilon}^d$ is the equivalent damage strain rate and,

$$\mathbf{N}^d = \mathbf{n} \quad (5.12)$$

In this model for simulation of the delamination of the TBC layers and crack initiation and propagation in the top-coat only mode I fracture is assumed. Thus, \mathbf{n} is a predefined unit vector normal to the damage plane (normal to the opening face). The trial Mandel stress is defined as

$$\mathbf{M}^e = \mathbb{C} : \mathbf{E}^e \quad (5.13)$$

The Mandel stress is projected on the normal of the damage plane. The magnitude of the projected vector is calculated as follows

$$M_d^e = |\mathbf{n} \cdot \mathbf{M}^e \mathbf{n}| \quad (5.14)$$

The Cauchy stress is defined as,

$$\mathbf{T} = J^{-1} \mathbf{R}^e \mathbf{M}^e \mathbf{R}^{eT} \quad (5.15)$$

The microforce balance reads,

$$M_d^e = g(\dot{\varepsilon}^d, S^d) \quad \text{when} \quad \dot{\varepsilon}^d > 0 \quad (5.16)$$

The parameter S^d is known as the material or deformation saturation resistance. g is a specific softening function defined in the next section.

5.1.1 Time integration

A summary of the time integration procedure for the model is presented below. Terms with $*$ are trial values. For a displacement driven analysis, the deformation gradient is known, so the trial elastic deformation gradient using the Kröner's decomposition can be calculated.

$$\mathbf{F}_{n+1}^{e*} = \mathbf{F}_{n+1} (\mathbf{F}^d)^{-1} \quad (5.17)$$

The polar decomposition is applied to the elastic deformation gradient and \mathbf{E}^{e*} is found to be

$$\mathbf{E}^{e*} = \ln(\mathbf{U}_{n+1}^{e*}) \quad (5.18)$$

The trial Mandel stress is calculated as,

$$\mathbf{M}^{e*} = \mathbb{C} : \mathbf{E}^{e*} \quad (5.19)$$

Then, the projection of the trial Mandel stress reads,

$$M_d^{e*} = |\mathbf{n} \cdot \mathbf{M}^{e*} \mathbf{n}| \quad (5.20)$$

The damage resistance (S^d) function is assumed to obey the following evolution with initial value S_0^d .

$$\dot{S}^d(\dot{\tilde{\epsilon}}^d, \dot{\tilde{\epsilon}}^p) = h \dot{\tilde{\epsilon}}^p + h_1 \dot{\tilde{\epsilon}}^d + S^d \left(\frac{\dot{\tilde{\epsilon}}^d}{\dot{\tilde{\epsilon}}_0^d} \right)^{m^d} \quad (5.21)$$

where h , h_1 , m^d and $\dot{\tilde{\epsilon}}_0^d$ are the hardening, softening, rate sensitivity and the reference damage flow rate parameters, respectively. h_1 is chosen to be a negative value so that

softening will occur instead of normal hardening. The definition of a rate-dependent behavior for plasticity provides a smooth transition from plasticity to the damage, which can be observed in the stress-strain curve plotted for a one-dimensional analysis in Figure 5.1. Including the plastic strain in the damage resistance function will provide dependency of the damage initiation stress on plastic deformation. As plasticity occurs in the material, damage occurrence would be easier through the oxidation process. Similarly as expressed in Appendix A the corrected Mandel stress can be written as

$$\mathbf{M}^e = \mathbf{M}^{e*} - \mathbb{C} : (\Delta t \mathbf{D}_{n+1}^d) \quad (5.22)$$

where,

$$\mathbf{D}_{n+1}^d = \dot{\tilde{\varepsilon}}^d \mathbf{N}^d \quad (5.23)$$

Substituting the expression for stretching tensor \mathbf{D}^d one can get,

$$\mathbf{M}^e = \mathbf{M}^{e*} - \Delta t \dot{\tilde{\varepsilon}}^d \mathbb{C} : \mathbf{N}^d \quad (5.24)$$

Since \mathbb{C} and \mathbf{N}^d are constant tensors the following tensor can be replaced with the multiplication those tensors.

$$\mathbf{C}_n = \mathbb{C} : \mathbf{N}^d \quad (5.25)$$

Equation (5.24) can be rewritten as

$$\mathbf{M}^e = \mathbf{M}^{e*} - \Delta t \dot{\tilde{\varepsilon}}^d \mathbf{C}_n \quad (5.26)$$

Calculating the magnitude of the projection of both sides of the equation (5.26) on \mathbf{n}

$$\mathbf{n} \cdot \mathbf{M}^e \mathbf{n} = \mathbf{n} \cdot \mathbf{M}^{e*} \mathbf{n} - \Delta t \dot{\tilde{\varepsilon}}^d (\mathbf{n} \cdot \mathbf{C}_n \mathbf{n}) \quad (5.27)$$

$\mathbf{n} \cdot \mathbf{C}_n \mathbf{n}$ represents an elastic modulus in the direction of the damage plane and can be represented as C_d . Using equation (5.20) the equation can be rewritten as,

$$M_d^e = M_d^{e*} - \Delta t \dot{\varepsilon}^d C_d \quad (5.28)$$

Then the following equations have to be solved for $\dot{\varepsilon}^d$ [114].

$$M_d^e - M_d^{e*} + \Delta t \dot{\varepsilon}^d C_d = 0 \quad (5.29)$$

$$S_{n+1}^d - S_n^d - \Delta t [h \dot{\varepsilon}^p + h_1 \dot{\varepsilon}^d + S^d \left(\frac{\dot{\varepsilon}^d}{\dot{\varepsilon}_0^d} \right)^{m^d}] = 0 \quad (5.30)$$

As a consequence of the microforce balance and using equation (5.21) and (5.29), (5.30) and assuming that $\dot{\varepsilon}^p = 0$ when $\dot{\varepsilon}^d > 0$, one can write

$$S_n^d + \Delta t h_1 \dot{\varepsilon}^d - M_d^{e*} + \Delta t \dot{\varepsilon}^d C_d + \Delta t S^d \left(\frac{\dot{\varepsilon}^d}{\dot{\varepsilon}_0^d} \right)^{m^d} = 0 \quad (5.31)$$

Thus, only equation (5.31) has to be solved for $\dot{\varepsilon}^d$. Having found the equivalent plastic strain rate, the updated stresses can be found using the following equations. The exponential mapping for the solution of equation (5.17) is used.

$$\mathbf{F}_{n+1}^d = \exp(\Delta t \mathbf{D}_{n+1}^d) \mathbf{F}_n^{d-1} \quad (5.32)$$

$$\mathbf{F}_{n+1}^e = \exp(-\Delta t \mathbf{D}_{n+1}^d) \mathbf{F}_{n+1}^{d-1} \quad (5.33)$$

Then, the Piola stress and the Mandel stress are computed.

$$\mathbf{T}_{n+1}^e = \mathbb{C} : \mathbf{E}_{n+1}^e \quad (5.34)$$

$$\mathbf{M}_{n+1}^e = \mathbf{F}_{n+1}^{eT} \mathbf{F}_{n+1}^e \mathbf{T}_{n+1}^e \quad (5.35)$$

Finally, the Cauchy stress reads

$$\mathbf{T}_{n+1} = J^{-1} \mathbf{R}_{n+1}^e \mathbf{M}_{n+1}^e \mathbf{R}_{n+1}^{eT} \quad (5.36)$$

5.2 Analysis

A plane-strain one-element analysis is initially carried out for a uniaxial tension test. The material parameters used are presented in Table 5.1. The stress-strain curve with hardening and a sharp softening region is observable in Figure 5.1. The initial failure strength of the model was defined to be $S_0^d = 400\text{MPa}$, but as it can be seen in the stress-strain plot, the softening mechanism initiates at approximately 290MPa, confirming the plasticity induced early failure.

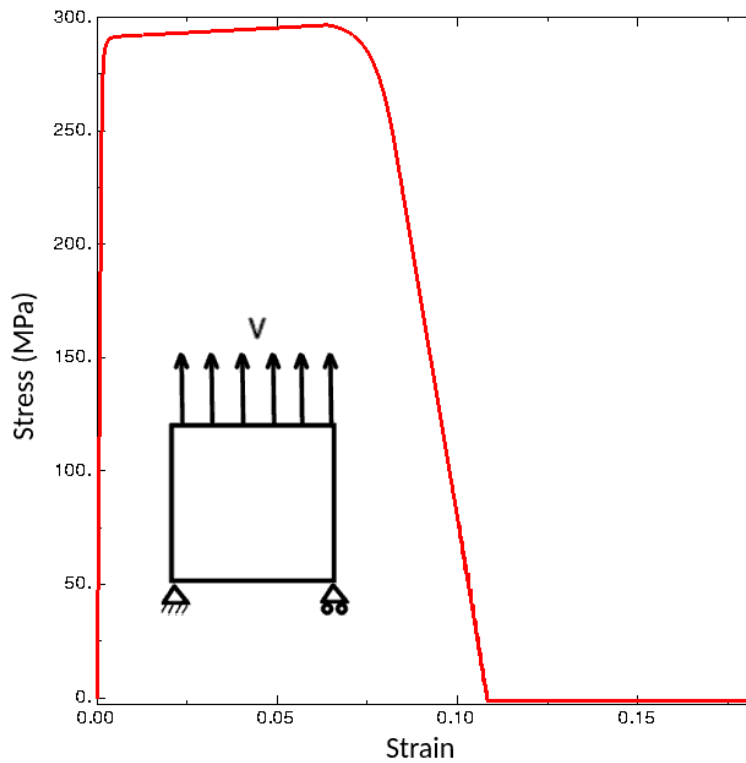


Figure 5.1: Stress-strain curve for one element simple tension test.

The next analysis is carried out for a strip under uniaxial tensile load, where the loading is applied at a constant strain rate, see Figure 5.2. A defected element is defined in the middle of the strip with lower deformation resistance ($S_0^d = 6.48\text{MPa}$).

Table 5.1: Material and analysis parameters

Parameters	Value	Unit	Parameters	Value	Unit
G	$150. \times 10^3$	MPa	$\dot{\varepsilon}_0$	1.0×10^{-4}	-
K	$225. \times 10^3$	MPa	S_0^d	4.0×10^2	MPa
S_0	2.5×10^2	MPa	h_1	-4.0×10^3	MPa
h	2.0×10^3	MPa	m^d	0.2	-
m	0.4	-	$\dot{\varepsilon}_0^d$	1.0×10^{-4}	-

The material properties for the analysis can be found in Table 5.2. The damage and stress contours are presented in Figure 5.2. Furthermore, the axial stress-strain curves in the defected element and in a regular element are depicted in Figure 5.2 as well. The elastic relaxation in the regular element is due to the damage progress in the defected element.

The model is also used in a uniaxial tension test with a weakened element to check its capability to model crack propagation. Propagation of the crack and the stress-strain curve for the damaged element are shown in Figure 5.3.

Table 5.2: Material and analysis parameters

Parameters	Value	Unit	Parameters	Value	Unit
G	$150. \times 10^3$	MPa	$\dot{\varepsilon}_0$	1.0×10^{-4}	-
K	$225. \times 10^3$	MPa	S_0^d	6.5×10^2	MPa
S_0	3.5×10^2	MPa	h_1	-4.0×10^3	MPa
h	2.0×10^3	MPa	m^d	0.2	-
m	0.4	-	$\dot{\varepsilon}_0^d$	1.0×10^{-4}	-

Transverse cracks are reported to be appearing usually at the material interfaces and in the TGO. In the case of EB-PVD top-coats lateral (normal to the TC/TGO interface in the direction of ceramic columns) cracks are responsible for the final spallation of the coatings in addition to the transversal (laying parallel the TC/TGO interface) cracks which may be also present in the structure. The transversely propagated cracks join the lateral ceramic cracks and this leads to the delamination and spallation of the

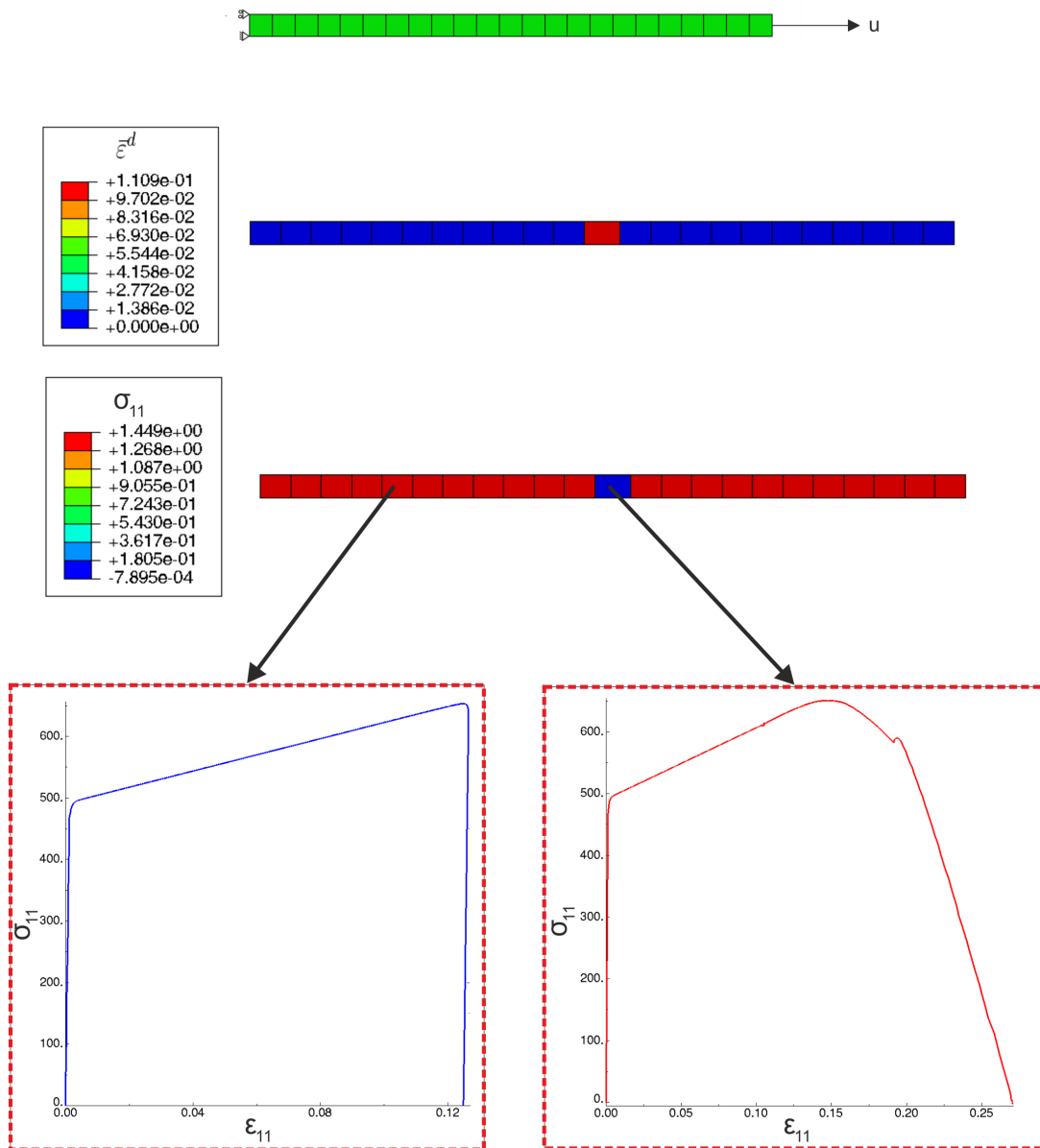


Figure 5.2: Uniaxial tensile loading of a strip with a defected element.

ceramic topcoat [115, 116, 6](Figure 5.4). In the case of isothermal analysis (Figure 5.5), the major transversal crack seems to be initiated from the downhill of the interface undulation (red arrow) and lateral cracks are observable mainly at the turning points of the interface profile (yellow arrows). It can be also observed that the location of the failure site depends on the shape of the undulation. Figure 5.6 shows damage in the same specimen after 200hrs of isothermal service. Finally, in this chapter an analysis is carried out by coupling the model presented in the previous chapter with the damage model for a TBC specimen with an undulated interface similar to the to-

pography of the failed region in the SEM image marked in Figure 5.6. The normal vector of the damage plane for the top-coat is defined to be on the x axis and for the bond-coat, this vector lays on the y axis.

The damage resistance of the top-coat, the bond-coat, and the TGO are calibrated with the experimental results so that the crack initiation will neither start too early nor too late in the domain. According to the SEM images damage is observed not earlier than 96hrs of isothermal service [15]. The crack initiation region in the medium depends strongly on the defects already present in the as-deposited coating system. However, for this analysis a homogeneous low damage resistance top-coat is assumed instead.

Table 5.3: Damage parameters

Parameters	Top-coat	Bond-coat	TGO	Unit
S_0^d	1.55×10^2	8.2×10^2	8.2×10^2	MPa
h_1	-1×10^3	-1×10^3	-1×10^3	MPa
m^d	0.2	0.2	0.2	-
$\dot{\epsilon}_0^d$	1×10^{-4}	1×10^{-4}	1×10^{-4}	-

The analysis conducted in the previous chapter for the oxidation of the TBC system at 1200°C is repeated with the same geometry and boundary conditions. However, damage model takes the control of the kinematics this time after the damage threshold is reached (see Figure A.1). The parameters in the Table 4.2 are used for this analysis and additional parameters used in the damage model is as presented in Table 5.3. Figure 5.7 shows the damage evolution in the domain after 200hrs of service. A comparison of the result with the experimental result in Figure 5.6 reveals the similarity in the initiation point and extent of the damage in these two results. As it was expected damage is initiated at the turning point of the profile mainly in the top-coat/TGO interface. Another site for the damage is the TGO/bond-coat interface where the material mismatch is responsible for the high stresses. Figure 5.8 shows that the maximum projected stress is moving with the oxidation front.

The normal stresses, equivalent plastic strain, and the damage resistance contour which is evolving due to plasticity and damage are shown for the TC and the BC/TGO in Figure 5.9 and Figure 5.10. It can be seen that the damage resistance is lower in

the regions with high plastic strain. The stress relaxation due to the damage in the top-coat can be observed but since there is not considerable damage in the TGO the relaxation can not be detected in the presented contour. It should be also noted that evolution of S^d is dependent on the hardening parameter before damage is initiated. Since hardening parameter is lower in the TGO, the decrease in the damage resistance is lower in this region in comparison with the top-coat.

A parametric study is also conducted for the initial damage resistance S_0^d in the top-coat and the TGO and the results are presented in Figure 5.11 and Figure 5.12. The results show that change in the resistance only changes the extent of the damage, but the initiation point does not change both for the top-coat and the bond-coat.

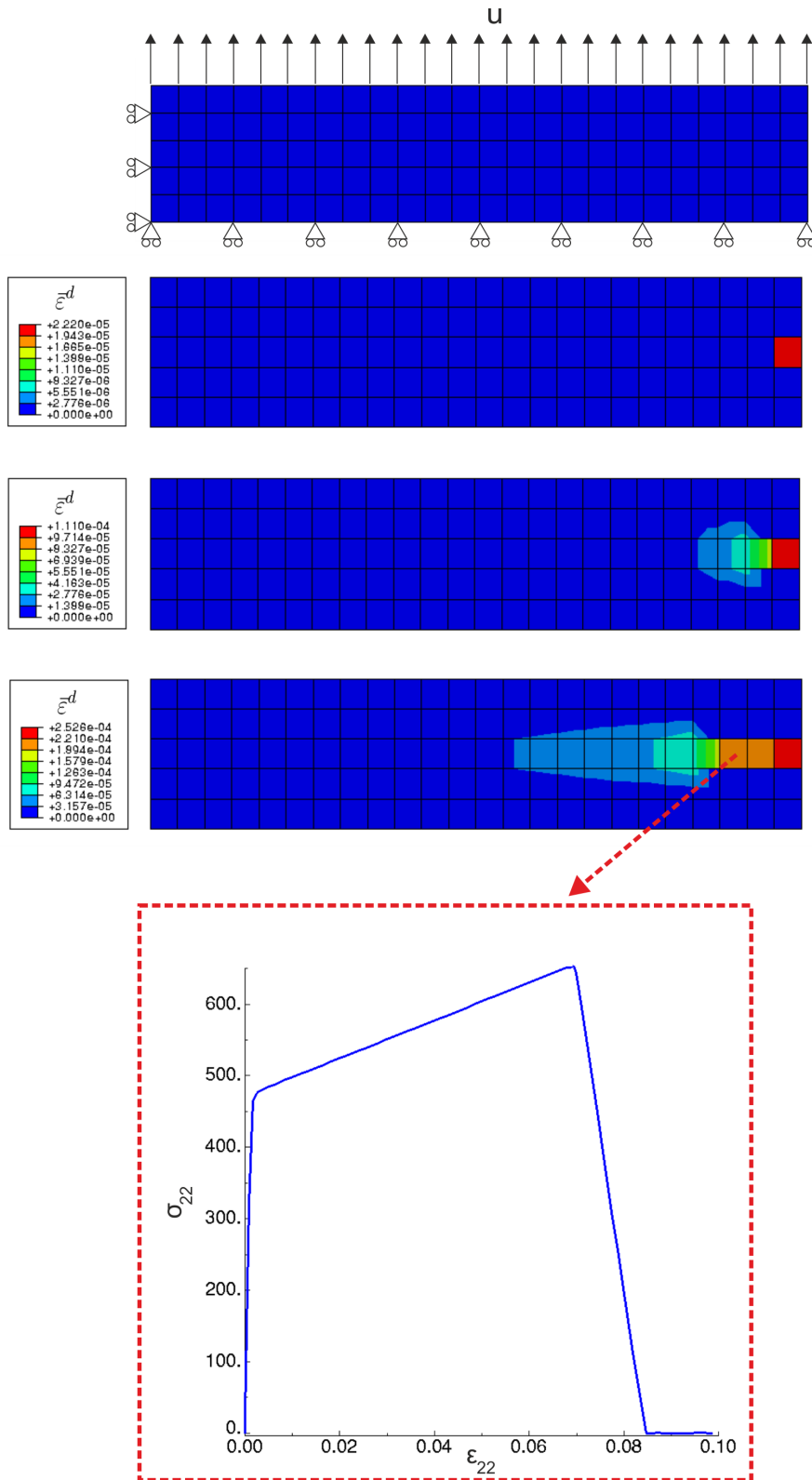


Figure 5.3: Damage evolution and crack propagation in a mode I fracture test.

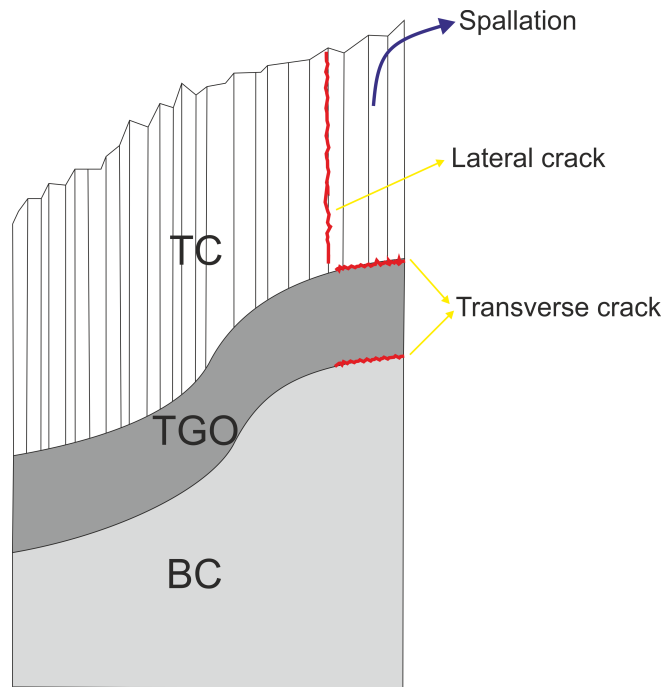


Figure 5.4: lateral and transverse cracks in the system and spallation of the top-coat due to coalescence of the cracks.

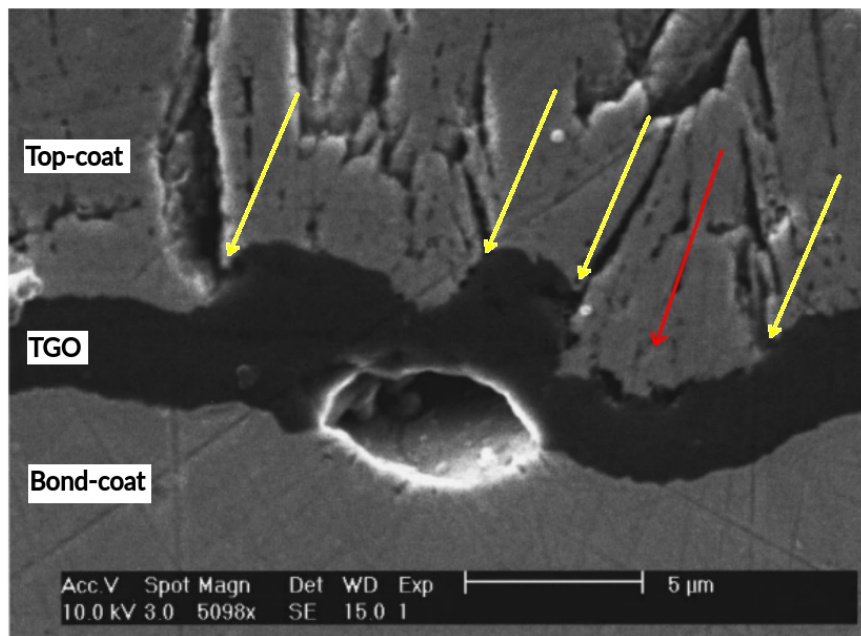


Figure 5.5: Cracks in the top-coat (yellow) and in the TGO (red) in an isothermally tested specimen after 96 hrs [15].

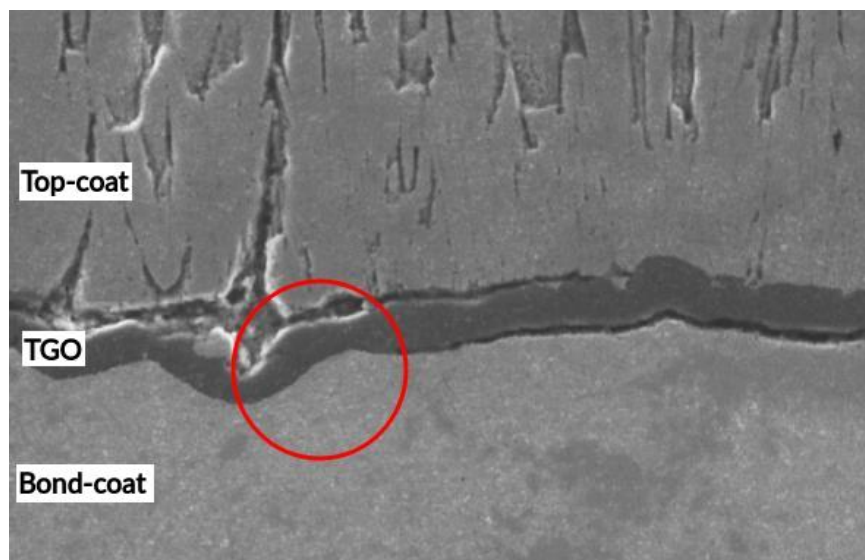


Figure 5.6: Cracks in an isothermally tested specimen after 200 hrs [15].

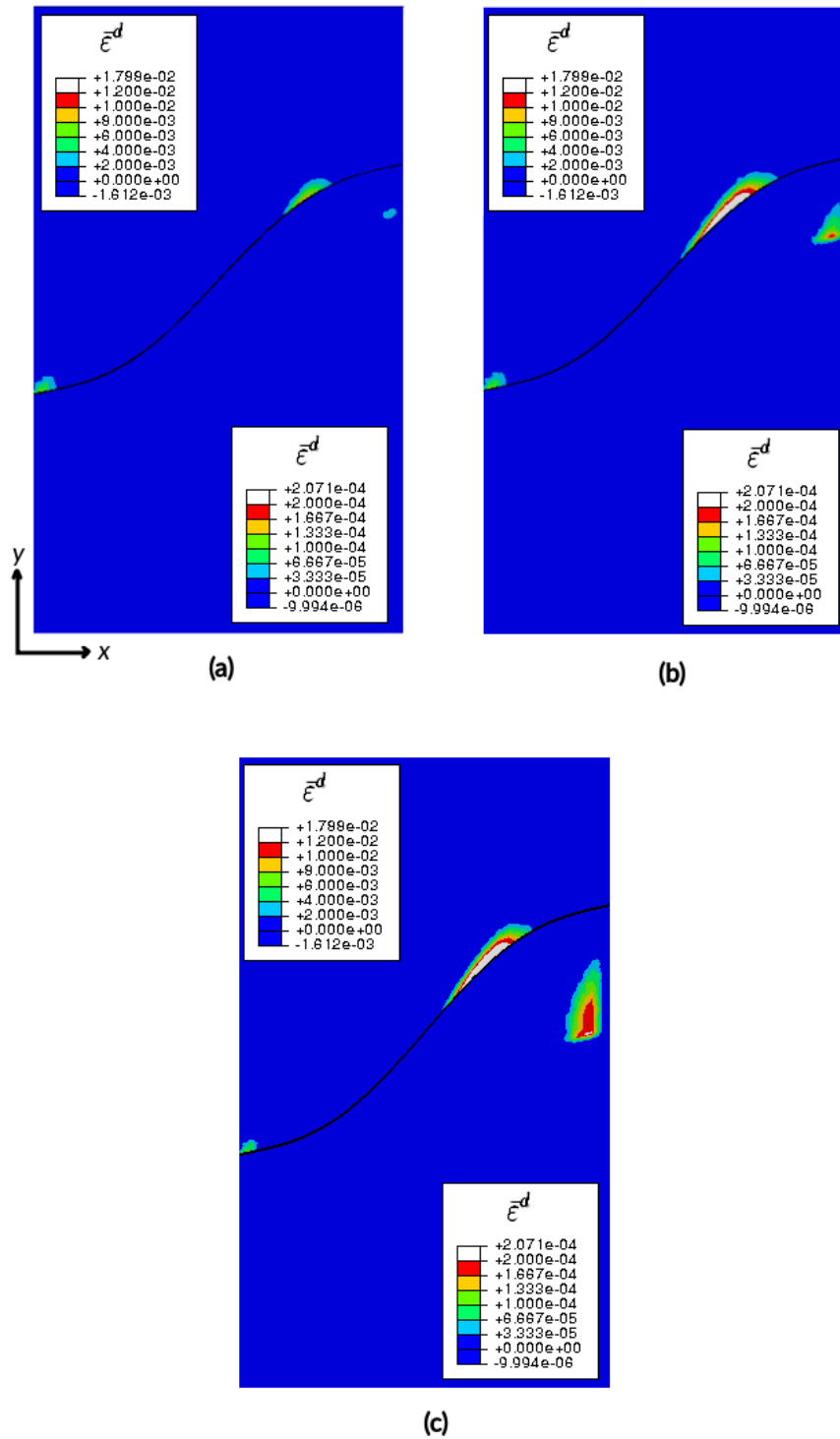


Figure 5.7: Damage contour for isothermal analysis after (a) 10 hrs, (b) 100 hrs and (c) 200 hrs.

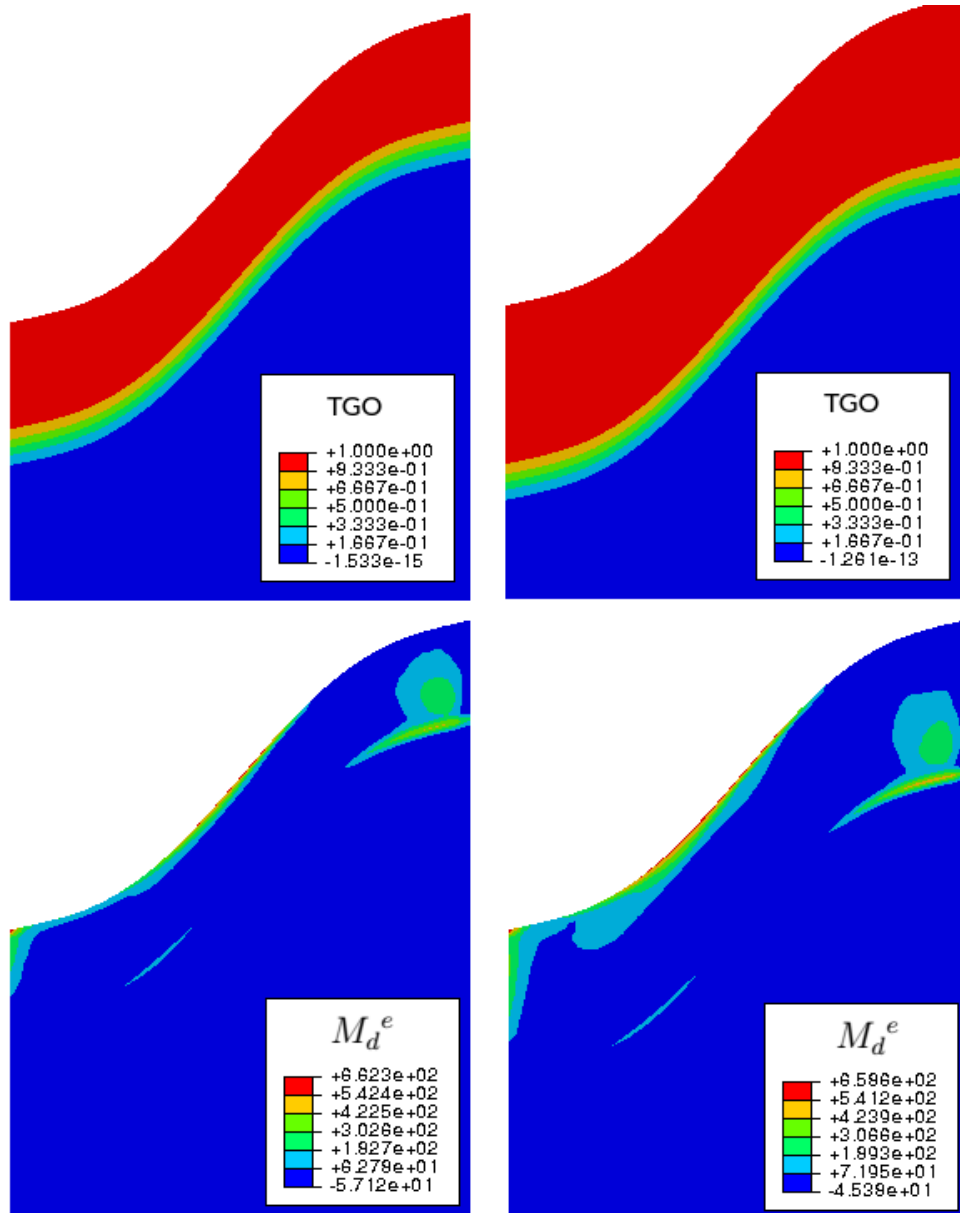


Figure 5.8: The TGO vs. the projected stress in the TGO after 100 hrs (left) and 200 hrs (right).

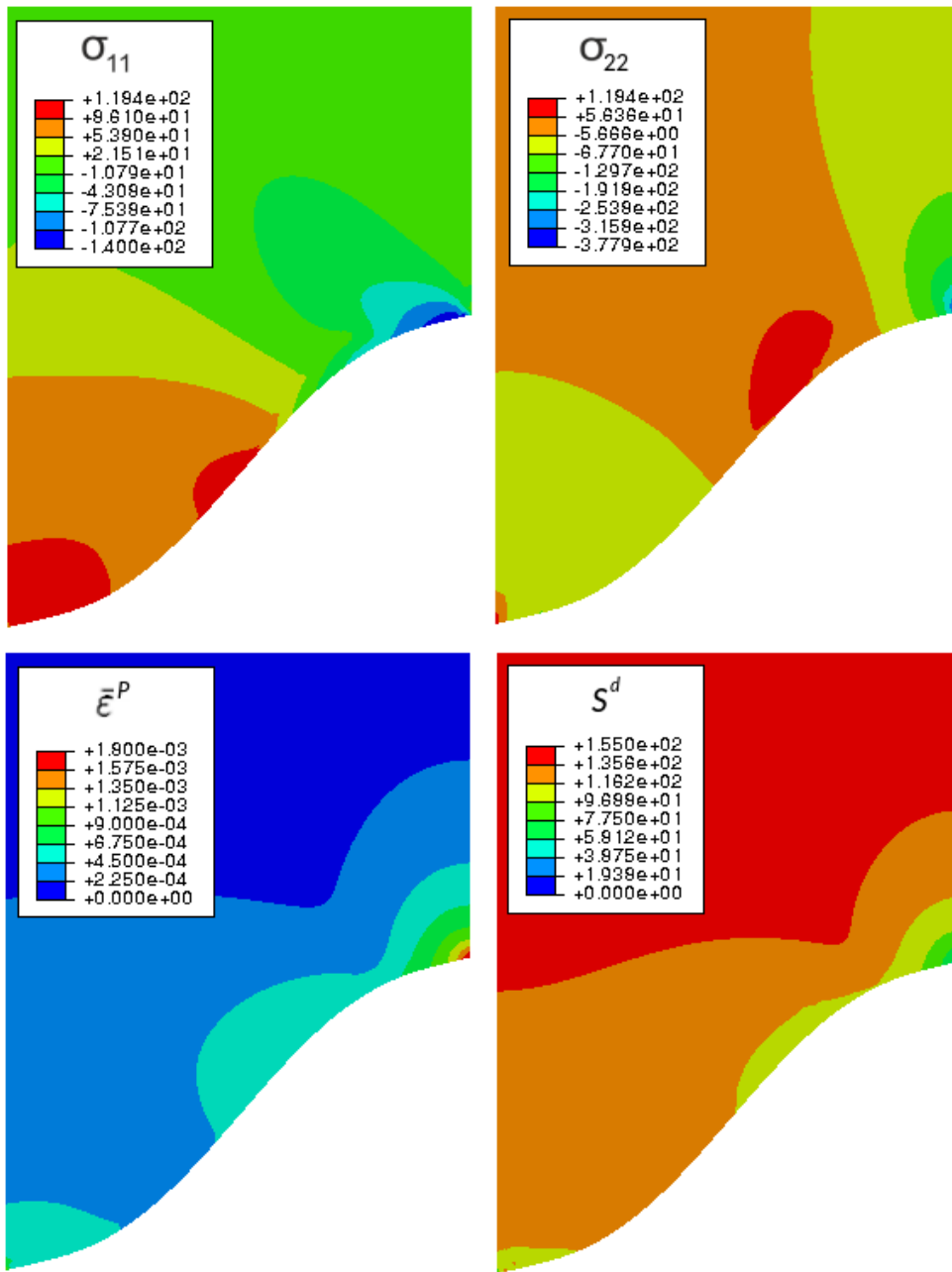


Figure 5.9: The normal Cauchy stress components (MPa), equivalent plastic strain, and damage resistance (MPa) in the top-coat after 200 hrs of isothermal service.

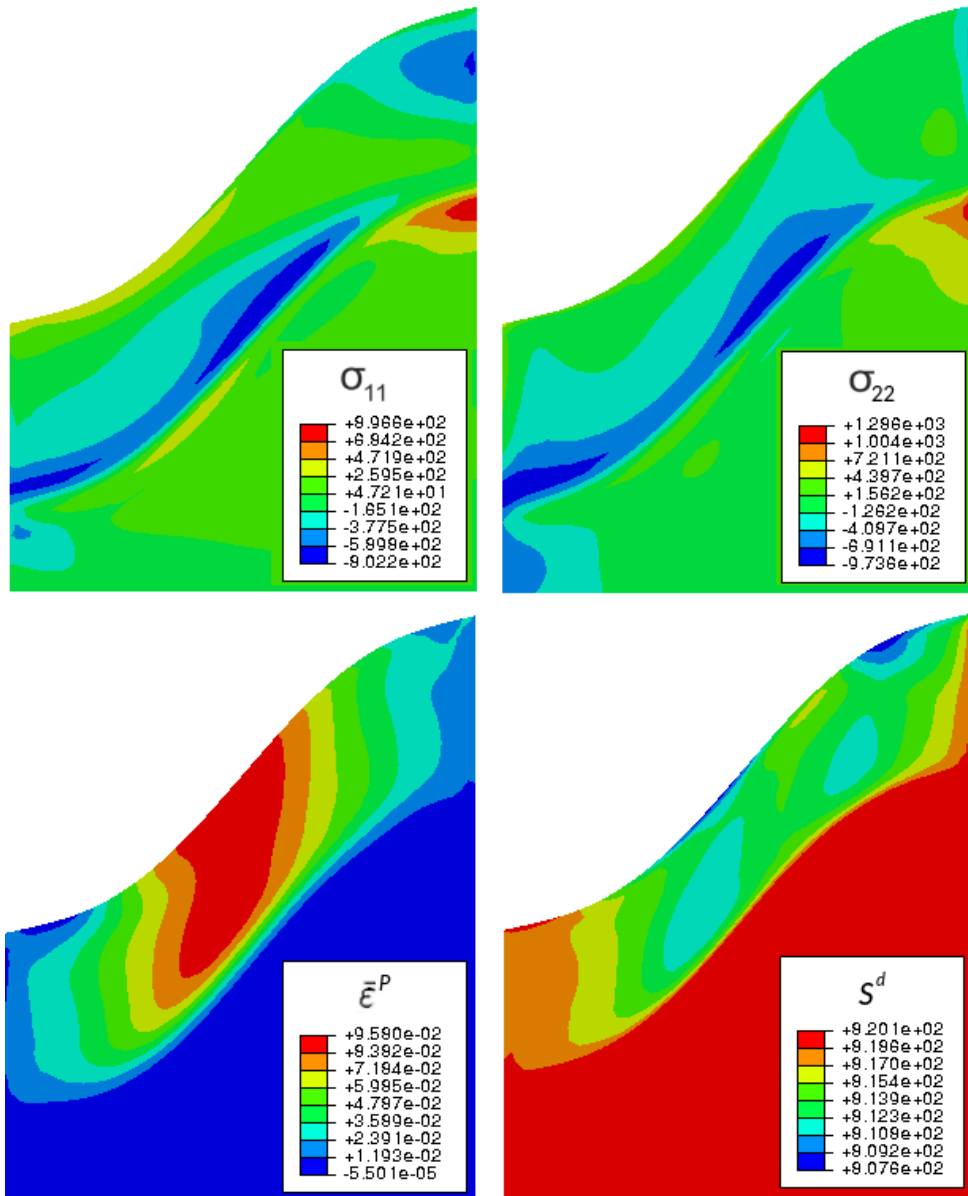


Figure 5.10: The normal Cauchy stress components (MPa), equivalent plastic strain, and damage resistance (MPa) in the bond-coat after 200 hrs of isothermal service.

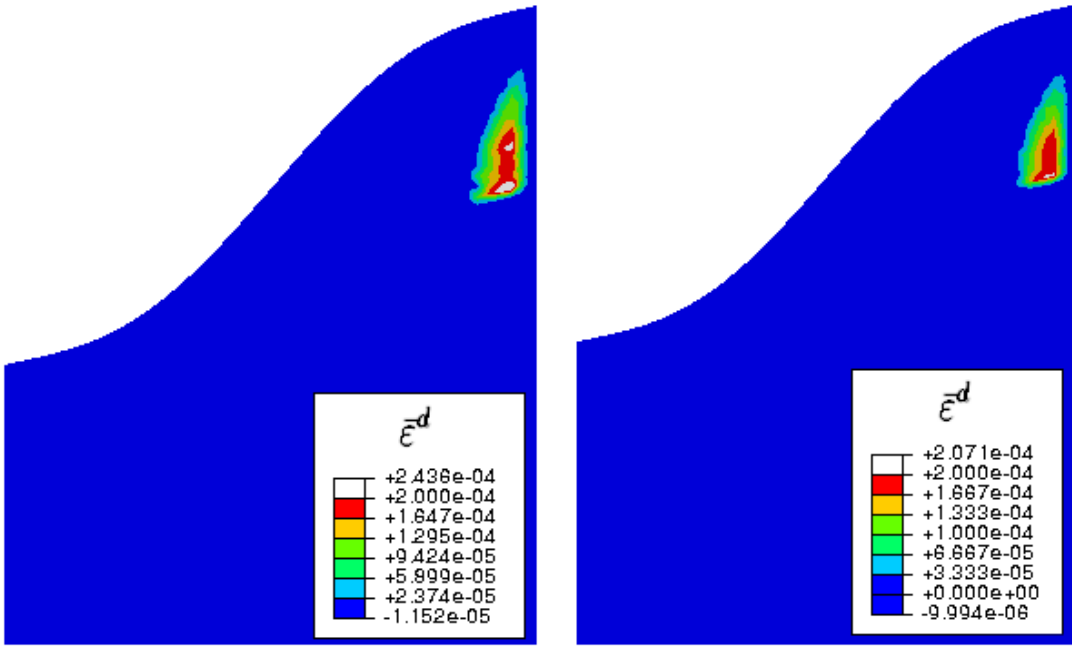


Figure 5.11: Damage contour for $S^d = 800\text{MPa}$ (left) and $S^d = 820\text{MPa}$ (right) after 200 hrs in the bond-coat.

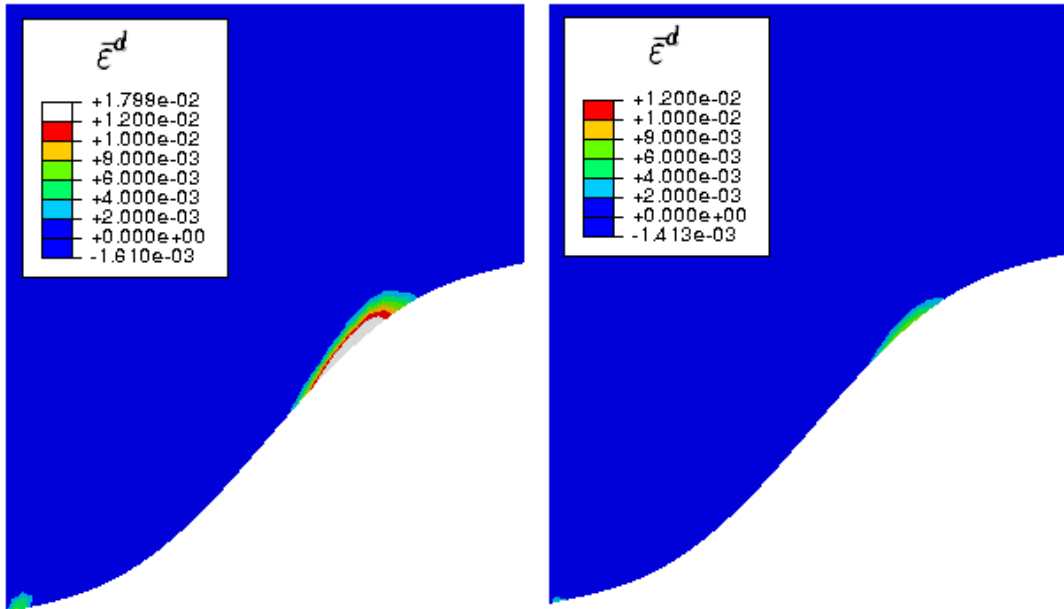


Figure 5.12: Damage contour for $S^d = 155\text{MPa}$ (left) and $S^d = 205\text{MPa}$ (right) after 200 hrs in the top-coat.

CHAPTER 6

CONCLUDING REMARKS

A finite element based phase-field model is developed in the large deformation framework for the oxidation of TBC systems at high temperatures. The phase-field approach and mechanics are fully coupled within the model, where the thermodynamic consistency is also ensured.

A numerical analysis is carried out for the progression of the TGO in a TBC system at 1200°C. The residual stresses achieved by the numerical simulation in the bond-coat are shown to be in good agreement with the experimental data.

The parametric study of the model is also conducted to investigate the effect of individual phase field and coupling parameters on the oxide growth rate. The results related to the calibration of the mechanical coupling parameter π demonstrate that the coupling parameter strongly connects the volumetric stress to the TGO growth rate.

The effect of creep on the oxidation induced stresses in the top-coat is also studied by including a Gurson-type inelasticity model in the ceramic coating. A considerable creep strain is observed in the ceramic coating, which leads to significant stress relaxation in the system in contrast to the models, where the top-coat is assumed to be elastic. The assumption of pure elastic behavior in the top-coat increases the stresses generated in the bond-coat, which results in shorter lifetime estimations.

Coupling the Allen-Cahn phase-field approach with mechanics, the presented model shows great potential for predicting the lifetime of TBC systems. Thus, additionally a damage model is coupled with the model. This approach successfully simulates the damage initiation in the TBC system, however much remains to be done for both propagation of TGO in the bond-coat and damage in the whole system.

6.1 Future works

In the context of future works, a few suggestions can be proposed for the further improvement of the main subroutine and individual models presented throughout this thesis. These are listed below.

a) Coupling temperature as an additional degree of freedom for thermal cyclic analysis. Thermal cyclic loading plays a very intense role in the evolution of residual stresses and the spallation of TBC systems. Thermo-mechanical coupling of the present subroutine will also provide a proper tool for analyzing structural instabilities like ratcheting in the bonding interface, which can be a critical factor in the failure mechanism [31].

b) Individual phase transitions of TC and TGO layers at different temperatures which affect the residual stresses in the structure can be also included in the model [76, 117, 118].

c) Non-local damage effects can be also considered using higher-order damage models for the ceramic top-coat. Localization of the micropores in the structure of the EB-PVD ceramic can lead to the development of micro-cracks. The effect of coalescence of these pores on the damage can be modeled via special gradient dependent plasticity enhanced damage models [119].

d) Due to the high mesh dependency of phase-field models, nanometer-size elements can be utilized in the case of access to a high computational power. Thus, phases interface length can be decreased to more realistic dimensions. Proper computational power can also facilitate 3D simulation of the entire blade geometry additionally.

e) Top-coat sintering is also an effective mechanism in TBC durability. High service temperature leads to a decrease in the intercolumnar and intercolumnar porosity and a decrease in the flexibility of the EB-PVD top-coat. Including a simple model for sintering in the top-coat can considerably affect the results [120].

f) The column orientation of top-coat is reported to be changing in the vicinity of the TC/BC interface. This anisotropy can be also considered in the mechanical behavior of the ceramic top-coat.

It worth noting that including all models in the routines may lead to divergence from the solution because coupling all these phenomena involves complex consistent tangent matrices in the FEM procedure, which can not always be calculated easily.

g) The amplitude of the undulations of the material interfaces can effect the magnitude of the stresses dramatically. The effect of the undulation shape on the stresses in the domain can be further investigated.

REFERENCES

- [1] E. A. Brandes and G. B. Brook, “Smithells Metals Reference Book: Seventh Edition,” *Smithells Metals Reference Book: Seventh Edition*, pp. 1–1800, 2013.
- [2] W. B. Pearson and G. H. Vineyard, “A Handbook of Lattice Spacings and Structures of Metals and Alloys,” *Physics Today*, vol. 11, no. 9, pp. 36–36, 1958.
- [3] Kevin G. Field, M. A. Snead, Y. Yamamoto, and K. A. Terrani, “Handbook on the Material Properties of FeCrAl Alloys for Nuclear Power Production Applications,” Tech. Rep. August, 2017.
- [4] S. L. Draper, J. Aikin, and J. Eldridge, “Tensile Behavior of Al₂O₃/FeAl Composites + B and Al₂O₃/FeCrAlY Composites,” *Metallurgical and Material Transactions A*, vol. 26, no. October 1995, 2017.
- [5] M. Y. He, J. W. Hutchinson, and A. G. Evans, “Large deformation simulations of cyclic displacement instabilities in thermal barrier systems,” *Acta Materialia*, vol. 50, no. 5, pp. 1063–1073, 2002.
- [6] B. Heeg, V. K. Tolpygo, and D. R. Clarke, “Damage evolution in thermal barrier coatings with thermal cycling,” *Journal of the American Ceramic Society*, vol. 94, no. SUPPL. 1, pp. 112–119, 2011.
- [7] T. J. Lu, C. G. Levi, H. N. G. Wadley, and A. G. Evans, “Distributed Porosity as a Control Parameter for Oxide Thermal Barriers Made by Physical Vapor Deposition,” *Journal of the American Ceramic Society*, vol. 84, no. 12, pp. 2937–2946, 2001.
- [8] R. G. Wellman and J. R. Nicholls, “On the effect of ageing on the erosion of EB-PVD TBCs,” *Surface and Coatings Technology*, vol. 177-178, pp. 80–88, 2004.

- [9] A. Azzopardi, R. Mévrel, B. Saint-Ramond, E. Olson, and K. Stiller, "Influence of aging on structure and thermal conductivity of Y-PSZ and Y-FSZ EB-PVD coatings," *Surface and Coatings Technology*, vol. 177-178, pp. 131–139, 2004.
- [10] X. Chunhua and G. Wei, "Pilling-Bedworth ratio for oxidation of alloys," *Mat Res innovat*, vol. 3, no. February 2000, pp. 231–235, 2000.
- [11] V. K. Tolpygo, J. R. Dryden, and D. R. Clarke, "Determination of the the Growth Stress and Strain in a Alumina Scales During the oxidation of Fe-22Cr-4.8Al-0.3Y Alloy," *Acta Metallurgica*, vol. 46, no. 3, pp. 927–937, 1998.
- [12] J. W. Cahn and J. E. Hilliard, "Free Energy of a Nonuniform System. I. Interfacial Free Energy," *The Journal of Chemical Physics*, vol. 28, no. 2, pp. 258–267, 1958.
- [13] V. K. Tolpygo, "Surface Rumpling of a (Ni, Pt) Al Bond Coat Induced by Cyclic Oxidation," *Acta mater.*, vol. 48, pp. 3283–3293, 2000.
- [14] V. K. Tolpygo and D. R. Clarke, "Wrinkling of [alpha]-alumina films grown by thermal oxidation–I. Quantitative studies on single crystals of Fe-Cr-Al alloy," *Acta Materialia*, vol. 46, no. 14, pp. 5153–5166, 1998.
- [15] M. E. Walter, B. Onipede, and C. Mercer, "Resulting From Isothermal and Thermocyclic Exposure of a Thermal Barrier Coating," *Journal of Engineering Materials and Technology*, vol. 122, no. 3, pp. 333–337, 2000.
- [16] S. Patsias, N. Tassini, and K. Lambrinou, "Ceramic coatings: Effect of deposition method on damping and modulus of elasticity for yttria-stabilized zirconia," *Materials Science and Engineering A*, vol. 442, no. 1-2 SPEC. ISS., pp. 504–508, 2006.
- [17] E. P. Busso and Z. Q. Qian, "A mechanistic study of microcracking in transversely isotropic ceramic-metal systems," *Acta Materialia*, 2006.
- [18] R. a. Miller, "Thermal barrier coatings for aircraft engines: History and directions," *Journal of Thermal Spray Technology*, vol. 6, no. 1, pp. 35–42, 1995.

- [19] F. Toriz, A. Thakker, and S. Gupta, "Thermal Barrier Coating for Jet Engines," in *International Gas Turbine and Aeroengine Congress and Exposition*, vol. 63, pp. 19–23, 1988.
- [20] J. T. DeMasi-Marcin, K. D. Sheffler, and S. Bose, "Mechanisms of Degradation and Failure in a Plasma-Deposited Thermal Barrier Coating," *Journal of Engineering for Gas Turbines and Power*, vol. 112, no. 4, pp. 521–526, 1990.
- [21] I. E. Sumner, "Development of Improved-durability Plasma Sprayed Ceramic Coatings for Gas Turbine Engines," *Sixteenth Joint Propulsion Conference cosponsored by the AIAA, ASME*, vol. Lewis Rese, 1980.
- [22] R. J. Bratton, S. K. Lau, and S. Y. Lee, "Evaluation of Present Thermal Barrier Coatings for Potential Service in Electric Utility Gas Turbines," *National Aeronautics and Space Administration*, vol. NASA CR-16, 1982.
- [23] S. Stecura, "Effects of Compositional Change on the Performance of a Thermal Barrier Coating System," *Nasa/Tm-78976*, vol. 78976, pp. 1–31, 1979.
- [24] A. G. Evans, D. R. Mumm, and J. W. Hutchinson, "Mechanisms controlling the durability of thermal barrier coatings," *Progress in Materials Science*, vol. 46, pp. 505–553, 2001.
- [25] A. G. Evans, D. R. Clarke, and C. G. Levi, "The influence of oxides on the performance of advanced gas turbines," *Journal of the European Ceramic Society*, vol. 28, no. 7, pp. 1405–1419, 2008.
- [26] J. Balmain, A. M. Huntz, and J. Philibert, "Atomic Transport Properties in Alumina Scales and Calculation of the Oxidation Parabolic Rate Constant," *Defect and Diffusion Forum*, vol. 143-147, pp. 1189–1194, 1997.
- [27] G. C. Chang, W. Phucharoen, and R. A. Miller, "Behavior of thermal barrier coatings for advanced gas turbine blades," *Surface and Coatings Technology*, vol. 30, no. 1, pp. 13–28, 1987.
- [28] A. M. Freborg, B. L. Ferguson, W. J. Brindley, and G. J. Petrus, "Modeling oxidation induced stresses in thermal barrier coatings," *Materials Science and Engineering A*, vol. 245, no. 2, pp. 182–190, 1998.

- [29] J. Cheng, E. Jordan, B. Barber, and M. Gell, "Thermal/residual stress in an electron beam physical vapor deposited thermal barrier coating system," *Acta Materialia*, vol. 46, no. 16, pp. 5839–5850, 1998.
- [30] C. H. Hsueii, P. F. Becher, E. R. Fuiler, S. A. Langer ', and W. C. Carter, "Surfnce-Roughness Induced Residual Stresses in Thermal Barrier Coatings: Computer Simulations," tech. rep., 1998.
- [31] M. Y. He, A. G. Evans, and J. W. Hutchinson, "Ratcheting of compressed thermally grown thin films on ductile substrates," *Acta Materialia*, vol. 48, no. 10, pp. 2593–2601, 2000.
- [32] M. Y. He, J. W. Hutchinson, and A. G. Evans, "Simulation of stresses and delamination in a plasma-sprayed thermal barrier system upon thermal cycling," *Materials Science and Engineering A*, vol. 345, no. 1-2, pp. 172–178, 2003.
- [33] T. Xu, M. Y. He, and A. G. Evans, "A numerical assessment of the durability of thermal barrier systems that fail by ratcheting of the thermally grown oxide," *Acta Materialia*, vol. 51, pp. 3807–3820, 2003.
- [34] D. Pan, M. W. Chen, P. K. Wright, and K. J. Hemker, "Evolution of a diffusion aluminide bond coat for thermal barrier coatings during thermal cycling," *Acta Materialia*, vol. 51, no. 8, pp. 2205–2217, 2003.
- [35] M. Caliez, F. Feyel, S. Kruch, and J.-L. Chaboche, "Oxidation induced stress fields in an EB-PVD thermal barrier coating," *Surface and Coatings Technology*, vol. 157, no. 2-3, pp. 103–110, 2002.
- [36] J. Rösler, M. Bäker, and M. Volgmann, "Stress state and failure mechanisms of thermal barrier coatings: Role of creep in thermally grown oxide," *Acta Materialia*, vol. 49, no. 18, pp. 3659–3670, 2001.
- [37] M. Bäker, J. Rösler, and G. Heinze, "A parametric study of the stress state of thermal barrier coatings Part II: Cooling stresses," *Acta Materialia*, vol. 53, no. 2, pp. 469–476, 2005.
- [38] A. F. Renteria and B. Saruhan, "Effect of ageing on microstructure changes in EB-PVD manufactured standard PYSZ top coat of thermal barrier coatings,"

Journal of the European Ceramic Society, vol. 26, no. 12, pp. 2249–2255, 2006.

- [39] U. Hermosilla, M. S. A. Karunaratne, I. A. Jones, T. H. Hyde, and R. C. Thomson, “Modelling the high temperature behaviour of TBCs using sequentially coupled microstructural-mechanical FE analyses,” *Materials Science and Engineering A*, 2009.
- [40] L. Anand, “A thermo-mechanically-coupled theory accounting for hydrogen diffusion and large elastic-viscoplastic deformations of metals,” *International Journal of Solids and Structures*, vol. 48, no. 6, pp. 962–971, 2011.
- [41] K. Loeffel and L. Anand, “A chemo-thermo-mechanically coupled theory for elastic-viscoplastic deformation, diffusion, and volumetric swelling due to a chemical reaction,” *International Journal of Plasticity*, vol. 27, no. 9, pp. 1409–1431, 2011.
- [42] K. Al-Athel, K. Loeffel, H. Liu, and L. Anand, “Modeling decohesion of a top-coat from a thermally-growing oxide in a thermal barrier coating,” *Surface and Coatings Technology*, vol. 222, pp. 68–78, 2013.
- [43] K. Ammar, B. Appolaire, G. Cailletaud, F. Feyel, and S. Forest, “Finite element formulation of a phase field model based on the concept of generalized stresses,” *Computational Materials Science*, vol. 45, no. 3, pp. 800–805, 2009.
- [44] E. P. Busso, H. E. Evans, Z. Q. Qian, and M. P. Taylor, “Effects of break-away oxidation on local stresses in thermal barrier coatings,” *Acta Materialia*, vol. 58, no. 4, pp. 1242–1251, 2010.
- [45] J. Frachon, “Multiscale approach to predict the lifetime of EB-PVD thermal barrier coatings,” *Thesis, Ecole Nationale Supérieure des Mines de Paris*, 2013.
- [46] K. Ammar, “Modelling and simulation of phase transformation-mechanics coupling using a phase field method Kais Ammar l’École nationale supérieure des mines de Paris Spécialité « Sciences et Génie des Matériaux » Modelling and Simulation of Phase Transformation-Mec,” 2010.

- [47] S. A. Chester and L. Anand, “A thermo-mechanically coupled theory for fluid permeation in elastomeric materials: Application to thermally responsive gels,” 2011.
- [48] H. Dal and C. Miehe, “Computational electro-chemo-mechanics of lithium-ion battery electrodes at finite strains,” *Computational Mechanics*, vol. 55, no. 2, pp. 303–325, 2014.
- [49] T. S. Hille, S. Turteltaub, and A. S. Suiker, “Oxide growth and damage evolution in thermal barrier coatings,” *Engineering Fracture Mechanics*, vol. 78, no. 10, pp. 2139–2152, 2011.
- [50] K. Loeffel, L. Anand, and Z. M. Gasem, “On modeling the oxidation of high-temperature alloys,” *Acta Materialia*, vol. 61, no. 2, pp. 399–424, 2013.
- [51] N. Pilling and R. E. Bedworth, “The Oxidation of Metals at High Temperatures,” *J. Inst. Met*, vol. 29, pp. 529–591, 1923.
- [52] D. R. Clarke, “The lateral growth strain accompanying the formation of a thermally grown oxide,” *Acta Materialia*, vol. 51, pp. 1393–1407, 2003.
- [53] Louis R. Rossi and Willis G. Lawrence, “Elastic Properties of Oxide Solid Solutions: The System $\text{Al}_2\text{O}_3\text{-Cr}_2\text{O}_3$,” *Journal of American Ceramic Society*, vol. 53, no. 11, pp. 604–608, 1970.
- [54] F. N. Rhines and J. S. Wolf, “The role of oxide microstructure and growth stresses in the high-temperature scaling of nickel,” *Metallurgical Transactions*, vol. 1, no. 6, pp. 1701–1710, 1970.
- [55] M. C. Stasik, F. S. Pettit, G. H. Meier, A. Ashary, and J. L. Smialek, “Effects of reactive element additions and sulfur removal on the oxidation behavior of ferral alloys,” *Scripta Metallurgica et Materiala*, vol. 31, no. 12, pp. 1645–1650, 1994.
- [56] V. L. Ginzburg and L. D. Landau, “On the Theory of Superconductivity,” in *On Superconductivity and Superfluidity: A Scientific Autobiography*, pp. 113–137, Berlin, Heidelberg: Springer Berlin Heidelberg, 2009.

- [57] J. W. Cahn, "On spinodal decomposition," *Acta Metallurgica*, vol. 9, no. 9, pp. 795–801, 1961.
- [58] J. W. CAHN, W. B. Hilligs, and G. W. Sears, "The Molecular Mechanism of Solidification," *Acta Metallurgica*, vol. 12, no. December, p. 231, 1964.
- [59] J. E. Morral and J. W. Cahn, "Spinodal decomposition in ternary systems," *Acta Metallurgica*, vol. 19, no. 10, pp. 1037–1045, 1971.
- [60] J. S. Langer, M. Bar-on, and H. D. Miller, "New computational method in the theory of spinodal decomposition*," *Physical Review A*, vol. 11, no. 4, 1974.
- [61] M. E. Gurtin, "On a Nonequilibrium Thermodynamics of Capillary and Phase," *Q.Appl.Math.*, vol. 47, no. 1, pp. 129–145, 1989.
- [62] L. Q. Chen and A. G. Khachaturyan, "Computer simulation of structural transformations during precipitation of an ordered intermetallic phase," *Acta Metallurgica Et Materialia*, vol. 39, no. 11, pp. 2533–2551, 1991.
- [63] L. Q. Chen and A. G. Khachaturyan, "Formation of virtual ordered states along a phase-decomposition path Long-Qing," *Physical Review B*, vol. 44, no. 9, pp. 4681–4684, 1991.
- [64] L. Q. Chen, Y. Wang, and A. G. Khachaturyan, "Transformation-induced elastic strain effect on the precipitation kinetics of ordered intermetallics," *Philosophical Magazine Letters*, vol. 64, no. 5, pp. 241–251, 1991.
- [65] J. Wang and A. P. Young, "Monte Carlo study of the six-dimensional Ising spin glass," *Journal of Physics A: Mathematical and General*, vol. 26, no. 5, p. 1063, 1993.
- [66] M. E. Gurtin and P. W. Voorhees, "The thermodynamics of evolving interfaces far from equilibrium," *Acta Materialia*, vol. 44, no. 1, pp. 235–247, 1996.
- [67] M. Takenaka and T. Hashimoto, "Computer simulation of the spinodal decomposition for a polydisperse polymer mixture," *Physical Review E*, vol. 48, no. 2, p. R647, 1993.
- [68] J. W. Cahn and J. E. Taylor, "Surface Motion by Surface Diffusion," *Acta Metallurgica Et Materialia*, vol. 42, no. 4, pp. 1045–1063, 1994.

- [69] A. A. Wheeler, W. J. Boettinger, and G. B. McFadden, "Phase-field model for isothermal phase transitions in binary alloys," *Physical Review A*, vol. 45, no. 10, pp. 7424–7439, 1992.
- [70] S. M. Allen and J. W. Cahn, "A microscopic theory for antiphase boundary motion and its application to antiphase domain coarsening," *Acta Metallurgica*, vol. 27, no. 6, pp. 1085–1095, 1979.
- [71] S. G. Kim, W. T. Kim, and T. Suzuki, "Phase-field model for binary alloys.," *Physical review. E, Statistical physics, plasmas, fluids, and related interdisciplinary topics*, vol. 60, no. 6 Pt B, pp. 7186–7197, 1999.
- [72] C. V. Di Leo, E. Rejovitzky, and L. Anand, "A Cahn-Hilliard-type phase-field theory for species diffusion coupled with large elastic deformations: Application to phase-separating Li-ion electrode materials," *Journal of the Mechanics and Physics of Solids*, vol. 70, no. 1, pp. 1–29, 2014.
- [73] J. S. Rowlinson, "Translation of J. D. van der Waals' "The thermodynamik theory of capillarity under the hypothesis of a continuous variation of density";," *Journal of Statistical Physics*, vol. 20, no. 2, pp. 197–200, 1979.
- [74] P. Yue, J. J. Feng, C. Liu, and J. Shen, "A diffuse-interface method for simulating two-phase flows of complex fluids," *Journal of Fluid Mechanics*, vol. 515, pp. 293–317, 2004.
- [75] R. DeHoff, *Thermodynamics in Materials Science*. Taylor & Francis, 2006.
- [76] B. A. Pint, J. R. Martin, and L. W. Hobbs, "The oxidation mechanism of θ -Al₂O₃ scales," *Solid State Ionics*, vol. 78, no. 1-2, pp. 99–107, 1995.
- [77] M. W. Brumm and H. J. Grabke, "The oxidation behaviour of NiAl-I. Phase transformations in the alumina scale during oxidation of NiAl and NiAl-Cr alloys," *Corrosion Science*, vol. 33, no. 11, pp. 1677–1690, 1992.
- [78] Kaspar Andreas Loeffel, *On the oxidation of high-temperature alloys , and its role in failure of thermal barrier coatings by*. PhD thesis, Massachusetts Institute of Technology, 2013.

- [79] P. Y. Hou, A. P. Paulikas, B. W. Veal, and J. L. Smialek, “Thermally grown Al₂O₃ on a H₂-annealed Fe₃Al alloy: Stress evolution and film adhesion,” *Acta Materialia*, vol. 55, no. 16, pp. 5601–5613, 2007.
- [80] Y. Wang, M. X. Li, and H. L. Suo, “Mechanical properties of YSZ thermal barrier coatings with segmented structure,” *Surface Engineering*, vol. 28, no. 5, pp. 329–332, 2012.
- [81] B. Echebarria, R. Folch, A. Karma, and M. Plapp, “Quantitative phase-field model of alloy solidification,” *Physical Review E - Statistical Physics, Plasmas, Fluids, and Related Interdisciplinary Topics*, vol. 70, no. 6, p. 22, 2004.
- [82] R. Chella, “Mixing two-phase cavity,” *Physical Review E*, vol. 53, no. 4, 1996.
- [83] K. Ammar, B. Appolaire, S. Forest, M. Cottura, Y. L. Bouar, and A. Finel, “Modelling inheritance of plastic deformation during migration of phase boundaries using a phase field method,” *Meccanica*, vol. 49, no. 11, pp. 2699–2717, 2014.
- [84] S. A. Chester, *Signature redacted Signature redacted Signature redacted MIT Libraries Pages 357-573*. PhD thesis, Massachusetts Institute of Technology, 2011.
- [85] E. Kröner, “Allgemeine Kontinuumstheorie der Versetzungen und Eigenspannungen,” *Archive for Rational Mechanics and Analysis*, vol. 4, no. 1, pp. 273–334, 1959.
- [86] F. Saeidi, E. Gurses, and O. Aslan, “A Numerical Approach to Simulate Oxidation in Thermal Barrier Coatings,” in *Reference Module in Materials Science and Materials Engineering* (S. Hashmi and I. A. Choudhury, eds.), pp. 986–992, Elsevier Ltd., 2020.
- [87] C. V. Di Leo, *Chemo-Mechanics of Lithium-Ion Battery Electrodes*. PhD thesis, Massachusetts Institute of Technology, 2015.
- [88] M. Gurtin, E. Fried, and L. Anand, *The mechanics and thermodynamics of continua*, vol. 53. 2013.

- [89] M. E. Gurtin, "Generalized Ginzburg-Landau and Cahn-Hilliard equations based on a microforce balance," *Physica D*, vol. 96, pp. 178–192, 1996.
- [90] S. G. Kim, W. T. Kim, and T. Suzuki, "Interfacial compositions of solid and liquid in a phase-field model with finite interface thickness for isothermal solidification in binary alloys," *Physical Review E - Statistical Physics, Plasmas, Fluids, and Related Interdisciplinary Topics*, vol. 58, no. 3, pp. 3316–3323, 1998.
- [91] R. W. Grimes and K. P. D. Lagerlo, "The Defect Chemistry of Sapphire (a -Al₂O₃)," *Acta mater.*, vol. 46, no. 16, pp. 5689–5700, 1998.
- [92] K. Vaidyanathan, M. Gell, and E. Jordan, "Mechanisms of spallation of electron beam physical vapor deposited thermal barrier coatings with and without platinum aluminide bond coat ridges," *Surface and Coatings Technology*, vol. 133-134, pp. 28–34, 2000.
- [93] A. I. Zavaliangos, *Elasto-viscoplasticity of Isotropic Porous Metals*. PhD thesis, Massachusetts institute of technology, 1992.
- [94] M. Haghi and L. Anand, "A constitutive model for isotropic, porous, elastic-viscoplastic metals," *Mechanics of Materials*, vol. 13, no. 1, pp. 37–53, 1992.
- [95] A. I. Zavaliangos and L. Anand, "Thermo-elasto-viscoplasticity of Isotropic Porous Metals," *Journal of Mechanics and Physics of Solids*, vol. 41, no. 6, pp. 1087–1118, 1993.
- [96] L. Anand, "Constitutive Equations for the Rate-Dependent Deformation of Metals at Elevated Temperatures," *Journal of Engineering Materials and Technology*, vol. 104, no. 1, pp. 12–17, 1982.
- [97] N. B. Dahotre, J. M. Hampikian, and J. E. Morral, *Elevated Temperature Coatings: Science and Technology IV*. Wiley-Tms, 2013.
- [98] L. Anand, "Introduction to Plasticity Lecture Notes (Draft)," Cambridge, 2009.
- [99] O. Altun and Y. E. Boke, "Heat Transfer Analysis of Thermal Barrier Coatings

- on a Metal Substrate,” *Journal of Thermal Science and Technology*, no. January, pp. 101–109, 2013.
- [100] H. Echsler, D. Renusch, and M. Schütze, “Mechanical behaviour of as sprayed and sintered air plasma sprayed partially stabilised zirconia,” *Materials Science and Technology*, vol. 20, no. 7, pp. 869–876, 2004.
- [101] P. F. Tortorelli, K. L. More, E. D. Specht, B. A. Pint, and P. Zschack, “Growth stress - Microstructure relationships for alumina scales,” *Materials at High Temperatures*, vol. 20, no. 3, pp. 303–310, 2003.
- [102] T. Tomimatsu, S. Zhu, and Y. Kagawa, “Effect of thermal exposure on stress distribution in TGO layer of EB-PVD TBC,” *Acta Materialia*, vol. 51, no. 8, pp. 2397–2405, 2003.
- [103] a.G. Evans, M. He, and J. Hutchinson, “Effect of interface undulations on the thermal fatigue of thin films and scales on metal substrates,” *Acta Materialia*, vol. 45, no. 9, pp. 3543–3554, 1997.
- [104] D. Mumm and A. Evans, “Failure of a thermal barrier system due to a cyclic displacement instability in the thermally grown oxide,” *Materials Research Society Symposium Proceedings*, vol. 645, pp. 2329–2340, 2001.
- [105] M. D. Thouless, H. M. Jensen, and E. G. Liniger, “Delamination from edge flaws,” *Proceedings of the Royal Society A: Mathematical, Physical and Engineering Sciences*, vol. 447, no. 1930, pp. 271–279, 1994.
- [106] M. Caliez, J. L. Chaboche, F. Feyel, and S. Kruch, “Numerical simulation of EBPVD thermal barrier coatings spallation,” *Acta Materialia*, vol. 51, no. 4, pp. 1133–1141, 2003.
- [107] J. Aktaa, K. Sfar, and D. Munz, “Assessment of TBC systems failure mechanisms using a fracture mechanics approach,” *Acta Materialia*, vol. 53, no. 16, pp. 4399–4413, 2005.
- [108] M. Białas, “Finite element analysis of stress distribution in thermal barrier coatings,” *Surface and Coatings Technology*, vol. 202, no. 24, pp. 6002–6010, 2008.

- [109] P. Bednarz, *Finite Element Simulation of Stress Evolution in Thermal Barrier Coating Systems*, vol. 60. Forschungszentrum Jülich GmbH, 2007.
- [110] K. Sfar, J. Aktaa, and D. Munz, “Numerical investigation of residual stress fields and crack behavior in TBC systems,” *Materials Science and Engineering A*, vol. 333, no. 1-2, pp. 351–360, 2002.
- [111] S. T. Kyaw, I. A. Jones, and T. H. Hyde, “Simulation of failure of air plasma sprayed thermal barrier coating due to interfacial and bulk cracks using surface-based cohesive interaction and extended finite element method,” *Journal of Strain Analysis for Engineering Design*, vol. 51, no. 2, pp. 132–143, 2016.
- [112] G. Z. Voyiadjis and T. Park, “Kinematics of damage for finite-strain elasto-plastic solids,” *International Journal of Engineering Science*, vol. 37, no. 7, pp. 803–830, 1999.
- [113] T. Park, “Kinematic Description of Damage,” *Journal of Applied Mechanics*, vol. 65, no. March 1998, pp. 93–98, 2016.
- [114] G. Weber and L. Anand, “Finite deformation constitutive equations and a time integration procedure for isotropic, hyperelastic-viscoplastic solids,” *Computer Methods in Applied Mechanics and Engineering*, vol. 79, no. 2, pp. 173–202, 1990.
- [115] V. K. Tolpygo, D. R. Clarke, and K. S. Murphy, “Oxidation-induced failure of EB-PVD thermal barrier coatings,” *Surface and Coatings Technology*, vol. 146-147, pp. 124–131, 2001.
- [116] V. Lughi, V. K. Tolpygo, and D. R. Clarke, “Microstructural aspects of the sintering of thermal barrier coatings,” *Materials Science and Engineering A*, vol. A368, pp. 212–221, 2004.
- [117] Y. H. Sohn and R. R. Biederman, “Partially Stabilized Zirconia Thermal Barrier Coatings,” *Journal of Materials Engineering and Performance*, vol. 3, no. February, pp. 55–60, 1994.

- [118] J. R. VanValzah and H. E. Eaton, "Cooling rate effects on the tetragonal to monoclinic phase transformation in aged plasma-sprayed yttria partially stabilized zirconia," *Surface and Coatings Technology*, vol. 46, no. 3, pp. 289–300, 1991.
- [119] R. A. B. Engelen, *Plasticity-induced damage in metals : nonlocal modelling at finite strains*. No. 2005, Eindhoven: R.A.B. Engelen, 2005.
- [120] E. P. Busso, Z. Q. Qian, M. P. Taylor, and H. E. Evans, "The influence of bondcoat and topcoat mechanical properties on stress development in thermal barrier coating systems," *Acta Materialia*, vol. 57, no. 8, pp. 2349–2361, 2009.
- [121] R. L. Ubachs, P. J. Schreurs, and M. G. Geers, "A nonlocal diffuse interface model for microstructure evolution of tin-lead solder," *Journal of the Mechanics and Physics of Solids*, vol. 52, no. 8, pp. 1763–1792, 2004.
- [122] R. H. Peerlings, R. De Borst, W. A. Brekelmans, and J. H. De Vree, "Gradient enhanced damage for quasi-brittle materials," *International Journal for Numerical Methods in Engineering*, vol. 39, no. 19, pp. 3391–3403, 1996.
- [123] a. Einstein, "Über die von der molekularkinetischen Theorie der Wärme geforderte Bewegung von in ruhenden Flüssigkeiten suspendierten Teilchen," *Ann. d. Phys.*, vol. 322, no. 8, pp. 549–560, 1905.
- [124] R. M. Spriggs and L. A. Brissette, "Expressions for Shear Modulus and Poisson's Ratio of Porous Refractory Oxides," *Journal of the American Ceramic Society*, vol. 45, no. 4, pp. 198–199, 1962.
- [125] R. Morrell, *Handbook of properties of technical & engineering ceramics*. No. pt. 2 in Handbook of Properties of Technical & Engineering Ceramics, H.M.S.O, 1987.
- [126] J. H. Gieske and G. R. Barsch, "Pressure Dependence of the Elastic Constants of Single Crystalline Aluminum Oxide," *Physica Status Solidi (B)*, vol. 29, no. 1, pp. 121–131, 1968.
- [127] P. Auerkari, "Mechanical and physical properties of engineering alumina ceramics," *VTT Tiedotteita - Valtion Teknillinen Tutkimuskeskus*, no. 1792, 1996.

- [128] K. Komeya and M. Matsui, "High Temperature Engineering Ceramics," *Materials Science and Technology*, 2006.
- [129] J. Castaing, J. Cadoz, and S. H. Kirby, "Deformation of Al₂O₃ Single Crystals Between 25°C and 1800°C: Basal and Prismatic Slip," *Le Journal de Physique Colloques*, vol. 42, no. C3, pp. C3-43-C3-47, 2007.
- [130] E. Souza Neto, P. D., and O. DRJ, *Computational methods for Plasticity*. Wiley, 2008.

APPENDIX A

TIME INTEGRATION FOR VISCOPLASTIC RESPONSE

A.1 Time integration for bond-coat material model

A summary of the time integration procedure for the model is presented below. Terms with * are the trial values. For a displacement driven analysis the deformation gradient is known, thus a trial elastic deformation gradient using the Kröner's decomposition can be calculated.

$$\mathbf{F}_{n+1}^{e*} = \mathbf{F}_{n+1}(\mathbf{F}_n^i)^{-1} \quad (\text{A.1})$$

where,

$$\mathbf{F}_{n+1}^i = \exp(\Delta t \mathbf{D}_{n+1}^i) \mathbf{F}_n^i \quad (\text{A.2})$$

The polar decomposition is applied and elastic strain tensor \mathbf{E}_{n+1}^{e*} and elastic right Cauchy-Green tensor \mathbf{C}_{n+1}^{e*} are found.

$$\mathbf{F}_{n+1}^e = \mathbf{R}_{n+1}^e \mathbf{U}_{n+1}^e \quad (\text{A.3})$$

$$\mathbf{F}_{n+1}^{e*} = \mathbf{R}_{n+1}^{e*} \mathbf{U}_{n+1}^{e*} \quad (\text{A.4})$$

$$\mathbf{E}_{n+1}^{e*} = \ln(\mathbf{U}_{n+1}^{e*}) \quad (\text{A.5})$$

$$\mathbf{C}_{n+1}^{e*} = (\mathbf{U}_{n+1}^{e*})^2 \quad (\text{A.6})$$

$$\mathbf{C}_{n+1}^e = (\mathbf{U}_{n+1}^e)^2 \quad (\text{A.7})$$

The elastic right Cauchy-green tensor is defined as,

$$\mathbf{C}_{n+1}^{e*} = \mathbf{F}_{n+1}^{e*T} \mathbf{F}_{n+1}^{e*} \quad (\text{A.8})$$

$$\mathbf{C}_{n+1}^e = \mathbf{F}_{n+1}^{eT} \mathbf{F}_{n+1}^e \quad (\text{A.9})$$

Hence, using equations above one can obtain,

$$\mathbf{R}_{n+1}^e \mathbf{U}_{n+1}^e \exp(\Delta t \mathbf{D}_{n+1}^i) = \mathbf{R}_{n+1}^{e*} \mathbf{U}_{n+1}^{e*} \quad (\text{A.10})$$

Here we make the following assumption to further simplify the procedure,

$$\mathbf{R}_{n+1}^e = \mathbf{R}_{n+1}^{e*} \quad (\text{A.11})$$

$$\mathbf{U}_{n+1}^e \exp(\Delta t \mathbf{D}_{n+1}^i) = \mathbf{U}_{n+1}^{e*} \quad (\text{A.12})$$

thus,

$$\mathbf{C}_{n+1}^e = \exp(-\Delta t \mathbf{D}_{n+1}^i) \mathbf{C}_{n+1}^{e*} \exp(-\Delta t \mathbf{D}_{n+1}^i) \quad (\text{A.13})$$

Using the series expansion of the exponential function and eliminating the higher order terms by assuming a small time step one can write,

$$\exp(-\Delta t \mathbf{D}_{n+1}^i) = 1 - \Delta t \mathbf{D}_{n+1}^i \quad (\text{A.14})$$

As a result the elastic right Cauchy-Green tensor can be written as,

$$\mathbf{C}_{n+1}^e = (1 - \Delta t \mathbf{D}_{n+1}^i) \mathbf{C}_{n+1}^{e*} (1 - \Delta t \mathbf{D}_{n+1}^i) \quad (\text{A.15})$$

The trail elastic Green strain tensor is,

$$\mathbf{E}_{n+1}^{e*} = \frac{1}{2} (\mathbf{C}_{n+1}^{e*} - \mathbf{1}) \quad (\text{A.16})$$

Assuming strains are not very large the expression for the right Cauchy-Green tensor can be simplified to the expression below by neglecting higher order terms.

$$\mathbf{C}_{n+1}^e = \mathbf{C}_{n+1}^{e*} (1 - 2\Delta t \mathbf{D}_{n+1}^i) \quad (\text{A.17})$$

Taking the logarithm of the both sides one can write,

$$\mathbf{E}_{n+1}^e = \mathbf{E}_{n+1}^{e*} + \frac{1}{2} \ln(1 - 2\Delta t \mathbf{D}_{n+1}^i) \quad (\text{A.18})$$

Knowing that function $f(x) = \ln(1 - x)$ for $x \approx 0$ can be approximated to $f(x) = -x$, the equation above can also be approximated to,

$$\mathbf{E}_{n+1}^e = \mathbf{E}_{n+1}^{e*} - \Delta t \mathbf{D}_{n+1}^i \quad (\text{A.19})$$

The Mandel stress is then calculated.

$$\mathbf{M}_{n+1}^e = \mathbb{C} : \mathbf{E}_{n+1}^e \quad (\text{A.20})$$

Thus (A.20) together with equation (A.19) can be written as,

$$\mathbf{M}_{n+1}^e = \mathbf{M}_{n+1}^{e*} - \mathbb{C} : (\Delta t \mathbf{D}_{n+1}^i) \quad (\text{A.21})$$

where,

$$\mathbf{M}^{e*} = \mathbb{C}\mathbf{E}_{n+1}^{e*} = 2\mu\mathbf{E}_{n+1}^{e*} + \lambda\text{tr}(\mathbf{E}_{n+1}^{e*}) \quad (\text{A.22})$$

\mathbb{C} is the fourth-order isotropic elasticity tensor and μ and λ are the Lamé constants. Then, the deviatoric Mandel stress is obtained as,

$$\mathbf{M}_0^{e*} = \mathbf{M}^{e*} + \frac{1}{3}P^*\mathbf{1} \quad (\text{A.23})$$

where P^* is the pressure.

$$P^* = -\frac{1}{3}\text{tr}(\mathbf{M}^{e*}) \quad (\text{A.24})$$

The equivalent stress is,

$$\bar{\sigma}_{n+1}^* = \sqrt{\frac{3}{2}\mathbf{M}_0^{e*}\mathbf{M}_0^{e*}} \quad (\text{A.25})$$

From equation (5.16) one can write,

$$\bar{\sigma}_{n+1} = S_{\alpha_{n+1}}\left(\frac{\dot{\bar{\epsilon}}_p}{\dot{\bar{\epsilon}}_0}\right)^m + \Delta th\dot{\bar{\epsilon}}_p \quad (\text{A.26})$$

Having found the equivalent plastic strain rate, the new plastic stretch tensor for multiphase region can be found using the following equation.

$$\mathbf{D}_{n+1}^p = \sqrt{\frac{3}{2}\dot{\bar{\epsilon}}_p^p}\mathbf{N}_{n+1}^p \quad (\text{A.27})$$

where,

$$\mathbf{N}_{n+1}^{p*} = \mathbf{N}_{n+1}^p = \sqrt{\frac{3}{2}\left(\frac{\mathbf{M}_0^{e*}}{\bar{\sigma}_{n+1}^*}\right)} \quad (\text{A.28})$$

The swelling stretching tensor is calculated using order parameter rate and the swelling tensor \mathbf{S}_{n+1} defined in equation (4.15).

$$\mathbf{D}_{n+1}^S = \dot{\phi}_{n+1} \mathbf{S}_{n+1} \quad (\text{A.29})$$

Then inelastic stretch tensor is calculated as,

$$\mathbf{D}_{n+1}^i = \mathbf{D}_{n+1}^p + \mathbf{D}_{n+1}^S \quad (\text{A.30})$$

The evolution equation $\dot{\mathbf{F}}^i = \mathbf{D}^i \mathbf{F}^i$ is integrated using the exponential mapping [114].

$$\mathbf{F}_{n+1}^i = \exp(\Delta t \mathbf{D}_{n+1}^i) \mathbf{F}_n^i \quad (\text{A.31})$$

Using equation (A.19) and (A.22),

$$\mathbf{M}^e = \mathbf{M}^{e*} - 2G\Delta t \mathbf{D}_{n+1}^i - \lambda\Delta t (\text{tr} \mathbf{D}_{n+1}^i) \mathbf{1} \quad (\text{A.32})$$

For the bond-coat material due to oxidation induced volumetric swelling is,

$$\text{tr} \mathbf{D}_{n+1}^i = \dot{\phi} \text{tr}(\mathbf{S}_{n+1}) \quad (\text{A.33})$$

Then using equations (A.27)-(A.33) for the bond-coat it can be written that,

$$\mathbf{M}^e = \mathbf{M}^{e*} - 2G\Delta t \left(\sqrt{\frac{3}{2}} \dot{\varepsilon}_\alpha^p \mathbf{N}_{n+1}^p + \dot{\phi}_{n+1} \mathbf{S}_{n+1} \right) - \lambda\Delta t (\dot{\phi} \text{tr}(\mathbf{S}_{n+1})) \mathbf{1} \quad (\text{A.34})$$

Using equations (A.28), (A.29), (A.34) and doing some calculations one can write (for details see [78]) the following equation containing $\dot{\varepsilon}^p$ as the only unknown.

$$\bar{\sigma}_{n+1} + 3G\Delta t \dot{\varepsilon}_\alpha^p - \sqrt{(\bar{\sigma}_{n+1}^*)^2 - 2G\Delta t \dot{\phi} (\sqrt{6} \bar{\sigma}_{n+1}^* \mathbf{N}_{n+1}^{p*} : \mathbf{S}_{0n+1} - 2G\Delta t \dot{\phi} (\beta_t - \beta_l))} = 0 \quad (\text{A.35})$$

where \mathbf{S}_{0n+1} is the deviatoric part of the swelling tensor \mathbf{S}_{n+1} .

A.2 Summery of the time integration

Step 1. The trial elastic deformation gradient is calculated.

$$\mathbf{F}_{n+1}^{e*} = \mathbf{F}_{n+1}(\mathbf{F}_n^i)^{-1} \quad (\text{A.36})$$

Step 2. The trail strain tensor is calculated by decomposing the deformation gradient.

$$\mathbf{E}_{n+1}^{e*} = \ln(\mathbf{U}_{n+1}^{e*}) \quad (\text{A.37})$$

Step 3. The trail Mandel stress and its deviatoric part are calculated.

$$\mathbf{M}^{e*} = \mathbb{C} : \mathbf{E}_{n+1}^{e*} \quad (\text{A.38})$$

$$\bar{\sigma}_{n+1}^* = \sqrt{\frac{3}{2} \mathbf{M}_0^{e*} : \mathbf{M}_0^{e*}} \quad (\text{A.39})$$

Step 4. Plastic flow direction is calculated.

$$\mathbf{N}_{n+1}^{p*} = \mathbf{N}_{n+1}^p = \sqrt{\frac{3}{2}} \left(\frac{\mathbf{M}_0^{e*}}{\bar{\sigma}_{n+1}^*} \right) \quad (\text{A.40})$$

Step 5. Solving the following equation implicitly $\dot{\varepsilon}^p$ is calculated.

$$\bar{\sigma}_{n+1} + 3G\Delta t \dot{\varepsilon}_\alpha^p - \sqrt{(\bar{\sigma}^*)^2 - 2G\Delta t \dot{\phi}(\sqrt{6}\bar{\sigma}^* \mathbf{N}_{n+1}^{p*} : \mathbf{S}_{0n+1} - 2G\Delta t \dot{\phi}(\beta_t - \beta_i))} = 0 \quad (\text{A.41})$$

where $\bar{\sigma}$ is defined to be,

$$\bar{\sigma}_{n+1} = S_\alpha \left(\frac{\dot{\varepsilon}_\alpha^p}{\dot{\varepsilon}_0} \right)^m + \Delta t h \dot{\varepsilon}_\alpha^p \quad (\text{A.42})$$

Step 6. Total equivalent plastic strain rate is calculated.

$$\dot{\tilde{\epsilon}}_{\alpha}^p = \phi \dot{\tilde{\epsilon}}_{ox}^p + (1 - \phi) \dot{\tilde{\epsilon}}_{bc}^p \quad (\text{A.43})$$

Step 7. Inelastic stretching tensor is calculated.

$$\mathbf{D}_{n+1}^p = \sqrt{\frac{3}{2}} \dot{\tilde{\epsilon}}^p \mathbf{N}_{n+1}^p \quad (\text{A.44})$$

$$\mathbf{D}_{n+1}^S = \dot{\phi}_{n+1} \mathbf{S}_{n+1} \quad (\text{A.45})$$

$$\mathbf{D}_{n+1}^i = \mathbf{D}_{n+1}^p + \mathbf{D}_{n+1}^S \quad (\text{A.46})$$

Step 8. The inelastic deformation gradient is calculated.

$$\mathbf{F}_{n+1}^i = \exp(\Delta t \mathbf{D}_{n+1}^i) \mathbf{F}_n^i \quad (\text{A.47})$$

Step 9. Elastic strain is updated using polar decomposition and stresses are updated.

$$\mathbf{M}_{n+1}^e = \mathbb{C} : \mathbf{E}_{n+1}^e \quad (\text{A.48})$$

A.3 Time integration for top-coat material model

A summary for the time integration for the Gurson type material model used for top-coat is presented below, see [93].

Step 1. The trial elastic deformation gradient is calculated.

$$\mathbf{F}_{n+1}^{e*} = \mathbf{F}_{n+1} (\mathbf{F}_n^i)^{-1} \quad (\text{A.49})$$

Step 2. The trail elastic strain tensor is calculated by decomposing deformation gradient.

$$\mathbf{E}_{n+1}^{e*} = \ln(\mathbf{U}_{n+1}^{e*}) \quad (\text{A.50})$$

Step 3. The trail Mandel stress and its deviatoric and volumetric parts are calculated.

$$\mathbf{M}^{e*} = \mathbb{C} : \mathbf{E}_{n+1}^{e*} \quad (\text{A.51})$$

$$\bar{\sigma}'^* = \sqrt{\frac{3}{2} \mathbf{M}_0^{e*} : \mathbf{M}_0^{e*}} \quad (\text{A.52})$$

$$\bar{\sigma}_v^* = \frac{1}{3} \text{tr}(\mathbf{M}^{e*}) \quad (\text{A.53})$$

Step 4. The equivalent deviatoric stress and equivalent plastic strain rate for the matrix are calculated.

$$\bar{\sigma}_m^* = \kappa(F)^{\frac{m}{m+1}} \cdot \bar{\sigma}'^* \quad (\text{A.54})$$

where κ and F are the porosity parameter and function, respectively.

$$\dot{\bar{\epsilon}}_m^p = \dot{\epsilon}_0 \left(\frac{\bar{\sigma}_m^*}{S_{sat}} \right)^{\frac{1}{m}} \quad (\text{A.55})$$

where a specific saturating deformation resistance is assumed for the model.

$$\dot{S} = h \dot{\bar{\epsilon}}_m^p \quad (\text{A.56})$$

$$h = h_0 \left[1 - \frac{S}{S_{sat}} \right]^q \text{sign} \left(1 - \frac{S}{S_{sat}} \right) \quad (\text{A.57})$$

where h_0 , q and S_{sat} are material constants.

Step 5. Solving following set of equations implicitly $\bar{\sigma}_v^*$, $\bar{\sigma}'$, S are calculated.

$$\begin{cases} \bar{\sigma}' = \bar{\sigma}'^* - 3G\Delta t \frac{\partial \varphi}{\partial \bar{\sigma}'} \\ \bar{\sigma}_v = \bar{\sigma}_v^* - K\Delta t \frac{\partial \varphi}{\partial \bar{\sigma}_v} \\ S_{n+1} = S_n + \Delta t g(\bar{\sigma}_m^*, S_{n+1}) \end{cases} \quad (\text{A.58})$$

where φ , G and K are the viscoplastic potential, shear modulus and bulk modulus, respectively.

Step 6. stresses are updated.

$$\mathbf{M}_{n+1}^e = \mathbf{N}_{n+1}^{p*} \bar{\sigma}' + \frac{1}{3} \bar{\sigma}_v \mathbf{1} \quad (\text{A.59})$$

Step 7. Plastic deformation gradient is updated.

$$\mathbf{E}_{n+1}^e = \frac{1}{2G} \mathbf{M}_0^e + \frac{1}{3K} \bar{\sigma}' \mathbf{1} \quad (\text{A.60})$$

$$\mathbf{F}_{n+1}^p = \left(\sum_{i=1}^3 \frac{\lambda_i^*}{\lambda_i} \mathbf{e}_i \otimes \mathbf{e}_i \right) \mathbf{F}_n^p \quad (\text{A.61})$$

where λ_i^* , λ_i and \mathbf{e}_i are the eigenvalues and eigenvectors for trail and updated stretch tensor \mathbf{U} .

A.4 Calculation of $\frac{\partial \mathbf{T}}{\partial \mathbf{F}}$

The details of the calculation of the $\frac{\partial \mathbf{T}}{\partial \mathbf{F}}$ for implicit finite element implementation is given in [98]. The summary of the time integration is presented in the equations below.

$$\frac{\partial \mathbf{T}}{\partial \mathbf{F}} = \mathbb{C} - \frac{3}{2} \rho_{n+1}^{-1} \tilde{\mathbf{M}} \otimes \tilde{\mathbf{M}} \quad (\text{A.62})$$

where ρ_{n+1} is calculated as

$$\rho_{n+1} = \frac{3\bar{\mu}}{\eta_{n+1} - \zeta_{n+1}} \quad (\text{A.63})$$

$$\zeta_{n+1} = \left(a_1 + a_2 \frac{b_1}{b_2}\right)^{-1} \quad (\text{A.64})$$

$$\eta_{n+1} = \frac{\bar{\sigma}_{n+1}}{\bar{\sigma}_{n+1}^*} \quad (\text{A.65})$$

$$a_1 = 1 + 3\mu\Delta t \left(\frac{\partial f}{\partial \bar{\sigma}}\right)_{n+1} \quad (\text{A.66})$$

$$a_2 = 3\mu\Delta t \left(\frac{\partial f}{\partial S}\right)_{n+1} \quad (\text{A.67})$$

$$b_1 = \Delta t \left(\frac{\partial g}{\partial \bar{\sigma}}\right)_{n+1} \quad (\text{A.68})$$

$$b_2 = 1 - \Delta t \left(\frac{\partial g}{\partial S}\right)_{n+1} \quad (\text{A.69})$$

and \mathbb{C} is the elastic tangent modulus. f is defined as $f = g^{-1}$, where g is defined in equation (5.16). $\tilde{\mathbf{M}}$ is given as below,

$$\tilde{\mathbf{M}} = 2GN^p \quad (\text{A.70})$$

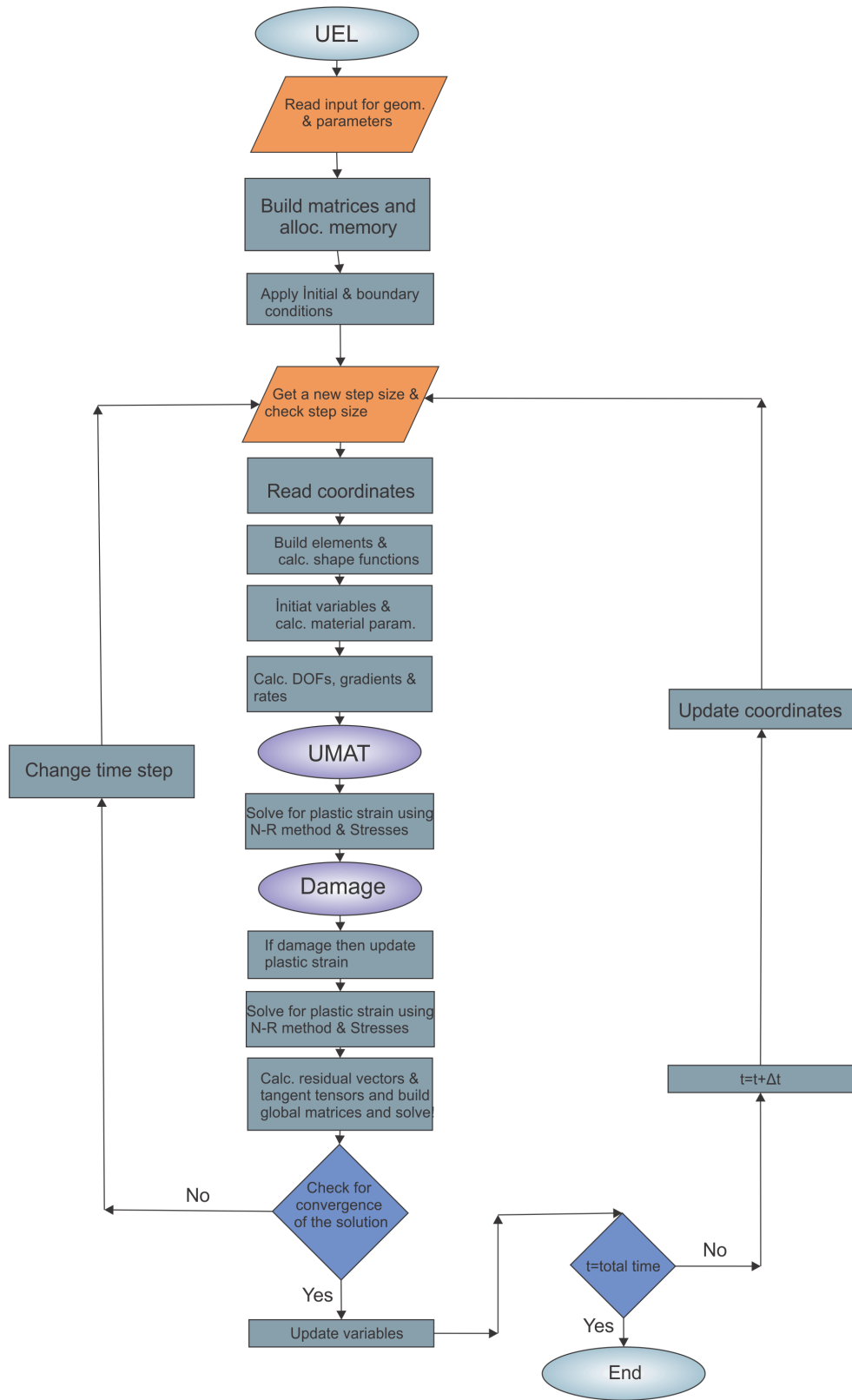


Figure A.1: Flowchart of the user element subroutine.

APPENDIX B

NUMERICAL IMPLEMENTATION OF CAHN-HILLIARD MODEL FOR PHASE SEPARATION

In the following section, the implementation of the Cahn-Hilliard model is presented for the smooth phase transition in the interphase region of a two-phase domain. This implementation is considered as the initial stage of the Allen-Cahn model.

According to Cahn and Hilliard [12], if the non-uniform field is chosen to be the molar fraction of a definite phase, then the free energy density function can be expressed as,

$$\psi(c, \nabla c) = \psi_0(c) + \frac{1}{2}\lambda|\nabla c|^2 \quad (\text{B.1})$$

where $\psi_0(c)$ is the free energy density of the homogeneous solution composition c and the second part of the equation is the interface energy of the composition. $\lambda > 0$ is a coefficient with energy per unit volume times length square unit. The classical derivation of the chemical potential in the form of variational derivative gives,

$$\mu = \frac{\partial\psi(c)}{\partial c} - \lambda\Delta c \quad (\text{B.2})$$

which will yield the classical Fick's law when $\lambda = 0$. Note that Δ is the Laplace operator. Then, the species flux \mathbf{j} can be written as,

$$\mathbf{j} = -\mathcal{M}(c)\nabla\mu \quad (\text{B.3})$$

where $\mathcal{M}(c)$ is the mobility of the species which is a parameter generally defined

dependent on the concentration. The equation for species balance is given as,

$$\dot{c} = \text{Div}(\mathcal{M}(c)\nabla(\frac{\partial\psi(c)}{\partial c} - \lambda\nabla^2c)) \quad (\text{B.4})$$

$\psi_0(c)$ for the solution composition is a non-convex double-well function as depicted in Figure 3.1.

As can be observed in equation (B.4) instead of classical second-order species flux equilibrium a fourth-order equation has to be solved. For finite element solution of the problem, a C^1 -continuous basis function should be used [72]. In order to get rid of this kind of basis functions a solution proposed by Ubachs et al. [121] is generally used. Using the same scheme as Peerlings et al. [122] the relation between the local and non-local terms of the equation (B.4) can be written as a Helmholtz type partial equation [122],

$$\mathcal{C} - l^2\nabla^2\mathcal{C} = c \quad l > 0 \quad (\text{B.5})$$

which can be also written in the following form,

$$\lambda\nabla^2\mathcal{C} + \beta(c - \mathcal{C}) = 0 \quad \text{with} \quad l = \sqrt{\frac{\lambda}{\beta}} \quad (\text{B.6})$$

where \mathcal{C} is a new variable named "micromorphic concentration" and l is an internal length parameter. Then equation (B.2) can be written as,

$$\mu = \frac{\partial\psi(c)}{\partial c} - \beta(c - \mathcal{C}) \quad (\text{B.7})$$

and equation (B.4) for the species concentration reads,

$$\dot{c} = \text{Div}(\mathcal{M}(c)\nabla(\frac{\partial\psi(c)}{\partial c} + \beta(c - \mathcal{C}))) \quad (\text{B.8})$$

B.1 Constitutive equations

An additive total free energy is considered in the following form,

$$\psi(\nu, c, \mathcal{C}, |\nabla\mathcal{C}|) = \psi^{diff}(\nu, c) + \psi^{interface}(\nabla\mathcal{C}) + \psi^{penalty}(c, \mathcal{C}) \quad (\text{B.9})$$

For the diffusion part of the total free energy density the following expression is given [87],

$$\psi^{diff}(\nu, c) = \mu_0 c + c_{max} [R\nu(c \ln c + (1-c) \ln(1-c)) - \chi c(1-c)] \quad (\text{B.10})$$

where c_{max} is the maximum concentration of the diffusing species in the site. The penalty part of the free energy is defined as,

$$\psi^{penalty}(c, \mathcal{C}) = \frac{1}{2} c_{max} \beta (c - \mathcal{C})^2 \quad (\text{B.11})$$

The free energy for gradient of the micromorphic concentration is [87],

$$\psi^{interface}(\nabla\mathcal{C}) = \frac{1}{2} c_{max} \lambda |\nabla\mathcal{C}|^2 \quad (\text{B.12})$$

Then the total free energy density for diffusion can be written as,

$$\psi(c) = c_{max} \left[\mu_0 c + R\nu (c \ln c + (1-c) \ln(1-c)) - \chi c(1-c) + \frac{1}{2} \beta (c - \mathcal{C})^2 + \frac{1}{2} \lambda |\nabla\mathcal{C}|^2 \right] \quad (\text{B.13})$$

where μ_0 is the reference chemical potential.

Micro-stresses:

From outcomes of energy balance of the system, following equations can be written

[87],

$$\left\{ \begin{array}{l} \mu = \frac{\partial\psi(\Phi)}{\partial c} \\ \mathcal{P} = \frac{\partial\psi(\Phi)}{\partial \mathcal{C}} \\ \mathcal{E} = \frac{\partial\psi(\Phi)}{\partial \nabla \mathcal{C}} \end{array} \right. \quad (\text{B.14})$$

Using equations (B.11), (B.12) and (B.14) following micro-stresses are calculated.

$$\begin{aligned} \mathcal{P} &= -\beta(c - \mathcal{C}) \\ \mathcal{E} &= \lambda \nabla \mathcal{C} \end{aligned} \quad (\text{B.15})$$

Chemical potential:

Using equations (B.10) and (B.14) for the chemical potential one can write,

$$\mu = \mu_0 + R\nu[\ln c - \ln(1 - c)] - \chi(1 - 2c) + \beta(c - \mathcal{C}) \quad (\text{B.16})$$

B.2 Numerical Implementation

For the implementation purpose, now an additional degree of freedom should be considered in the FEM process as explained before. The approximations of the fields can be written as below.

$$c = \sum_{i=1}^n N_i c_i, \quad \nabla c = \sum_{i=1}^n \mathbf{B}_i c_i \quad (\text{B.17})$$

$$\mathcal{C} = \sum_{i=1}^n N_i \mathcal{C}_i, \quad \nabla \mathcal{C} = \sum_{i=1}^n \mathbf{B}_i \mathcal{C}_i \quad (\text{B.18})$$

where n is the number of nodes and $\mathbf{B}_i = \nabla N_i$. For simplicity a relation between the diffusion coefficient (D) and mobility of the material is assumed in the following form [123] on the basis of constant diffusion coefficient.

$$\mathcal{M} = \frac{D}{R\nu}c(1-c) \quad (\text{B.19})$$

$$D = D_0 \quad (\text{B.20})$$

where D_0 represents the initial value for the diffusion coefficient. Substituting (B.19) in (B.4) and doing some algebra the balance equation can be written as,

$$\dot{c} - \text{Div} \left[\frac{\mathcal{M}}{c_{max}} \left(\left(\frac{R\nu}{c(1-c)} - 2\chi + \beta \right) \nabla c + \beta \nabla \mathcal{C} \right) \right] = 0 \quad (\text{B.21})$$

Multiplying equation (B.21) with the weighting function w and integrating over the element volume Ω_e one can get

$$\int_{\Omega_e} w \left[c_{max} \dot{c} - \text{Div} \left(\mathcal{M} \left(\left(\frac{R\nu}{c(1-c)} - 2\chi + \beta \right) \nabla c + \beta \nabla \mathcal{C} \right) \right) \right] dV = 0 \quad (\text{B.22})$$

Then the weak form of the equation (B.22) is found for the boundary value problem. The boundary conditions read as follows.

$$\begin{cases} c = c_0 \text{ on } \partial\Omega_c \\ -D \frac{\partial c}{\partial \mathbf{x}_i} = j_0 \text{ on } \partial\Omega_j \end{cases} \quad (\text{B.23})$$

Defining,

$$a = \mathcal{M} \left(\frac{R\nu}{c(1-c)} - 2\chi + \beta \right) \quad (\text{B.24})$$

$$b = \mathcal{M}\beta \quad (\text{B.25})$$

Using integration by parts and the divergence theorem the residual vector is calculated.

$$R_c = \int_{\Omega_e} [c_{max} w \dot{c} + a \nabla w \cdot \nabla c - b \nabla w \cdot \nabla \mathcal{C}] dV - \int_{\partial\Omega_j} \mathbf{j} \cdot \mathbf{n} dS = 0 \quad (\text{B.26})$$

Let N_A be the shape function for the interpolation of node A, then the residuals can be calculating substituting the approximation $w = N_A w_A$,

$$R_c^A = \int_{\Omega_e} [c_{max} N_A \dot{c} + a \nabla N_A \cdot \nabla c - b \nabla N_A \cdot \nabla \mathcal{C}] dV - \int_{\partial\Omega_j} \mathbf{j} \cdot \mathbf{n} dS = 0 \quad (\text{B.27})$$

Considering the balance equation (B.5) the residual for micromorphic concentration can be calculated in the same manner,

$$R_c^A = \int_{\Omega_e} N_A \beta (c - \mathcal{C}) - \lambda \nabla N_A \cdot \nabla \mathcal{C} dV + \int_{\partial\Omega_\varepsilon} N_A \boldsymbol{\varepsilon} \cdot \mathbf{n} dS = 0 \quad (\text{B.28})$$

The elements of stiffness matrix are also calculated to be,

$$K_{cc}^{AB} = - \int_{\Omega_e} [c_{max} \frac{N_A N_B}{\Delta t} + a \nabla N_A \nabla N_B + \frac{\partial a}{\partial c} N_B \nabla N_A \nabla c - \frac{\partial b}{\partial c} N_B \nabla N_A \nabla \mathcal{C}] dV - \int_{\partial\Omega_j} N_A N_B \frac{\partial \mathbf{j}}{\partial c} \cdot \mathbf{n} dS \quad (\text{B.29})$$

where,

$$\frac{\partial a}{\partial c} = \frac{\partial \mathcal{M}}{\partial c} \left(\frac{R\nu}{c(1-c)} - 2\chi + \beta \right) + \frac{\mathcal{M}}{c_{max}} \frac{R\nu(2c-1)}{c^2(1-c)^2} \quad (\text{B.30})$$

$$\frac{\partial b}{\partial c} = \beta \frac{\partial \mathcal{M}}{\partial c} \quad (\text{B.31})$$

$$K_{CC}^A = - \int_{\Omega_e} -\beta N_A N_B - \lambda \nabla N_A \nabla N_B dV + \int_{\partial\Omega_\varepsilon} N_A N_B \frac{\partial \boldsymbol{\varepsilon}}{\partial \mathcal{C}} \cdot \mathbf{n} dS = 0 \quad (\text{B.32})$$

The non-zero off-diagonal elements of the stiffness matrix are as following,

$$K_{cC}^{AB} = \int_{\Omega_e} b \nabla N_A \nabla N_B dV \quad (\text{B.33})$$

$$K_{Cc}^{AB} = - \int_{\Omega_e} \beta \nabla N_A \nabla N_B dV \quad (\text{B.34})$$

An analysis was carried out for the geometry and boundary conditions depicted in Figure B.1. The initial conditions for the normalized concentration were defined to be $c = 0.8$ in the upper half of the model and $c = 0.2$ in the lower half. Two different models were used to test the diffusion of the species from the upper half to the lower half via changing the parameter β in equation (B.8). It is very obvious that defining $\beta = 0$ will change this equation to classical Fick's law and defining a non-zero value for β leads to the higher-order diffusion model. The material properties used in the simulation are given in Table B.1. Figure B.2 shows the species concentration after 12hrs in the domain. It can be observed that diffusing species has no definite boundary in the case with $\beta = 0$ and when $\beta = 1 \times 10^8$ an interphase region with a hyperbolic distribution of the concentration is formed.

Table B.1: Material and analysis parameters

Material parameters	@ 1473 K	unit
D	1.6×10^{-17}	m^2/s
β	1×10^8	-
λ	1×10^{-10}	m^2
χ	1×10^7	-
R	8.314	$\text{J}/\text{mol} \cdot \text{K}$

Figure B.3 and Figure B.4 show the evolution of the concentration on a path that lies along the diffusion direction for two different models. It can be seen that the C-H solution reaches a steady state where stationary interface forms. The steady-state limits of concentration may appear to be above or below initial condition values due to the high or low interfacial energy, which can be calibrated by solution parameters.

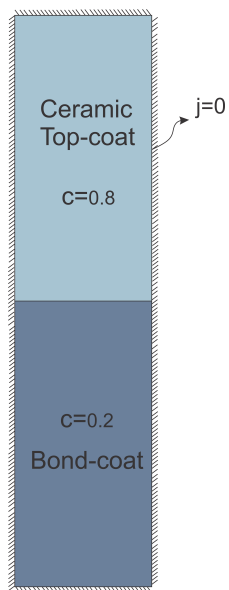


Figure B.1: No-flux condition at boundaries and initial concentrations in upper and lower regions.

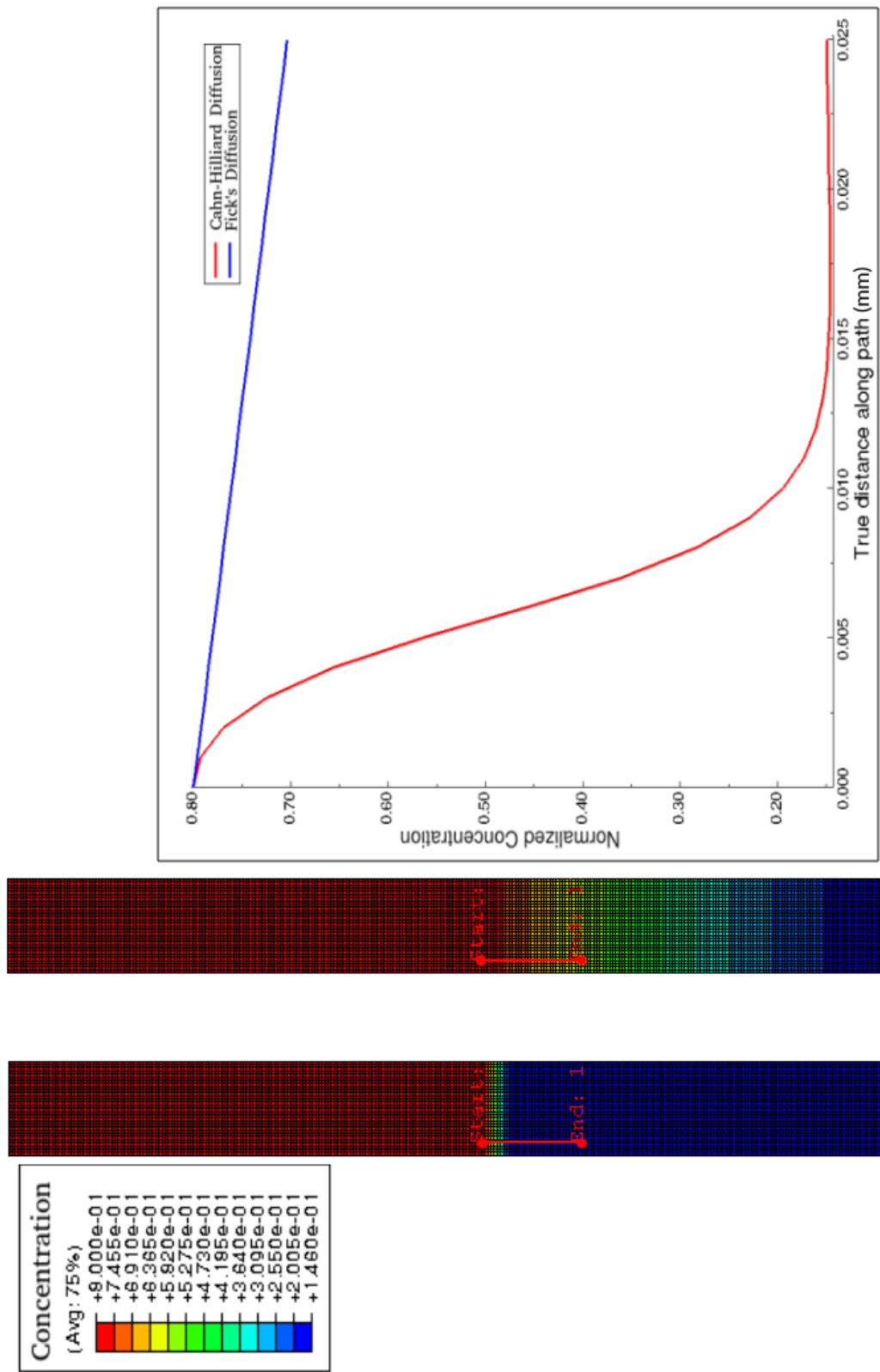


Figure B.2: Phase field illustration after approximately 12 hrs. The left contour corresponds to the C-H solution while the right one corresponds to Fick's law.

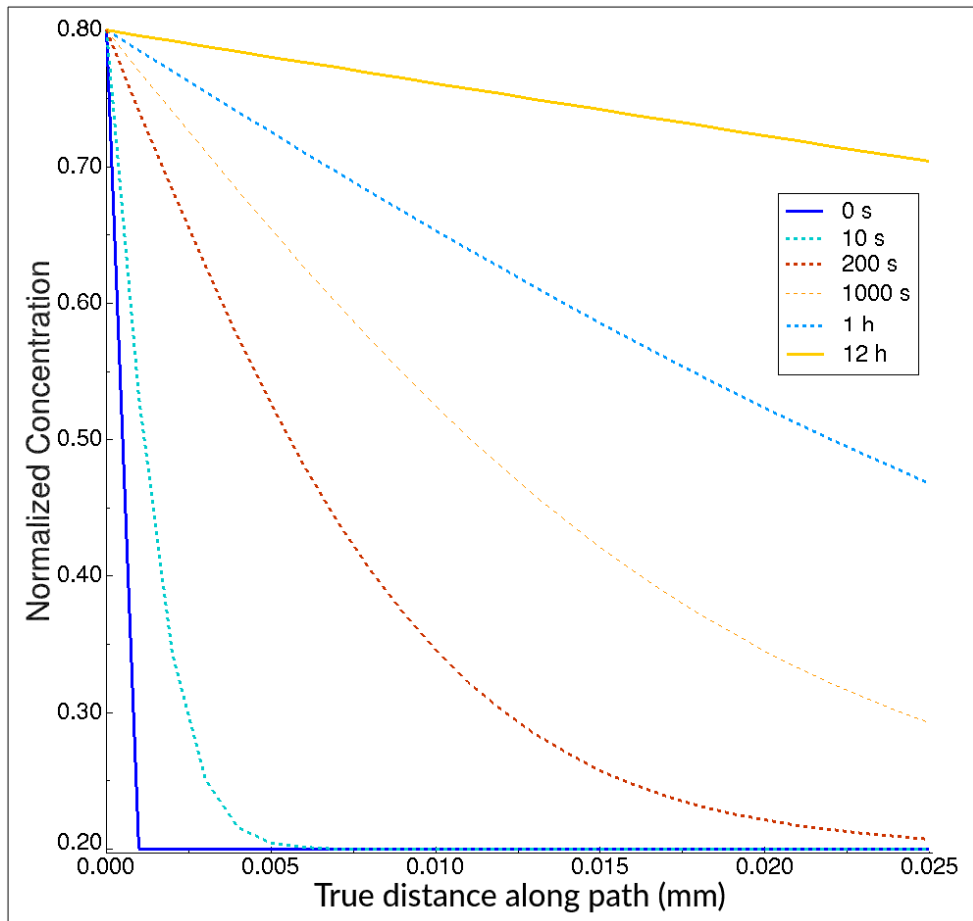


Figure B.3: Time evolution of normalized concentration on the path presented in the previous figure for diffusion with the Fick's law

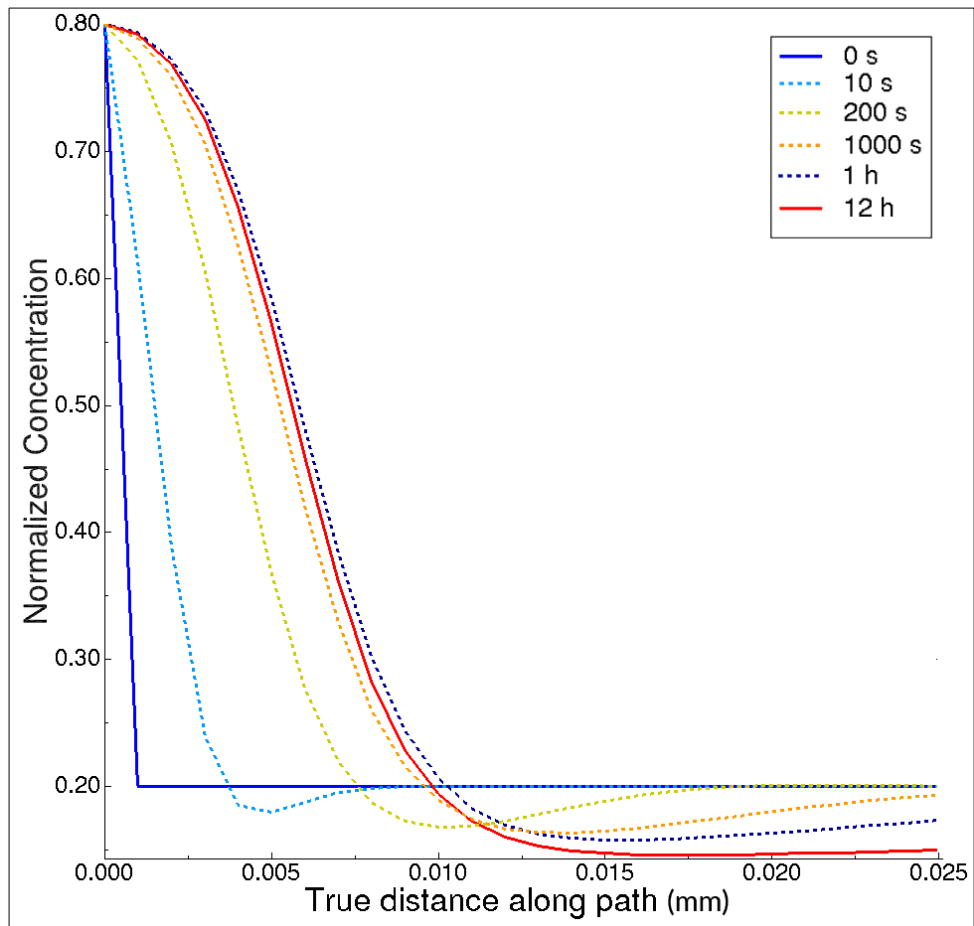


Figure B.4: Time evolution of normalized concentration on the path presented in the previous figure (b) for diffusion with the C-H law

APPENDIX C

MATERIAL AND ANALYSIS PARAMETER CALIBRATION

C.1 Top-coat elasticity

Due to brittleness of the YSZ material, when deposited via the EB-PVD technique this material may owe its plastic behavior to defect and crack already present in the structure. Thus, early damage and fracture are inevitable in the ceramic structure and a damage model has to associate the viscoplastic model used for the material.

Determining elastic modulus of a severely anisotropic structure like EB-PVD YSZ is not an easy task, but using a technique called amplitude-dependent damping (ADD) an estimation of this material property was found in [16]. Furthermore, the Poisson's ratio was reported as $\nu = 0.29$. It has been also reported, that the substrate plays a critical role in the results for the elastic modulus of deposited ceramic (Figure C.1).

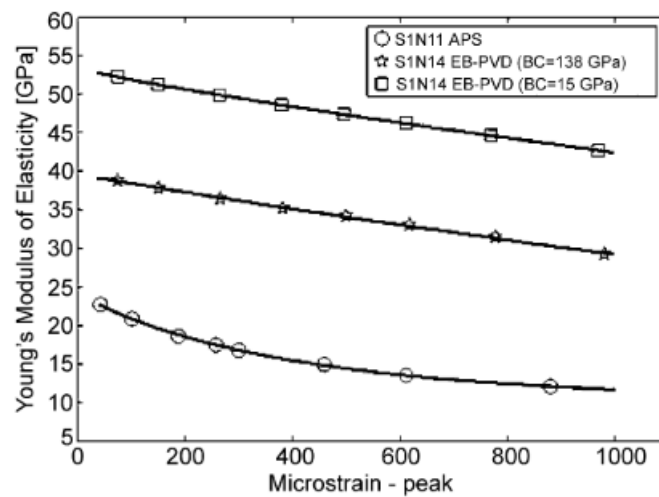


Figure C.1: Young's modulus for TBC deposited on different bondcoats [16].

An average value of 40GPa was chosen for the elastic modulus of the top-coat. Furthermore, the top-coat is assumed to be isotropic, but The transversely isotropic behavior would be more appropriate for this layer. A specific anisotropic model may be also used taking change of column orientation into account [17] (Figure C.2). However, for simplicity an isotropic structure is assumed for the top-coat in this study.

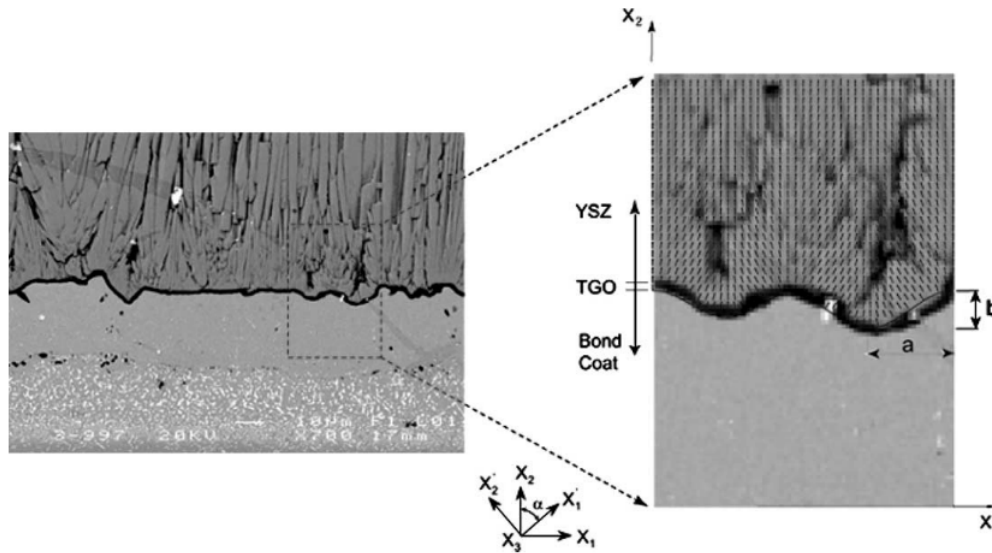


Figure C.2: Change of column orientation in the EB-PVD deposited ceramic layer [17].

C.2 Bond-coat elasto-viscoplasticity

As discussed in previous chapters an elasto-viscoplastic material model was used for $FeCrAlY$ bond-coat. The model parameters were calibrated using experimental data available in the literature for the material at 700K [4], since thermal analysis for the TBC at 1000°C reveal that the TGO and the BC layers are approximately around 400°C in the APS coating system. It should be noted that in this thesis 1200°C is accepted as the service temperature, the temperature in the TGO and the bond-coat layers are roughly estimated to be around 400°C [99]. The material properties at 400°C are given in Table C.1. The calibrated material parameters can be found in Table 4.2. The result of a uniaxial tension test and the comparison with test data is presented in the Figure C.3. The medium was pulled with constant strain rate

$\dot{\epsilon} = 2.16 \times 10^{-6}$ m/s in accordance with the experiment. The ultimate tensile strength was reported to be $\sigma_u = 520$ MPa, but since the failure was expected to happen in the TGO, ceramic, and most probably in the material interfaces no failure stress limit was defined for the bond-coat.

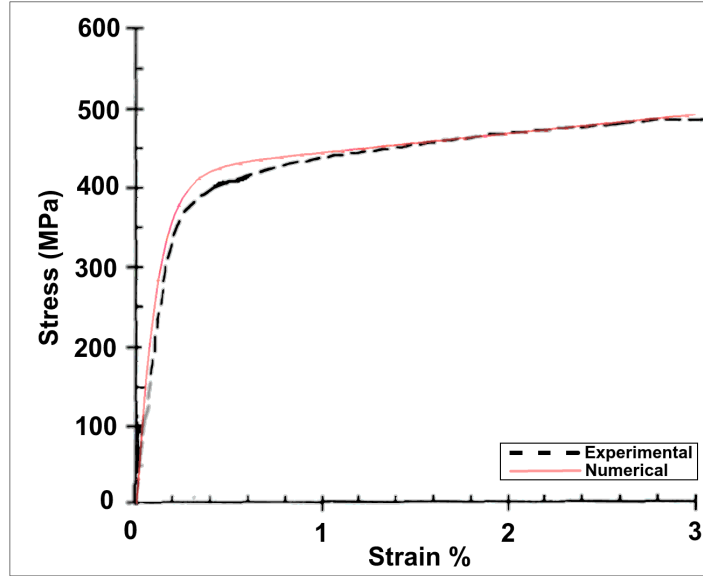


Figure C.3: Stress-strain curve for *FeCrAlY* experimental (black) and numerical (red) result comparison [4].

Table C.1: Material parameters for *FeCrAlY* at 400°C [3, 4]

Material parameters	Value	Unit
G	92.31	GPa
E	240	GPa
K	200	GPa
ν_p	0.3	-

C.3 Alumina layer

The same material model as bond-coat is used for the thermally grown oxide layer. Material properties for for 99.6% grade alumina with less than 2% porosity in room temperature is given in Table C.2 [124, 125, 126].

Following functional rule is accepted for the change of properties (the Young's modulus E , the shear modulus G and the Poisson's ratio ν_p) with respect to the temperature [127].

$$E = E_0(1 - \eta_E(\nu - 25)) \quad (\text{C.1})$$

$$G = G_0(1 - \eta_G(\nu - 25)) \quad (\text{C.2})$$

$$\nu_p = \nu_{p0}(1 - \eta_{\nu_p}(\nu - 25)) \quad (\text{C.3})$$

where ν represents the temperature. The parameters with subscript 0 correspond to room temperature values. η_E , η_G and η_{ν_p} are the constant coefficients for interpolation. The values for the material properties and coefficients at room temperature is given in Table C.2.

Table C.2: Material parameters for alumina at room temperature

Material parameters	Value	Unit
G_0	163	GPa
E_0	403	GPa
K_0	254.	GPa
ν_{p0}	0.23	-
η_E	1.2×10^{-4}	$1/^\circ\text{C}$
η_G	1.4×10^{-4}	$1/^\circ\text{C}$
η_{ν_p}	6.2×10^{-5}	$1/^\circ\text{C}$

Using functions in equation (C.1), (C.2) and (C.3) material parameters at 400°C can be found as shown in Table C.3.

The compressive strength of the alumina is reported to be around $2 - 4\text{GPa}$ [128]. This property for this material at 400°C (Interface temperature) can be assumed to be around 1GPa [129].

Table C.3: Material parameters for alumina at 400°C

Material parameters	Value	Unit
G	154.44	GPa
E	384	GPa
K	231	GPa
ν_p	0.224	-

APPENDIX D

FINITE ELEMENT IMPLEMENTATION

Implementation of the model is carried out by using User Element (UEL) in ABAQUS software, where ABAQUS is basically used as a solver and a visualiser. Two dimensional quadrilateral elements with four linear nodes are developed for the plane-strain analysis. Since ABAQUS does not support graphical output of the user elements, for the visualization of the results, a mock mesh is created using dummy CPE4T plane strain elements already defined in ABAQUS. These elements are attached to the user elements to share the outputs. A total of five degrees of freedom (u_1, u_2, e, c, ϕ) are defined for the elements. Considering the two dimensional four node isoparametric element used for the analysis of the plane strain problem, the interpolation of the of the DOFs and their gradients in an element can be expressed as,

$$\mathbf{u} = \sum_{i=1}^n N_i \mathbf{u}_i, \nabla \mathbf{u} = \sum_{i=1}^n \mathbf{B}_i \mathbf{u}_i \quad (\text{D.1})$$

$$e = \sum_{i=1}^n N_i e_i, \nabla e = \sum_{i=1}^n \mathbf{B}_i e_i \quad (\text{D.2})$$

$$c = \sum_{i=1}^n N_i c_i, \nabla c = \sum_{i=1}^n \mathbf{B}_i c_i \quad (\text{D.3})$$

$$\phi = \sum_{i=1}^n N_i \phi_i, \nabla \phi = \sum_{i=1}^n \mathbf{B}_i \phi_i \quad (\text{D.4})$$

where N^i are the shape functions used for the interpolation. For the specific four node

linear isoparametric element shape functions are given by,

$$\begin{cases} N_1 = \frac{1}{4}(1 - \xi)(1 - \eta) \\ N_2 = \frac{1}{4}(1 + \xi)(1 - \eta) \\ N_3 = \frac{1}{4}(1 + \xi)(1 + \eta) \\ N_4 = \frac{1}{4}(1 - \xi)(1 + \eta) \end{cases} \quad (\text{D.5})$$

The velocity and rates of change of the DOFs can be calculated using the values at time t (beginning of the step) and time $(t + 1)$ end of the time step (dt) as follows:

$$\mathbf{V}_{t+1} = \frac{\mathbf{u}_{t+1} - \mathbf{u}_t}{dt} \quad (\text{D.6})$$

$$\dot{c}_{t+1} = \frac{c_{t+1} - c_t}{dt} \quad (\text{D.7})$$

$$\dot{\phi}_{t+1} = \frac{\phi_{t+1} - \phi_t}{dt} \quad (\text{D.8})$$

$$\dot{e}_{t+1} = \frac{e_{t+1} - e_t}{dt} \quad (\text{D.9})$$

The isoparametric mapping of a typical element is schematically shown in Figure D.1.

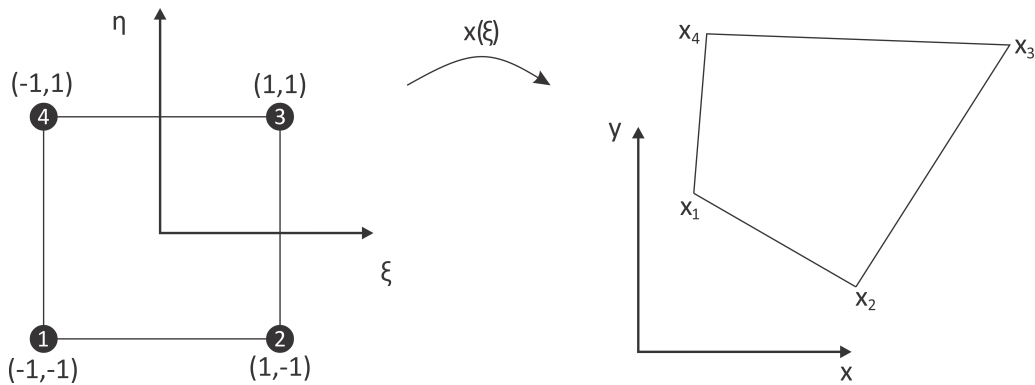


Figure D.1: Isoparametric mapping.

The following relation is given for mapping the derivatives of the shape functions using Jacobian J .

$$\begin{bmatrix} \frac{dN}{dx} \\ \frac{dN}{dy} \end{bmatrix} = J^{-1} \begin{bmatrix} \frac{dN}{d\xi} \\ \frac{dN}{d\eta} \end{bmatrix} \quad (\text{D.10})$$

For plane strain analysis \mathbf{B} matrix for an element has the following standard form.

$$\mathbf{B} = \begin{bmatrix} N_{1,1} & 0 & N_{2,1} & 0 & \dots & N_{nNode,1} & 0 \\ 0 & N_{1,2} & 0 & N_{2,2} & \dots & 0 & N_{nNode,2} \\ N_{1,2} & N_{1,1} & N_{2,2} & N_{2,1} & \dots & N_{nNode,2} & N_{nNode,1} \end{bmatrix} \quad (\text{D.11})$$

where $N_{i,1}$ and $N_{i,2}$ represent $\frac{\partial N_i}{\partial x}$ and $\frac{\partial N_i}{\partial y}$, respectively. \mathbf{G} matrix is also defined as below[130].

$$\mathbf{G} = \begin{bmatrix} N_{1,1} & 0 & N_{2,1} & 0 & \dots & N_{nNode,1} & 0 \\ 0 & N_{1,2} & 0 & N_{2,2} & \dots & 0 & N_{nNode,2} \\ N_{1,2} & 0 & N_{2,2} & 0 & \dots & N_{nNode,2} & 0 \\ 0 & N_{1,1} & 0 & N_{2,1} & \dots & 0 & N_{nNode,1} \end{bmatrix} \quad (\text{D.12})$$

The deformation gradients at the beginning and end of the time step are calculated as below:

$$\mathbf{F}_t = 1 + \nabla \mathbf{u}_t \quad \mathbf{F}_{t+1} = 1 + \nabla \mathbf{u}_{t+1} \quad (\text{D.13})$$

where \mathbf{u}_t and \mathbf{u}_{t+1} are displacements at time t and $t + 1$.

D.1 F-bar method

The volumetric locking is an important issue in 4 node elements [130], however using F-bar method the deformation gradient can be modified to avoid the locking. The locking happens in the incompressible limit when low-order elements are used. Thus, if an isochoric (\mathbf{F}_d) and a volumetric (\mathbf{F}_v) split for the deformation gradient is considered in the following form

$$\mathbf{F} = \mathbf{F}_d \mathbf{F}_v \quad (\text{D.14})$$

the volumetric part of the deformation gradient \mathbf{F}_v can be replaced by the volumetric deformation gradient at the centroid of the element $(\mathbf{F}_o)_v$. Then the modified deformation gradient $\bar{\mathbf{F}}$ is given as

$$\bar{\mathbf{F}} = \mathbf{F}_d (\mathbf{F}_o)_v = \left[\frac{\det(\mathbf{F}_o)}{\det(\mathbf{F})} \right]^{\frac{1}{3}} \mathbf{F} \quad (\text{D.15})$$

As pointed out before, for high-order elements (e.g. 8 node element) this modification is not needed since numerical locking would not occur during the analysis.

CURRICULUM VITAE

PERSONAL INFORMATION

Surname, Name : Sait, Ferit

Nationality : Turkish (TC)

Date and Place of Birth : 3 May 1986, Miyandoab, Iran

Phone : +90 541 673 1176

E-mail : farid.saeidi@metu.edu.tr

EDUCATION

Degree	Institution	Year of Graduation
MS	METU	2013
BS	Azad University	2008

WORK EXPERIENCE

Year	Place	Enrollment
2016-Present	Atilim University	Lecturer

PUBLICATIONS

1. F. Sait, E. Gurses and O. Aslan, "Modeling and simulation of coupled phase transformation and stress evolution in thermal barrier coatings," *International Journal of Plasticity*, 2020 (accepted for publication)
2. F. Saeidi, E. Gurses and O. Aslan, "A Numerical Approach to Simulate Oxidation in Thermal Barrier Coatings," *in Reference module in material Science and Material Engineering*, pp. 986-992, Elsevier Ltd., 2020.
3. F. Saeidi, S. Dag, "Thermal Fracture Analysis of Fibrous composites with Variable Fiber Spacing Using Jk-Integral," *IJMME*, 11, 3, 2017.

4. F. Saeidi, R. Orhan Yildirim, "Interaction of Armour Penetrating Bullet with Non-Explosive Reactive Armour Cassette," SAVTEK, METU, 2016
5. F. Saeidi, M. C. Kurt, T. Deniz, E. Gürses, 3D Numerical Simulation of Nonenergetic Reactive Armor," 8th Ankara International Aerospace Conference (AIAC), 2015.
6. Kurt M. C. , Saeidi F., Gürses E., Çukur İmla Şişen Zirh Etkileşiminin Sayisal Yöntemlerle İncelenmesi, (Simulation of Shaped charge Jet and Non-explosive Reactive Armor Interaction)," SAVTEK, METU, 2014
7. Rohani B., Latifi-Navid M., Saeidi F., Ghaziani M, "A Hydraulic Strategy Design for Modeling and Simulation of A Mold Oscillation System," The 15th International Conference on Machine Design and Production, June 19– 22, Pamukkale, Denizli, Turkey, 2012